Frontiers Of Dealloying – Novel Processing For Advanced Materials

by

Ian McCue

A dissertation submitted to Johns Hopkins University in conformity with the requirements for the degree of Doctor of Philosophy

Baltimore, Maryland

October, 2015

Abstract

Dealloying is the selective dissolution in a liquid environment of one or more component sfrom a multicomponent metal alloy, leaving behind a material enriched in the remaining component(s). This process can be broken down into two competing kinetic reactions: surface roughening from dissolution, and surface smoothening from diffusion of the remaining component(s) along the metal/liquid interface. When both rates are approximately equal porosity evolution can occur, leading to the formation of a porous metal with a characteristic ligament and pore size. Previous work in this field has heavily focused on using the dissolution rate to control porosity evolution, but in this dissertation we study how surface diffusivity affects dealloying and use it as a dial to control the resulting structure.

Starting with finite systems we use kinetic Monte Carlo simulations to study how particle size affects porosity evolution. Dealloying is used extensively to fabricate next-generation catalysts, however this process isn't well-understood at small particle sizes. We report that changes to the chemical potential due to high curvatures increases the surface diffusivity, making it more difficult to evolve porosity in nanoparticle systems. It follows that higher dealloying potentials are required to overcome this increased surface diffusion rate.

We then turn to the fabrication of porous refractories where the surface diffusivity is very low. Electrochemical dealloying of refractory alloys does not lead to porosity evolution because the homologous temperature (reaction temperature normalized by the melting point of the remaining component) is too low. To solve this we extended the concept of dealloying to a liquid melt where we can reach much higher temperatures in order to fabricate porous structures. We studied the morphology, dealloying rate and ligament size as functions of composition, temperature, and time, and developed a model for liquid metal dealloying.

Lastly, in addition to studying the kinetics of porosity evolution we used this new technique to fabricate refractory-based composites and report the first bicontinuous metal/metal composite materials. We were able to fabricate bulk quantities (~ 1 cm^3) and studied their base mechanical properties, e.g. the yield strength. The materials show size-dependent strengthening and provide a new processing route to fabricate bulk nanostructured materials.

Advisor: Dr. Jonah Erlebacher

Readers: Dr. Jonah Erlebacher, and Dr. Kevin Hemker

Acknowledgements

First and foremost I would like to thank my advisor Dr. Jonah Erlebacher for his guidance and mentorship throughout my graduate and undergraduate research at Johns Hopkins University. He has helped me grow immensely as a researcher, speaker, and writer. He constantly challenged me to think outside of the box and always encouraged me to pursue any odd idea that I may have for a research project. I hope in the future to be able to create a similar creative environment for my own students.

I would like to thank the members of my committee: Dr. Kevin Hemker, Dr. Robert Cammarata, Dr. Tim Weihs, Dr. Jaafar El-Awady, Dr. Evan Ma, and Dr. Tyrel McQueen. I would like to thank everyone who has collaborated with me over the years on exciting projects: Dr. Karl Sieradzki, Dr. Alain Karma, Dr. Mingwei Chen, Dr. Pierre-Antoine Geslin, and Dr. Matteo Seita. I would also like to thank Dr. Orla Wilson for all of her help and advice during my undergraduate and graduate career at Johns Hopkins; you are a great mentor and have great taste in music!

I would like to thank my former and current labmates: Josh Snyder, Felicitee Kertis, Ellen Benn, and Bernard Gaskey. I've enjoyed many research and non-research related discussions, and I'm glad that I can send you a text about research at 1 am, and you think it's totally normal. I would also like to thank my fellow graduate students for their support, coffee enthusiasm, and good times inside and outside of lab (in no particular order): Nick Krywopusk, Amanda Levy, Jesse Placone, Steve Farias, Steve Ryan, Alex Kinsey, Mike Grapes, and many others it would take too long to list.

I would like to give a special thanks to all of my fencing friends I have met during my graduate career: my coaches, Austin Young and Aaron Kandlik; Hopkins fencing alumnus Dr.

Carl Liggio; Hopkins varsity fencers, Ben Wasser, Glenn Balbus, Jay Petrie, and many others; my fencing friends at Rockville fencing academy, Stuart Sacks, Andrew Holbrook, Steve Gross, Don Davis, Levente Szego, Joe Hsu, Roshan Talagala, JD Schwartzman, Andy Radu, and many others. Fencing has kept me sane all of these years and I wouldn't have been able to make it through graduate school without you! It was an honor fencing everyone and thank you for fencing me.

I owe a great deal of thanks to the former and current staff of the Materials Science and Engineering department: Marge Weaver, Mark Koontz, Dorothy Reagle, Jeanine Majewski, Alex Van Horn, Ada Simari, and Bryan Crawford.

I cannot thank my parents enough for their support during my graduate career. My mother who taught me to follow my heart which has yet to lead me to a bad decision or anything I regret. A big thank you to my father who is the reason why I am a scientist. I will never forget him helping me with Science Olympiad in high school and encouraging me to study nanoscience in college (think the scene from The Graduate when Mr. McGuire says "plastics"). He has always been there to give me advice on all-things academia, whether it is looking at a manuscript draft, how I should handle a tough reviewer, or discussing my future career. I am also thankful for the love and support of my sister Sarah and brothers-in-law Shaun and Hyung-nim, my parents-in-law Umma and Appa, and the rest of my extended family (including Zoey, Indy, and Boswell).

Above all, I would like to thank my wife Jessica. You have always been there for me, supporting me throughout this process, and I would not be defending if it weren't for you. I have told you many times already, but marrying you was the greatest decision of my life and

our wedding day was the best day of my life. I love you so much and thank you for everything you have done for me.

Table of Contents

List of tables

List of figures

Dedicated to my wife Jessica,

Chapter 1 Introduction/Background

1.1 Chapter Summaries

Dealloying was originally resitricted to corrosion, but now it is considered a facile self-organization technique to fabricate high surface area, bicontinuous nanoporous materials (Figure 1.1). Owing to their high interfacial area and the versatility of metallic materials,

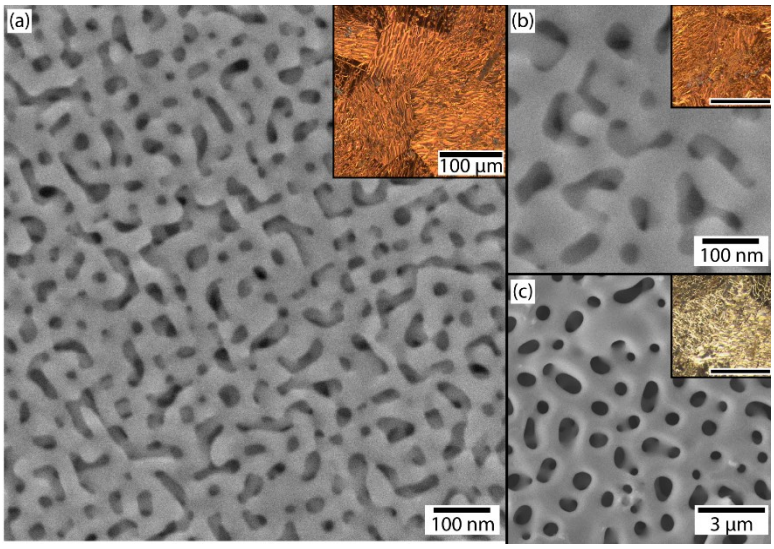

Figure 1.1. SEM and optical (inset) micrographs of nanoporous gold (np-Au) formed by free corrosion dealloying of homogeneous $Ag_{65}Au_{35}$ alloy in concentrated nitric acid. After initial dealloying for 24 hours the system exhibits ~30 nm features (a) which coarsen to ~60 nm after an additional 100 hours in nitric acid (b) or several micrometers after heating to 800°C for 10 minutes (c). Inset scale bars are 100 µm.

nanoporous metals have found application in catalysis, sensing, actuation, electrolytic and ultra-capacitor materials, high temperature templates/scaffolds, battery anodes, and radiation-damage tolerant materials (*1*–*7*). Despite the fact that the kinetics of formation dictate the composition, morphology, and ligament crystal orientation of the resulting nanoporous metal, the majority of the research on nanoporous metals has focused on the characterization and properties of dealloyed materials.

The aim of this thesis is to examine the fundamental kinetic processes involved in the formation of nanoporous metals made by dealloying, and use this knowledge to fabricate new nanomaterials. We will show that porosity evolution via dealloying is not limited to electrochemical techniques and can be generalized into any liquid-mediated dissolution. We will first start with examining the kinetic reactions that result in porosity evolution in the context of electrochemical dealloying, extend the kinetic theory to dealloying in a liquid metal, and finally examine some applications of these materials.

In Chapter 2 we examine dealloying in finite volumes by studying binary alloy nanoparticles using kinetic Monte Carlo methods. Elemental metal nanoparticles were shown to be less stable with decreasing particle size, however we observed that porosity evolution became more difficult with decreasing particle size. This is explained by noting that the surface diffusion rate increases with decreasing particle size, effectively passivating the surface. In order for porosity to evolve the dissolution rate (a function of the applied potential) needs to increase to overcome this surface passivation.

In Chapter 3 we introduce the concept of liquid metal dealloying as an alternative method to produce porous structures. Corrosion can occur in any type of liquid medium, but only recently has this idea extended to porosity evolution. We develop a liquid metal dealloying

system that is used in the following chapters and present the initial proof of concept. We demonstrate that we are able to precisely control the morphology and ligament size of the resulting structures.

In Chapter 4 we examine the fundamental kinetic parameters in liquid metal dealloying in order to gain a better understanding of how to fabricate bulk nanostructures. We study how the dealloying depth, ligament size, and concentration of the liquid phase change as a function of time, temperature and composition. Additionally, we introduce a dealloying model to relate these parameters together and compare it to our experimental results. This work demonstrates that the rate-limiting step is diffusion of the dissolving component out of the dealloyed structure and provides a framework for future work on liquid metal dealloying.

In Chapter 5 we report the baseline mechanical properties of bicontinuous composites produced using liquid metal dealloying. These materials offer a solution on how to assemble bulk microstructures and are an interesting model to study mechanical properties in confined systems. The majority of size-dependent studies have been performed on micropillars and nanowires, but both of these systems have free surfaces and undergo rapid strain bursts. The bicontinuous composites in this chapter are effectively constrained pillars/nanowires and as a result their deformation behavior is similar to bulk materials. This allows the material to undergo significant work hardening and possibly achieve very high dislocation densities prior to failure.

The remainder of this introduction is dedicated to the fundamentals of dealloying as defined in the literature, liquid metal dealloying, and finally the mechanical properties of nanoporous materials.

1.2 Dealloying Mechanism

Dealloying refers to the selective dissolution of one or more components from an alloy, leaving behind a material enriched in the more-noble alloy component (*8*, *9*). Under conditions where the dissolution rate is fast enough relative to the surface diffusion rate of the undissolved component, it is well-established that a nanoscale pattern forming instability arises that drives the formation of nanoporosity during dealloying of bulk alloys, where the intrinsic lengthscale of this pattern forming instability is on the nanometer scale (*10*, *11*). The pore and ligament size can be dialed-in during the dealloying process by controlling the surface diffusion rate (e.g. using a different electrolyte solution) or by controlling the dissolution rate (e.g. changing the applied potential). Alternatively, the dealloyed structure can be coarsened after fabrication in an electrolyte solution or in a gas environment (air, N_2, Ar) at an elevated temperature. The smallest reported ligament and pore size is around 2 nm (*12*), and the largest reported structures are tens of microns (*13*). This tunability and ease of fabrication are the two largest reasons for the popularity of nanoporous metals.

The concept of dealloying has been well-known for over a century, but in the context of corrosion as a materials phenomenon to be avoided. Depletion gilding, enriching the surface of Cu-Au alloys, is a form of dealloying that dates as far back as pre-Columbian Andean cultures (*14*). More recently, dealloying has been studied in the context of dezincification of Zn-Cu and Al-Zn brasses. Despite being studied extensively, the mechanism by which porosity evolves has only recently been solved. Pickering and Wagner (*15*) were the first to introduce a dissolution model in the 1960's, arguing volume diffusion was the mechanism for pit formation, however, this required unphysical bulk diffusion rates. Forty in the 1970s suggested surface diffusion may play a role, but bulk diffusion was still considered the primary

mechanism (*16*). Pickering, Wagner and Forty contributed significantly to the field of corrosion, but they were unable to elucidate the correct mechanism of porosity evolution because surface diffusion rates in electrochemical solutions were assumed to be similar to surface diffusion rates for metals in vacuum (very low). This idea changed in the 1990s when scanning tunneling microscopy was used to directly measure surface diffusivities in electrolyte solutions. As a comparison, the surface diffusivity of a metal in vacuum is approximately $10^{-19}\ cm^2 s^{-1}$ at room temperature, but surface diffusivity in electrolyte solutions was found to be approximately $10^{-14}\ cm^2 s^{-1}$ (*17*). This 4-5 order of magnitude increase in an electrolyte allows surface diffusion to be the primary diffusion mechanism during dealloying without introducing unrealistic bulk diffusion rates or vacancy concentrations.

The working model for electrochemical dealloying was introduced in 2001 by Erlebacher et al. using a combination of kinetic Monte Carlo (KMC) simulations and numerical solutions (*9*). In this model the interface evolution (leading to porosity evolution) is described as the result of two competing kinetic processes: surface roughening (caused by dissolution of the less noble component, LN) and surface smoothening (caused by the remaining more noble component, MN, passivating the surface).

The mechanistic model is illustrated in Figure 1.2. Thermodynamically, dealloying is favorable above a particular critical electrochemical potential, V_c, which balances the free energy reduction associated with dissolution into solution with the energetic penalty associated with any new roughness and surface area created (*18*). During dissolution, LN atoms from low-coordination surface sites are easily solvated and dissolve into the electrolyte, Figure 1.2a (*19*). Dealloying is analogous to crystal growth, where the dealloying interface advances through layer-by-layer dissolution compared to layer-by-layer growth in thin film systems. It follows

that the rate-limiting step of nanoporosity evolution is the dissolution of an atom from a high-coordination site such as a terrace (*20*), which leads to the creation of a terrace vacancy that then grows laterally into a vacancy cluster as lateral near-neighbors are subsequently dissolved.

During dissolution the MN component is left on the surface as adatoms at high concentrations, Figure 1.2b. Using a regular solution model, it was shown that the equilibrium concentration of adatoms on the surface is very low (*19*) and the MN component will diffuse with the receding step edge. The MN atoms form island clusters, which grow into mounds as the dealloying process continues, Figure 1.2c. This a type of interfacial uphill diffusion (adatoms moving from low concentration areas to high concentration areas) mathematically describable by Cahn-Hilliard diffusion kinetics usually associated with spinodal decomposition (*8*). Eventually, the path length for diffusing MN atoms to travel to the MN-passivated mounds becomes too large and new MN-rich regions develop, bifurcating the pores, Figure 1.2d. Following this process of mound nucleation and bifurcation, porosity proceeds into the bulk and a bicontinuous structure is formed with a characteristic ligament and pore size, Figure 1.2e. At some point, it may be thought that transport of dissolved cations out of the porous layer becomes rate-limiting, but in practice this diffusion rate is nearly ten orders of magnitude faster than interface diffusion and electrolyte diffusion has never been observed to be rate limiting. Nanoporous metals, however, are metastable structures and, if left in solution, nanoporous metals will undergo post-dealloying coarsening, Figure 1.2f, to reduce their large interfacial area. As a result, the average ligament size increases and LN atoms left in the interior of the ligaments are exposed and dissolved. In an extreme case (as $t \rightarrow \infty$), the structure will coarsen into a large lump consisting only of the MN component.

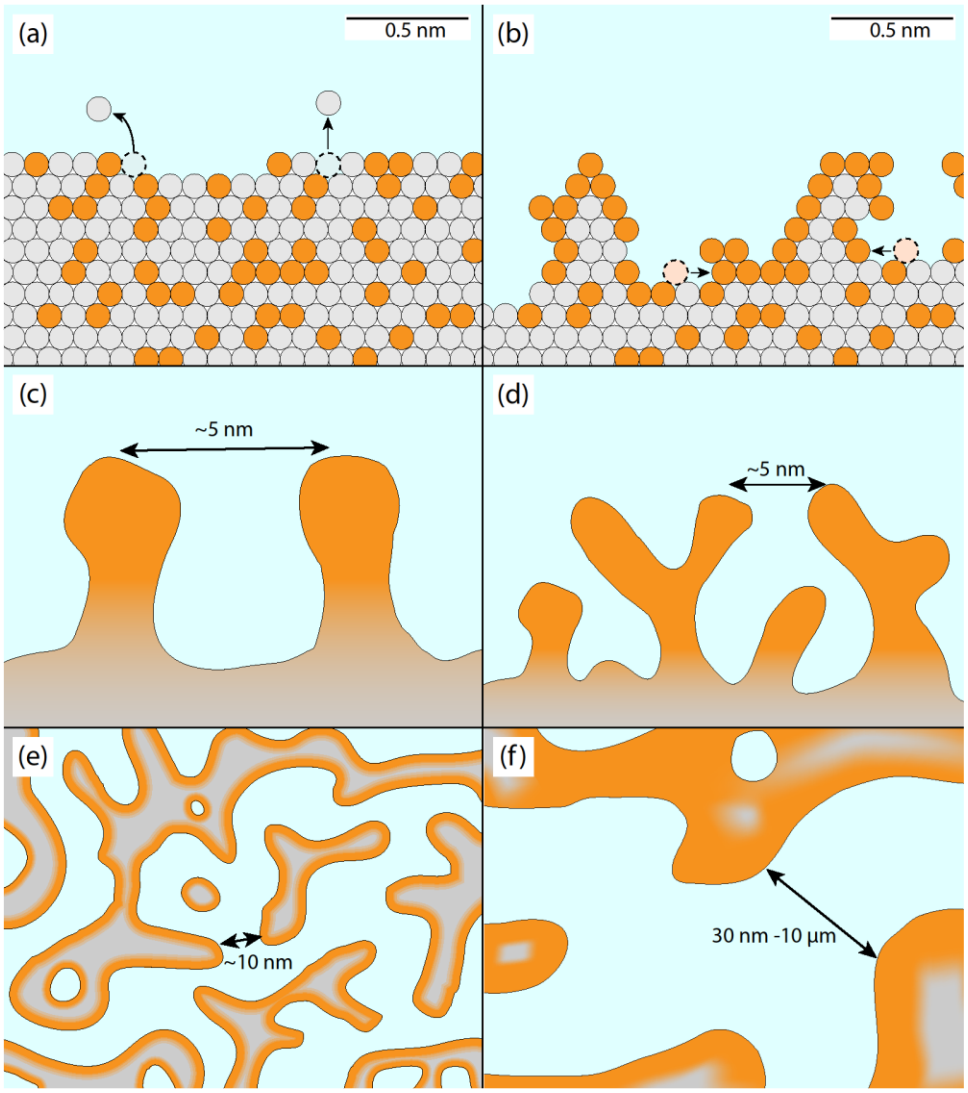

Figure 1.2. Illustration for selective dissolution and porosity evolution. (a) Dissolution of the less noble (LN) atoms from the parent alloy. (b) Surface diffusion of remaining more noble (MN) atoms attempting to passivate the surface. (c) Over time MN-rich island clusters form into mound, while their bases have a composition closer to the initial alloy. (d) The diffusion path length for future dissolution events becomes too large and new mounds are nucleated. (e) The resulting porous network has a characteristic ligament and pore size, with a MN-passivated surface, and LN-rich interior. (f) Over time, post-dealloying coarsening leads to an increase in the average ligament size and the ligament enrich in the MN component.

1.3 Parting limit critical potential, bicontinuous structure

Historically, dealloying systems have been characterized by two key parameters: the parting limit, or percolation threshold p_c, defined as the fraction of the LN species above which dealloying occurs, and the critical potential, V_C, defined as the minimum potential required for bulk dealloying. The parting limit and critical potential were defined early in the development of dealloying theory (*21*), but the understanding of both concepts have been refined in the last decade.

1.3.1 The Parting Limit

The parting limit is the critical alloy composition necessary for a structure to fully dealloy; this does not necessarily imply porosity evolution and only asks the question whether or not the dissolving liquid can travel from one end of the sample to the other. Another way of considering this problem is whether there is a network/chain of atoms (of the LN component), which goes through the entire sample. If the composition is below the parting limit the structure will not fully dealloy, and if the composition is above the parting limiting it will fully dealloy.

For electrochemical dealloying of Ag_xAu_{1-x} the parting limit is ~55 at.% Ag, however the percolation threshold for an fcc lattice is only ~20 at.%. Recent work by Artymowicz showed that this difference can be explained by considering high-density clusters (*22*). Specifically, the study examined the high-density percolation threshold $p_c(m)$, which denotes that a percolation chain/path exists composed of Ag atoms with at least m Ag near-neighbors. If we assume Ag atoms only need one Ag near-neighbor, $p_c(1)$, the critical threshold is ~20 at.%. If, however the number of near-neighbors is increased to nine the threshold isn't observed until

the Ag composition is at least ~ 60 at.%, i.e. $p_c(9) \approx 60$ (a value very similar to the observed parting limit). The percolation clusters at these higher concentrations are 2-3 atoms wider than $p_c(1)$, and it is thought that there is a geometric requirement for ion solvation; if the chain is too small the LN component is unable to coordinate with anions in solution and dissolve. Kinetic factors such as surface diffusion and dissolution can alter the observed threshold, however this has not been extensively studied.

1.3.2 The Critical Potential

The idea of a critical potential, V_C, is grounded in the field of corrosion science (*10*, *23*, *24*) and is an important concept because it represents the onset of selective dissolution. This has implications in corrosion and pitting corrosion of the important aluminum alloy 2024 as well as stress-corrosion cracking in brass and stainless steel alloys (*25*). The critical potential, however, is poorly defined by a potential sweep as can be seen in Figure 1.3. It is clear that as the potential increases, the current - associated with dissolution of the LN component - eventually increases exponentially. Unfortunately, the exact value of "the onset of selective dissolution" is unclear; empirically, it has been defined as the value when the current is above $\sim 1\, mA/cm^2$. Going back to our model in section 1.2, the critical potential is the value where the surface dissolution rate (itself a function of the applied potential) overcomes the passivation of the MN component (where the surface diffusivity is not a function of applied potential). The critical potential is a function of alloy composition, typically decreasing with decreasing LN composition. However, as the composition varies toward 100% of the LN component, the critical potential does not tend toward the reversible dissolution potential for that element, as would be expected, and instead was typically a few hundred millivolts higher (*18*). Erlebacher

(*19*) and Corcoran et al. (*26*) suggested that the critical potential usually observed was an artifact of the potential sweep rates used experimentally (*25*), and suggested an experimental protocol employing the observation of steady-state dissolution currents at different potentials to get at an "intrinsic" critical potential. The intrinsic critical potential is lower than earlier measurements with practical implications that the corrosion stability of alloys might be less than expected. Later, Rugolo and co-workers (*18*) developed a model for the intrinsic critical potential that gives its origin as that potential above which it is thermodynamically favorable to dissolve a region of volume corresponding to a pore diameter one atom deep in the dealloyed material.

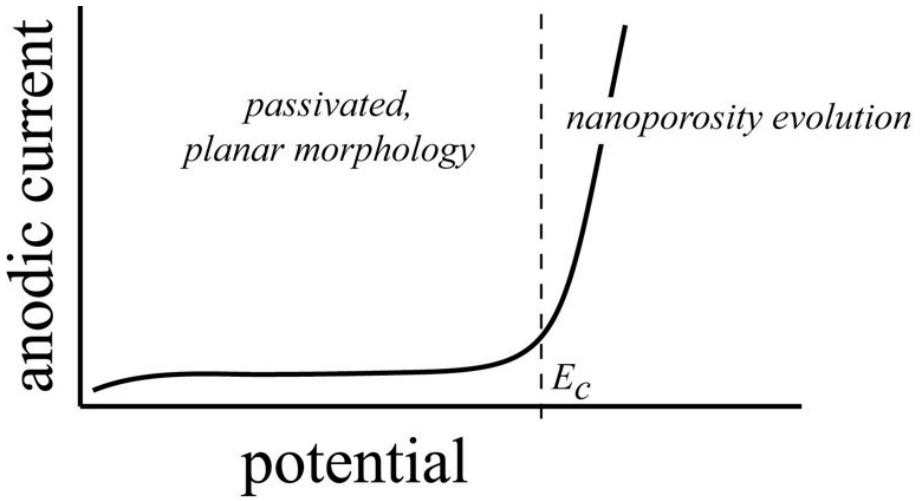

Figure 1.3. Potential sweep curve for a binary dealloying system. As the potential increases the current eventually dramatically increases, representing the onset of dissolution (the critical potential). This onset, however, is poorly defined and can depend on the sweep rate, electrolyte, and electrolyte concentration. As a result there have been refinements as to how the critical potential is defined by holding at fixed potentials and observing the current decay over long periods of time.

1.3.3 Bicontinuous Structure and Coarsening

The structure of nanoporous metals is quite unique. Dealloying occurs within the initial grain structure of the metal so the grain structure of the parent alloy is preserved. To further illustrate this point, if the parent alloy has 1 mm diameter grains, then the dealloyed material

will also have 1 mm diameter grains, where each grain is nanoporous with ligaments maintaining the same crystal orientation throughout. Nanoporous metals have been compared to sintered structures, however, this is an incorrect statement because the porous networks are single crystalline within each grain and lack internal boundaries. Due to this feature, diffusion pathways are very large. This imparts unique geometric features to nanoporous metals: namely that they possess regions of positive, negative, and saddle point curvature in a topologically complex network. Such complex topologies have been of significant recent interest (*27–32*), and methods have been developed to describe the topology of nanoporous metals (*33*, *34*), while the dynamics of topology evolution have been studied by KMC and MD (*35*, *36*).

Coarsening of nanoporous metals is driven by thermodynamic surface energy reduction (*35–37*). The results of these studies indicate that structure evolution tends to proceed via pinch-off Rayleigh instabilities which reduce the local genus (the number of "handles" in the structure). One implication is that inverse Rayleigh instabilities - a tunnel breaking up into a series of voids - can also occur, which in turn explain the TEM observations of large voids within the ligaments of np-Au reported in (*38*).

1.4 Conditions for electrochemical dealloying/limits of tunability

One reason for the growing popularity of studying dealloyed nanoporous metals is that they are very easy to make. A homogeneous alloy precursor, of whatever shape or form factor, is simply immersed into an acid that selectively dissolves one component away. As long as the remaining component is free to diffuse along the acid/alloy interface, porosity generally forms. However, the major drawback to this technique is that there are several requirements for porosity evolution (*19*):

1. The electrochemical reduction potential between the MN and LN components needs to be several hundred millivolts. For instance, in the Ag-Au system, the difference between the standard reductions potentials of Ag and Au is $\sim 1V$. However, in the Ni-Cu system – which does not evolve porosity – the difference in the two standard reduction potentials is $\sim 500\ mV$. The critical potential of an alloy system typically sits between the reduction potentials of the two elements; in the case of Ni-Cu it is difficult to perform selective dissolution, and both elements simultaneously dissolve. Certain chemical tricks can be used to achieve potential-independent selective dissolution, but this has only been reported for one system.
2. The parting limit imposes a restriction on the composition range to fabricate a porous material. Below the parting limit the system is passivated and porosity does not occur. There is also an upper limit on the alloy composition where if there is too little of the MN component the structure does not hold together. This is difficult to predict a priori and the parting limit can vary system to system. For instance, Zn-Cu systems only require 20 at.% of the LN component for porosity evolution to occur.
3. The alloying components must form a homogeneous solid solution. This is not a strict requirement, in fact intermetallic and glassy alloys have been dealloyed, but these structures do not have uniform ligament sizes. As a result, reporting size-dependent properties becomes difficult.
4. The final requirement is that the surface diffusivity of the MN component needs to fall within a certain window, i.e. a Goldilocks Principle: If the surface diffusivity

is too low the MN clusters, and subsequent mounds (Figure 1.2), are unable to form. The system will dealloy but porosity evolution will not occur. Conversely, if the surface diffusivity is too high the structure will passivate and bulk dealloying will occur.

Due to these requirements, dealloying has been restricted to noble-metal systems, Figure 1.4, which are often expensive and are limited to catalysis applications. This figure illustrates the lack of diversity of porous materials at the start of my PhD studies (2010) and will be compared with the current state of dealloyed materials in Chapter 6.

1.5 Liquid Metal Dealloying

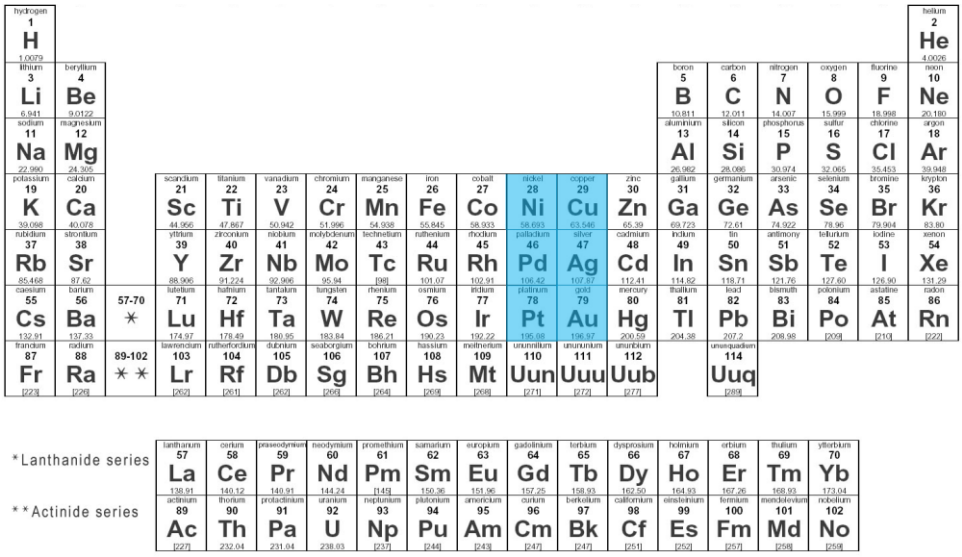

Figure 1.4. Periodic table showing the elements (highlighted blue) which have been successfully fabricated into nanoporous metals via dealloying. Note that all of the elements are noble metals, demonstrating the limitations of current dealloying techniques.

The requirements laid out in section 1.5 demonstrate that although electrochemical dealloying is an easy technique, it can only be applied to metal systems that meet certain requirements. Elements that are prone to oxidation, such as Ti or Al, can never be fabricated

by electrochemical techniques, and atoms with slow surface mobilities (e.g. Ta, W), will not diffuse fast enough to form porous structures. The concept of dealloying has recently been generalized to be any form of liquid-mediated dissolution, representing a paradigm shift in this community.

Harrison & Wagner (*39*) first examined this idea in 1959 by looking at metal alloy corrosion in molten metals and salts, but this idea did not catch on until Kato and coworkers (*40*) reported making porous Ti in 2011 by dealloying Ti-Cu alloys in molten Mg. Analogous to the critical potential, the dissolving component has a negative enthalpy of mixing with the liquid phase, which thermodynamically drives the dissolution process. Unlike electrochemical dealloying, dissolution is always favorable and there is no critical potential. Preliminary studies of liquid metal dealloying (LMD) have shown that the morphologies are similar to electrochemical dealloying, which is to be expected as long as the two competing mechanisms (dissolution and surface diffusion) are the same (*41*, *42*). We will come back to this concept in Chapter 3 for the development of new alloy systems.

1.6 Mechanical Properties

Nanoporous metals are an attractive material for structure applications because they consist of ~10^{18} nanoscale objects (for 10 nm ligaments in 1 cm^3 of material), and should have similar size-dependent strengthening – increasing strength with decreasing size – as is seen in micropillar and nanowire systems. The wealth of the work on the size-dependence of the yield strength in nanoporous metals has been performed on np-Au, however, the scaling laws are expected to be the same for all bicontinuous nanoporous metals. The mechanical properties of np-Au have been examined by many research groups using a variety of mechanical techniques

including tension, compression and hardness testing (*43–69*). A compilation of the data is given in Table A.1 and Figure 1.5. There is significant scatter (addressed below), however the data demonstrates an overall increase in strength with decreasing ligament size, suggesting that there is an expression to relate the strength of the porous material to its feature size.

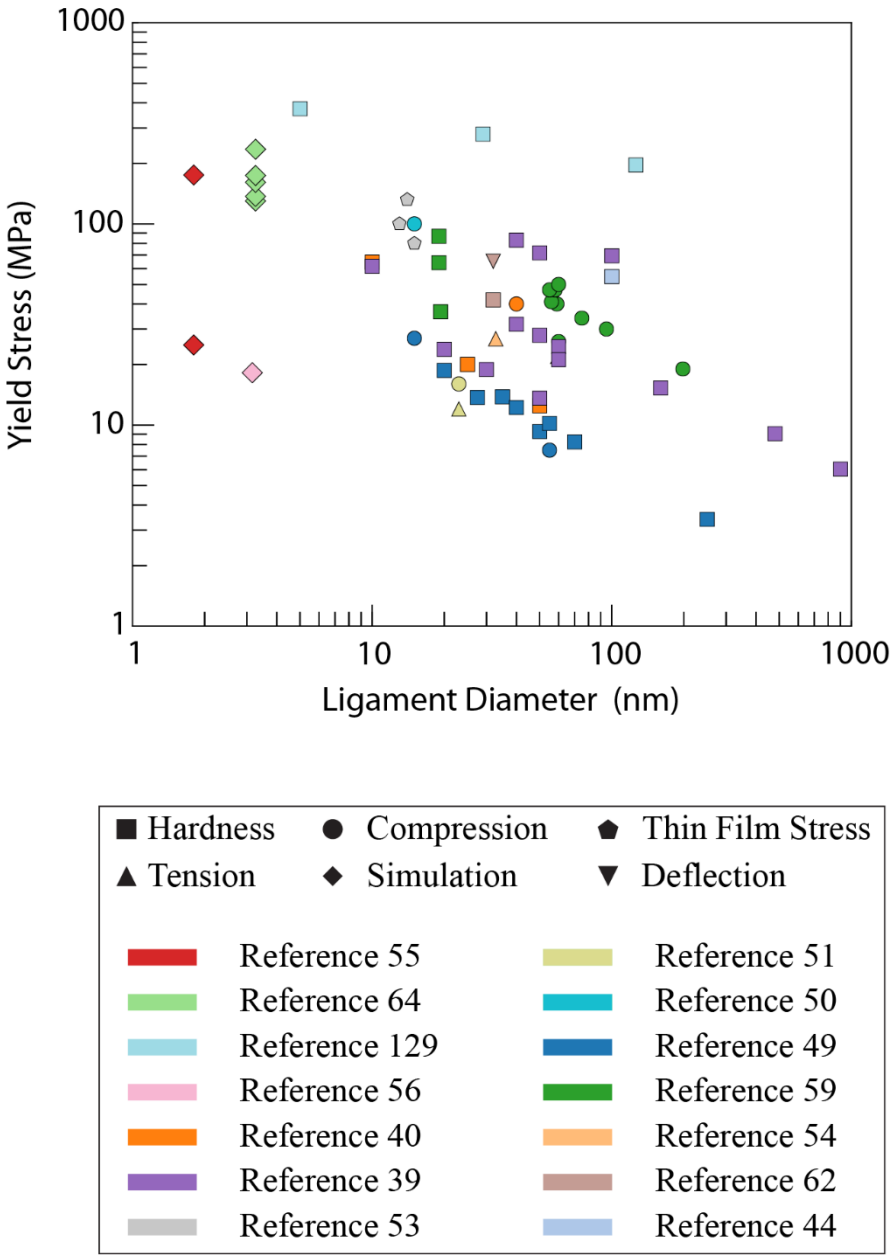

Figure 1.5. Yield strength versus ligament size for reported values of np-Au in the literature from various mechanical tests: hardness values (square), compression values (circle), thin film stress values (pentagon), tension values (triangle), simulation values (diamond), and deflection tension testing (upside-down triangle). It is apparent that there is a trend of increasing strength with decreasing ligament size, however there is a large amount of scatter associated with samples having different relative densities.

1.6.1 Scaling Laws and Gibson-Ashby Relations

Despite being a network of connected nanostructures, nanoporous metals are still high-density foams and have decreased mechanical properties compared to their fully dense nanowire, micropillar, or nanocrystalline counterparts. The underlying strength of nanoporous metals are commonly estimated using the empirical Gibson-Ashby (GA) relations for foams (*70*). The GA equations for the yield strength and elastic modulus of a foam are given by

$$\sigma_y^{foam} = C_\sigma \sigma_y^{bulk} \left(\rho^*\right)^{n_\sigma} \tag{1.1}$$

$$E^{foam} = C_E E^{bulk} \left(\rho^*\right)^{n_E} \tag{1.2}$$

Here, C_σ and C_E are geometric constants taken to be $C_\sigma = -0.3$ and $C_E = -1.0$, σ_y^{bulk} and E^{bulk} are the bulk yield strength and elastic modulus, ρ^* is the relative density of the material ($\rho^* = \rho^{foam} / \rho^{bulk}$), and both n_σ and n_E are exponents dependent on the microstructure of the solid material, but taken to be ~ and ~ , respectively, for bending-dominated behavior. It has been noted in simulations by Sun et al. (*71*) that ligaments in np-metals undergo both bending and tensile deformation, and the values for C_σ, C_E, n_σ, and n_E need to be carefully considered when being applied to a particular system of materials. The values of C_σ and n_σ will be addressed in Chapter 5.

Previous work by Hodge and coworkers (*46*, *49*) expressed the size-dependence using a Hall-Petch relationship, but individual ligaments are not constrained by adjacent grains and the ligaments are more aptly compared to micropillars/nanowires as suggested by several other research groups (*43*, *57*, *61*, *66*, *67*). The equation for the yield strength as a function of ligament size is given by

$$\sigma_y = \sigma_o + A\lambda^{-m}, \tag{1.3}$$

where σ_o is the scale-independent yield strength, λ is the ligament size, and A and m are empirical constants. The first term is very small and can be neglected (*72*), and the yield strength becomes

$$\sigma_y \cong A\lambda^{-m}. \tag{1.4}$$

Combining the yield strength and Gibson-Ashby relation yields the equation

$$\sigma_y^{foam} = C_\sigma A\lambda^{-m}\left(\rho^*\right)^{n_\sigma}. \tag{1.5}$$

Note, however, that the power-law relationship is grounded in statistics. Specifically, the power-law relationship in micropillars is linked to the probability of finding the maximum size of a dislocation source in a material with a given diameter and dislocation density, as discussed in recent work by El-Awady, who established a size-dependent Taylor-strengthening law for dislocation-mediated plasticity in micropillars (*73*). El-Awady points out that the strengthening mechanism relies heavily on the dislocation density in the material and, in the case of plasticity, knowledge of the kinetic evolution of the dislocation density of the material during deformation. Unfortunately, to our knowledge there have only been two qualitative studies of dislocation microstructure in micropillars (*74*, *75*), let alone for nanoporous metals, and we cannot compare Eq. (1) with this more rigorous model.

There is no size-dependent scaling law for the elastic modulus of nanoporous metals because it is not expected to change dramatically above 10 nm as pointed out by Weissmuller et al. (*48*). Large sample (mm-scale) experiments have shown dramatic manifestations of elastic behavior such as macroscopic actuation caused by electrocapillary forces (changes in surface stress with applied electrochemical potential) in solution and gas-phase environments (*3*, *76–80*).It has been suggested that excess elasticity on the surface might decrease or increase the elastic modulus, and was reported in simulations of materials with 2-4 nm ligaments by

Sun et al. and Farkas et al. (*62*, *71*), but experiments in nanoporous metals generally show no change in modulus. One set of experiments by Mathur & Erlebacher inferred the modulus of np-Au by examination of the buckling of thin films (*81*), showing an increase in the modulus with decreasing ligament size, but the authors argued that it was a geometric manifestation and did not originate from the ligaments. The effects of capillary forces and altering the surface stress of nanoporous metals have been discussed in detail previously and can be found in Reference (*48*) and those therein.

1.6.2 Dislocation Activity

Dislocation activity in nanoporous metals is expected to be different because individual ligaments are observed to be ductile, but the bulk structure tends to be brittle (at least in tension). This was first observed in a fracture toughness study by Li and Sieradzki (*82*) where a ductile-brittle transition was observed in np-Au when the sample size was significantly larger than the ligament size. Pure tension tests confirmed this brittle behavior (*58*, *61*, *69*), contrasting with the ductile behavior observed in compression and hardness testing. This tension-compression asymmetry was observed in MD simulations by Farkas et al. (*62*), but only for ligaments below 15-20 nm and was attributed to the surface stress response of the ligaments.

TEM experiments, MD simulations, and an EBSD study all showed significant dislocation activity inside the ligaments, even at sizes as small as 3 nm (*60*, *62*, *63*, *67*, *71*). Due to the small ligament sizes in these samples, perfect dislocations are not observed but there is a large density of twins, stacking faults, and Shockley partial dislocations. MD simulations showed that Shockley partials are emitted from the surface, and quickly pass through ligaments, leaving

behind twins and stacking faults. TEM studies confirm these observations and noted that this behavior is similar to pure Au wires 50 nm in diameter. In fact, dislocations don't always terminate on the surface, and can move through ligaments and eventually into nodes. An EBSD study on 55 nm ligament np-Au by Jin and coworkers (*56*) demonstrated the evolution of a dislocation cell structure, suggesting dislocations in porous metals were able to move a distance larger than the ligament diameter and can be stored.

All of this work suggests that nanoporous metals are ductile, at least locally, and it is difficult to have coherent, macroscopic plasticity where a dislocation can travel large distances though the highly porous network. Dislocations easily terminate on surfaces and uniform deformation is impossible. This informs understanding of the brittle behavior in tension, whereas compression testing masks this lack of coherency either through densification or inherently preventing early catastrophic failure. We will discuss these limitations and design strategies for new bicontinuous structures in Chapter 5.

Chapter 2 Dealloying in Finite Systems

2.1 Summary

In this chapter we examine dealloying in binary nanoparticles in order to understand how porosity evolves in confined systems where the chemical potential term dominates. The Gibbs-Thomson effect (the reduction of local chemical potential due to nanoscale curvature) predicts that nanoparticles of radius r dissolve at lower electrochemical potentials than bulk materials, decreasing as $1/r$. However, we show here that if the particle is an alloy –susceptible to selective dissolution (dealloying) and nanoporosity evolution – then complete selective electrochemical dissolution and porosity evolution requires a *higher* electrochemical potential than the comparable bulk planar material, increasing empirically as $1/r$. This is a kinetic effect, which we demonstrate via kinetic Monte Carlo (KMC) simulation. Our model shows that in the initial stages of dissolution, the less noble particle component is easily stripped from the nanoparticle surface, but owing to an increased mobility of the more noble atoms, the surface of the particle quickly passivates. At a fixed electrochemical potential, porosity and complete dealloying can only evolve if fluctuations in the surface passivation layer are

sufficiently long-lived to allow dissolution from percolating networks of the less-noble component that penetrate through the bulk of the particle.

2.2 Background

Porosity evolution can occur during dealloying when the dissolution rate is fast enough relative to the surface diffusion rate of the undissolved component, with ligament and pore sizes in some cases less than 5 nm. Dealloying has been used to fabricate bulk metals for catalysis with high surface areas, however this form factor is not always useful (*12*, *83*, *84*). In the case of bulk np-NiPt, the mass activity for oxygen reduction drops as porosity extends into the bulk of the material. A function of the overpotential, oxygen will diffuse an average distance before being reduced to water. This suggests that there is an optimum dealloying depth for a porous catalyst and it is useful to consider finite systems. In the case of a nanoparticle, the diameter can be finely tuned and it can be dealloyed to produce a nanoporous nanoparticle.

Dealloyed nanoparticles are potentially excellent electrocatalysts (*85*, *86*), combining the high surface area/volume features of traditional nanoparticles with the ability to tune composition and morphology for improved functionality. Nanoporous particles offer additional functionality because the porous region can be filled with secondary phases to form nanoreactors (*12*). Nanoporous metals generally exhibit unusual physical behavior associated with their structure including nanoscale manifestations of thermodynamic surface stress (*87*) and high magnetoresistance (*88*). Typically dealloying of nanoparticles is accomplished by electrochemical potential cycling between prescribed voltage limits, sometimes yielding a variety of dealloyed nanoparticle types including core-shell and nanoporous structures.

Thermodynamically, dealloying is favorable above a particular critical electrochemical potential E_{crit} that balances the free energy reduction associated with dissolution into solution with the energetic penalty associated with any new roughness and surface area created (*18*). The energy gain associated with electrochemical dissolution is a strong function of the curvature of the surface, and for single component materials the electrochemical potential decreases with particle radius r as a function of $1/r$ due to the Gibbs-Thomson effect (*89*, *90*). The electrochemical stability of nanoparticles has been previously studied, and the relationship for the dissolution voltage (in millivolts) is given as:

$$E_{M/M^{n+}}(r) = \overline{E}_{M/M^{n+}} - \frac{\gamma_M \Omega_M}{nF}(2/r) \tag{2.1}$$

where $E_{M/M^{n+}}(r)$ is the size-dependent standard reduction potential of the metal species M, $\overline{E}_{M/M^{n+}}$ is the bulk standard reduction potential, γ_M is the surface energy, Ω_M is the molar volume, n is the number of electrons per mole product, F is the Faraday constant, and r is the radius of the nanoparticle. Using standard values for $Pt^{2+} + 2e^- \rightleftarrows$, the relationship becomes:

$$E_{Pt/Pt^{2+}} = 1011 - 133(2/r)\ mV \tag{2.2}$$

An experimental plot of the stability of Pt nanoparticles can be seen in Figure 2.1. The effect does not become dramatic until the radius is smaller than 2 nm, however there is a $200\,mV$ difference between the bulk value and a 2 nm radius particle, which is significant for an industrial application.

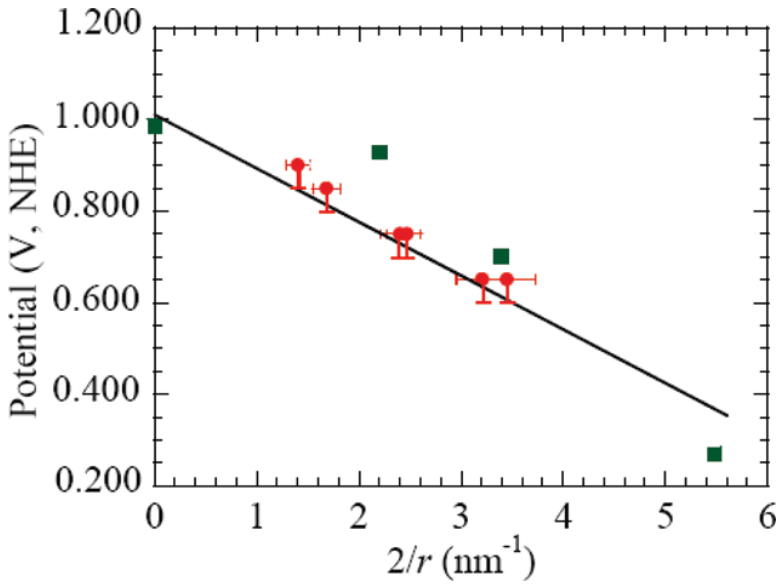

Figure 2.1. Electrochemical dissolution potential versus $2/r$ for Pt nanoparticles from Ref. (*89*). This decrease in stability reflects a lower limit on Pt nanoparticle size for catalytic applications.

It might be expected that the potential at which porosity forms in a nanoparticle should also decrease with decreasing radii, but here we report the results of kinetic Monte Carlo simulations (KMC) showing that this potential actually *increases* with $1/r$ in alloy nanoparticles. The origin of this effect lies in the details of nanoparticle alloy dissolution – generally, regardless of potential, dealloying nanoparticles initially and quickly tends to form noble-metal passivated particles. Porosity only forms over longer timescales if the dissolution rate is high enough to form pits during transient surface fluctuations that expose less-noble atoms buried under step edges to the external environment. Such surface fluctuations increase in frequency but decrease in duration with smaller particle size because of the rise in surface mobility associated with the Gibbs-Thomson effect (such fluctuations can be considered the initial manifestation of the melting point suppression in nanoparticles).

2.3 Experimental Methods

To study selective dissolution in alloy nanoparticles, we used the KMC simulation code MESOSIM, a full description of which can be found in Ref. (*19*). Briefly, MESOSIM has been optimized to reflect time and energy scales associated with the prototypical Ag-Au dealloying system (leading to np-Au), but the general trends here should be applicable to dealloyable systems that remain single phase. Simulations are initialized by placing atoms on a 3-dimensional fcc lattice and the type of atom (Ag or Au) is assigned at random based on a weighted probability determined by the composition of the alloy. The time evolution of the system is governed by the KMC algorithm. In KMC, if there are N total events that can occur, each one indexed by i and possessing rate k_i , the time for a single event to occur is $\Delta t = -\ln \xi \Big/ \sum_{i=1}^{N} k_i$ where ξ is a random number in (0,1]. Within this time the probability of an event occurring is $P_i = k_i \Big/ \sum_{j=1}^{N} k_j^{-1}$. KMC simulations progress by picking a random event according to its weighted probability (more unstable events are weighted heavier than stable ones) and then the time is incremented accordingly. Our model here draws on the model introduced in Ref (*91*) and uses a simple bond-breaking model to capture the generic morphological evolution physics occurring over experimental timescales. Specifically, rates for surface diffusion and dissolution at a potential ϕ are given by the expressions $k_{diff} = v_1 \exp\left[-\frac{nE_B}{k_b T}\right]$, and $k_{diss} = v_2 \exp\left[-\frac{nE_B - \phi}{k_b T}\right]$, where $v_1 = 10^{13}\,\text{sec}^{-1}$, $v_2 = 10^4\,\text{sec}^{-1}$, $E_B = 0.15\,\text{eV}$ for all bond energies, and n is the number of bonds. These parameters have been shown in other studies to accurately model dissolution current vs potential behavior (*8*, *91*, *92*) the parameters also successfully model coarsening in nanoporous nanoparticles (*35*)

that agree with timescales of experimental studies of coarsening of np-Au (which we note are generally much longer than any of the timescales discussed in this work) (*93*); and recently an experimental measurement of the activation barrier for dissolution of Ag from a terrace site was measured, and found to be consistent with a bond energy between 0.1-0.2 eV (*20*).

2.4 Results and Discussion

Figure 2.2 shows a representative time evolution of a simulated nanoparticle of radius 30 and composition 75 at. % Ag. Overall, three different compositions were examined: 65, 75, and 85 at. % Ag; and four different nanoparticle radii: 8, 11, 18, 30 $\pm$ 1 atom diameters. These values approximately correspond to nanoparticle diameters of ~4, 6, 10, and 17 nm. The compositions were chosen to be representative of the composition range typically found in porosity-forming dealloying systems (*8*, *19*). Smaller particles were not studied because the roughness that evolved in the initial stages of dissolution was greater in amplitude than the particle diameter, and porosity never evolved. Particles were dealloyed under constant potential at $300\,\mathrm{K}$ and ran between 10^4-10^5 simulated seconds or ~5×10^8 iterations. The behavior exemplified by the particle in Figure 2.2 shows the following characteristics: (a) at short times, $t < 10^2$ sec., the outmost silver atoms are quickly stripped. Unlike the case of a bulk, planar surface, there are always low-coordination Ag atoms sitting at step edges at facet boundaries that facilitate such stripping; (b) at intermediate times $t < 10^3$ sec. , the particle is passivated with a monolayer of gold, which surface diffuses until the particle approaches the equilibrium Wulff shape (if we start the simulations with particle shapes already equilibrated to the Wulff shape rather than a sphere, our results are unchanged); (c) over long time periods, regions of the bulk are exposed to the external environment due to fluctuations in the outermost

layer; (d) in some cases, these fluctuations are long-lived enough to allow further attack into the interior of the nanoparticle. An important point here is that fluctuations exposing the interior also appear in stage (a), but the concurrent dissolution of the outermost silver is roughening the surface so quickly that there are always nearby gold atoms that can diffuse into terrace vacancies resulting in transient passivation.

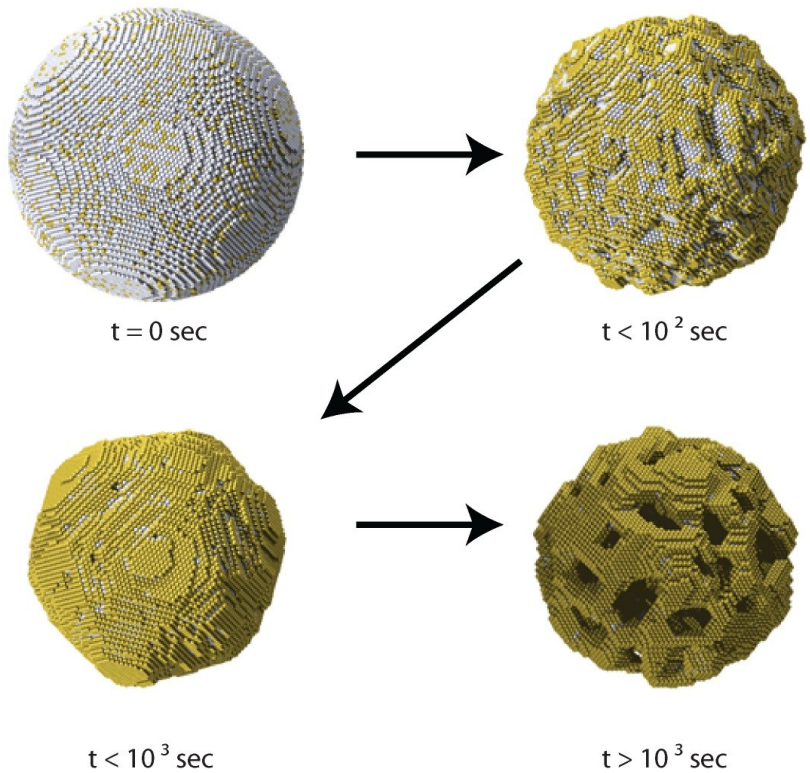

Figure 2.2. Time evolution of a simulated Ag-Au (white spheres: Ag; dark spheres: Au) nanoparticle (r = 30, 75 at. % Ag) under constant potential ($\phi = 0.98\,eV$). Initially the surface is Ag rich; it is easily stripped off and the surface roughens. The remaining Au atoms quickly form a passivating monolayer and a pseudo-equilibrated Wulff shape; eventually, a long-lived surface fluctuation reveals a percolating network of silver atoms in the bulk that dissolves to form a nanoporous nanoparticle.

In dealloying of bulk planar materials, the critical potential is a sharp threshold separating porosity formation from surface passivation (*25*). Analogously in nanoparticles, we find an increase in the propensity for porosity evolution to exist as the electrochemical potential

increases, but this threshold is not sharp. To quantify this observation, for each particular radius and electrochemical potential we generated a histogram over the course of many runs (Figure 2.3), typically many thousand, showing the final volume of the particle after being subjected to a dissolution potential for some fixed, but long, period of time (10^4 sec).

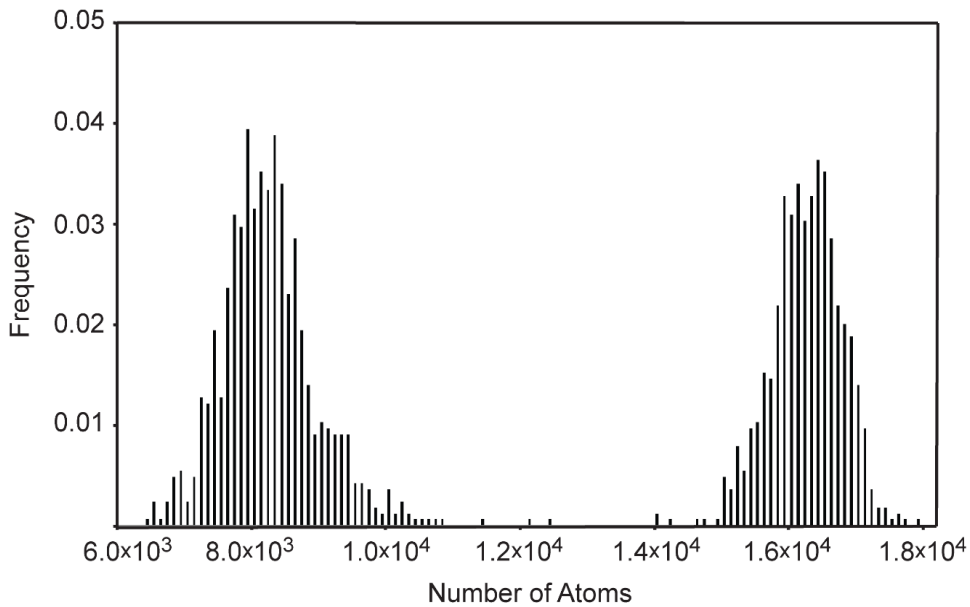

Figure 2.3. Histogram data of 2000 runs of a r = 18 particle, 85 at. %Ag, under constant dissolution potential $\phi = 0.975\,eV$. The Gaussian at smaller number of atoms corresponds to dealloyed and porous nanoparticles while the Gaussian at larger number of atoms corresponds to passivated, but non-porous nanoparticles. The initial number of atoms for this particle radius was approximately 3.68×10^4.

Near a potential for porosity evolution E_P, distinct from and larger than the critical potential for the bulk planar alloy, we see two Gaussian distributions corresponding to two final particle volumes. The distribution at smaller volume corresponds to fully dealloyed and porous particles that have lost the majority of their less-noble component mass, and the other corresponds to particles that have undergone only superficial surface dealloying and become passivated with the noble component. For this latter case, there is still a significant amount of

the less noble component buried in the particle. We define E_P as that potential where the area of each Gaussian distribution is equal. We note that by the particular time at which the mass distribution was assessed (10^4 sec.), the distribution had reached a steady state; that is, we occasionally checked that non-porous particles subjected to the potential E_P over a time 10^4 do not dissolve further even if the simulations are run for an order of magnitude in time longer.

Figure 2.4 shows E_P for the three compositions plotted against the inverse particle radius. For reference, bulk values for the critical potential reported in Ref. (*19*) are plotted at $1/r = 0$. Most notably, the potential associated with porosity evolution E_P is seen to *increase* as the particle size decreases.

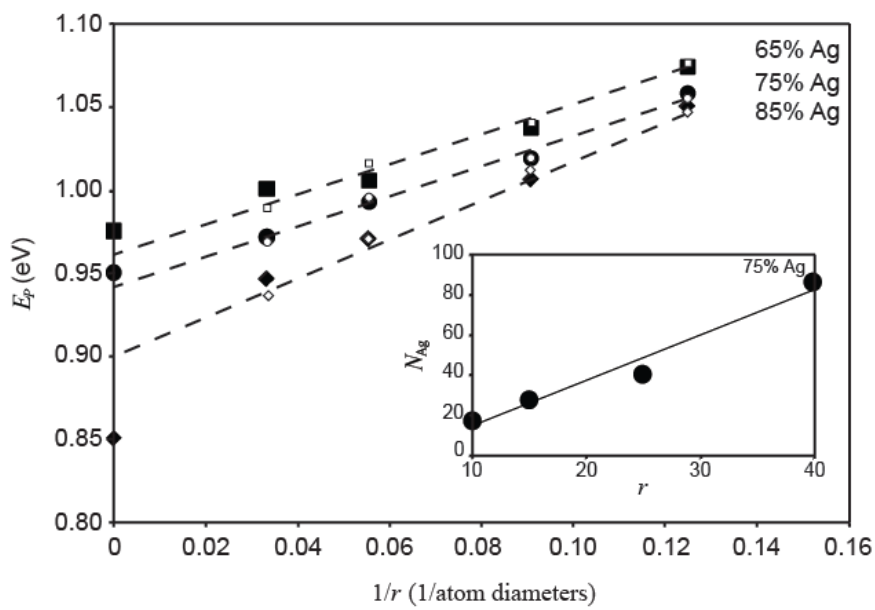

Figure 2.4. Simulation and model data for the potential for porosity evolution E_P versus $1/r$. (closed symbols) measured simulation values (symbols at $1/r = 0$ correspond to values of the critical potential reported in (*19*)); (open symbols) predicted values of EP using the model, Eq. (2); (grey symbols) simulation values for the critical potential for bulk porosity evolution (from Ref. (*19*)). Linear fit of the predicted values of E_P using Eq. (2) (dashed lines), shows an approximate $1/r$ dependence, and also shows that E_P generally sits at a potential higher than the bulk critical potential. (inset): the number of silver atoms in 9- coordinated sites $N_{Ag}(0)$ as a function of radius for a 75 at.% particles.

This observation should not be interpreted to mean that it is more difficult energetically to dissolve silver atoms from smaller particles than from larger ones. All the particles here quickly lose silver from their initial surface, and, in accordance with the Gibbs-Thomson effect, at fixed potential smaller particles tend to lose their surface silver more quickly because they have a higher fraction of low-coordinated step and kink sites (*90*). However, for the same reason, the gold atoms left behind on the alloy particle surface are much more mobile on the smaller particles and thus quickly passivate the interior. It is possible that reduction of the ratio k_{diff}/k_{diss} could reduce such passivation at a fixed particle size and potential, but it is unclear how to experimentally achieve this.

We necessarily conclude that E_P is fundamentally kinetic in origin, containing a complex choreography of surface composition fluctuations convoluted with the geometric connectivity of the more reactive component under the passivating gold surface. The ingredients that need to be included in a kinetic model for E_P include:

(i) An observation that the initial stage of porosity evolution in particles must be gold-passivated particles and not a surface with an appreciable concentration of silver. After this initial stage, there are a few silver atoms exposed on the surface on the low-index facets, but the majority of silver atoms still on the surface sit along facet boundaries in 10- and 11-coordinated sites (see, for instance, Figure 2.5). For this reason, the number of exposed silver atoms at this stage of evolution increases approximately linearly with the particle radius.

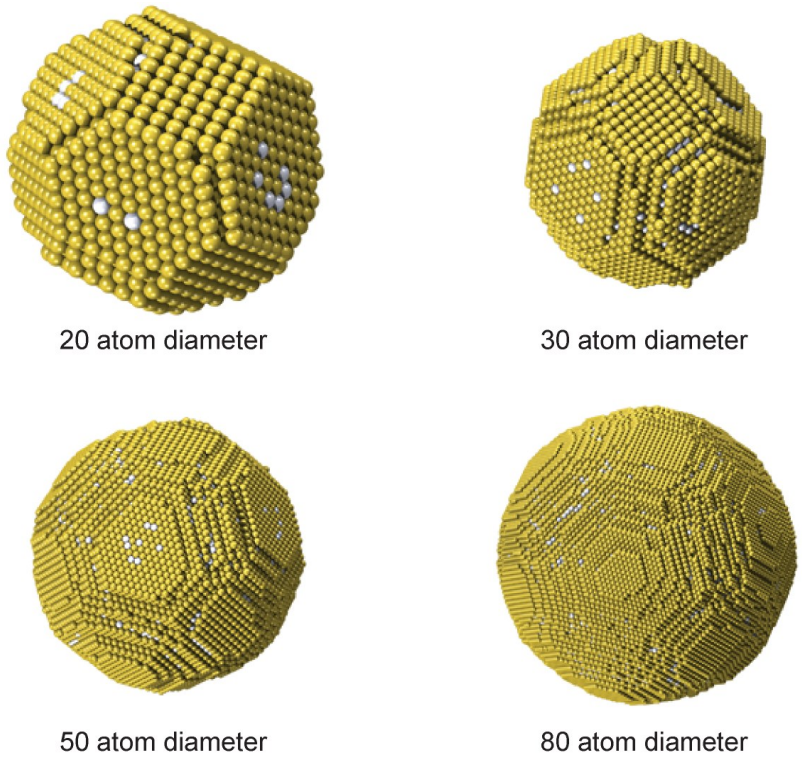

Figure 2.5. Snapshots of passivated particles as a function of particle size. As the particle size increases the fraction of silver atoms on terrace sites decreases and the majority are found underneath step edges.

(ii) The majority of surface diffusion events that can lead to further exposure of silver to the electrolyte, or reduction of silver coordination, are fluctuations at step edges that reduce the coordination of 10- and 11-coordinated silver atoms to 9-coordinated terrace sites susceptible to attack by electrolyte. Over long periods of simulated time, of order 10^4 sec, many Ag atoms are transiently exposed to the electrolyte. The 9- coordination number corresponds geometrically to a terrace atom in a (111)-oriented surface, and it has been shown that this is likely the maximum coordination for which dissolution occurs (*20*, *22*); physically, more highly coordinated atoms are thought not to be sterically complexable by anions in solution. Within the model, the lifetime of the fluctuation exposing Ag atoms is independent

of the dissolution potential. At the very least, for porosity to form, this lifetime must be larger than the average time to dissolve silver from such a terrace site (Figure 2.6).

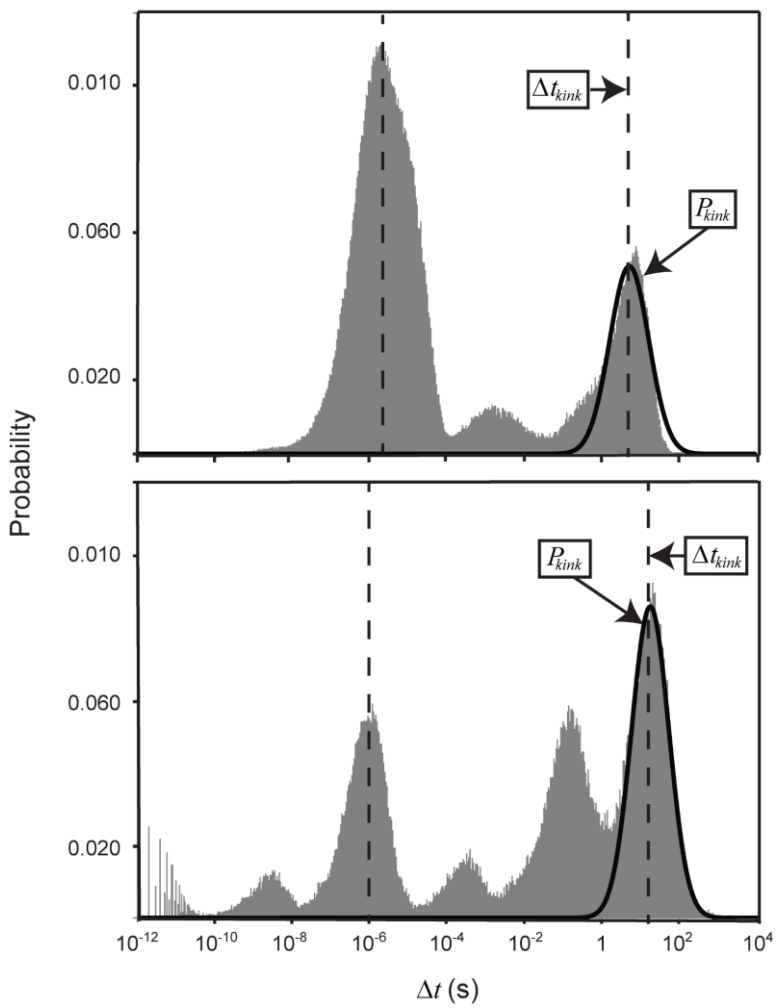

Figure 2.6 Surface fluctuation lifetime data for r = 8 particles (top) and r = 30 particles (bottom). The time interval Δt is the lifetime of a 9 Ag atom coordinated terrace site. The peak at $\sim 10^{-6}$ sec. corresponds to surface fluctuations associated with adatom motion, and the peak at ~10 sec. corresponds to fluctuations at kink sites. We set Δt_{kink} to the center of the latter peak, and the area under the kink distribution to P_{kink} .

(iii) Finally, assuming the Ag atom is dissolved within the lifetime of a surface fluctuation, porosity can form only if the surface Ag atom is connected to a percolation network of other Ag atoms through the bulk of the particle. In contrast to the early stages of dissolution,

where there are many Au atoms diffusing on the surface that are readily available to passivate low-coordinate surface defects, the surface vacancies associated with dissolution of silver atoms during these surface fluctuations are very long-lived. As a result, we observe that if a percolation network of silver atoms starts to dissolve after the particle has reached the pseudo-equilibrated Wulff shape, the entire particle will almost instantaneously dealloy and become porous. It can be seen in Figure 2.7 that the error associated with the probability a surface atom is connected to a percolation network becomes quite large as the particle size decreases. This is result of having a finite system and represents the length scales below which the existence of high-density percolation networks disappears. This results in a distribution of dealloyed morphologies in nanoparticles including porous, core-shell, and passivated nanoparticles

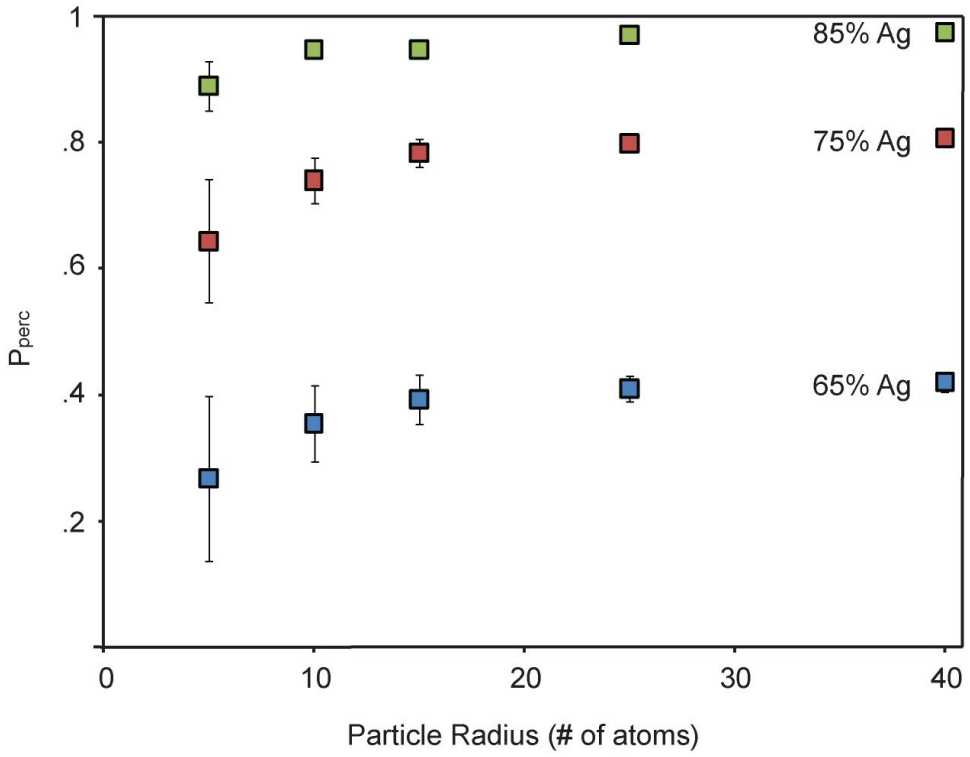

Figure 2.7 Probability that a surface silver atom is connected to a percolation pathway in the nanoparticle. If this atom is selected to dissolve the entire particle will evolve porosity. This probability is weakly size-dependent, but most importantly dependent on the alloy composition.

Taken together, these observations lead to a first order master equation describing the rate of change of the number of exposed 9-coordinated silver atoms N_{Ag}:

$$\frac{dN_{\mathrm{Ag}}}{dt} = -k_{diss} P_{kink} P_{perc} N_{\mathrm{Ag}} \tag{2.3}$$

Here, k_{diss} is the dissolution frequency from a 9-coordinated site, P_{kink} is the probability a kink site has fluctuated with large-enough amplitude to expose a silver atom, and P_{perc} is the probability this silver atom is connected to a percolation network into the bulk. Because a single dissolution event at this stage tends to lead to porosity evolution, the simplest criterion for E_P is determined by the condition that over a period of time Δt equal to the lifetime of the step edge fluctuation the surface silver concentration decreases by one: $N_{Ag}(\Delta t) \leq N_{Ag}(0) - 1$. Solving Eq. (2.3) under this condition and noting that the simulation rule $k_{diss} = \nu \exp\left[-\left(9E_B - E_P\right)/k_B T\right]$, we find E_P is determined by

$$E_P \geq 9E_B + k_b T \ln\left[\frac{-1}{\nu P_{kink} P_{perc} \Delta t} \ln\left(\frac{N_{Ag}(0) - 1}{N_{Ag}(0)}\right)\right] \tag{2.4}$$

The simulation model allows P_{perc}, $N_{Ag}(0)$, P_{kink} and Δt to be quantitatively measured independently. For percolation and $N_{Ag}(0)$, particle dissolution was halted upon completion of the passivation layer, and 9-coordinated silver atoms were counted and checked to see whether or not they belonged to a percolation network. A high-density percolation (HDP) threshold criterion was used to determine if a silver atom belonged to a percolation network, following Ref. (*22*), requiring Ag atoms to be counted in the percolating network if at least nine of its twelve potential neighbors are also silver. As discussed in Ref. (*22*), this criterion

is equivalent to the physically reasonable requirement that there be enough free volume around a surface silver atom for it to be solvated and dissolved by the electrolyte. Not surprisingly over the particle sizes examined, we find little size dependence of the probability of belonging to such a percolation network, with the probabilities equaling ~42%, ~81%, and ~97%, for compositions of 65, 75 and 85 at. % Ag, Figure 2.7. For $N_{Ag}(0)$, we find a weak linear dependence (see inset of Figure 2.4) on the particle radius, reflecting how most of the exposed silver atoms sit on facet boundary regions, the length of which increases linearly with particle radius.

The largest particle size-dependence is found for P_{kink} and Δt , the measures associated with fluctuations that lead to transient exposure buried of surface silver atoms. To quantify this effect, gold-passivated particles were again generated, but then silver atoms were not allowed to dissolve or diffuse during the further course of the simulation. These simulations tracked the time interval between a silver atom becoming 9-coordinated, and then becoming buried (i.e., re-passivated) by surface diffusing gold. Histograms of these time intervals for radius 8 and radius 30 particles are shown in Figure 2.6, and exhibit a rich complexity. For both particle sizes shown, we see that the majority of fluctuations are short-lived – 10^{-6} to 10^{-7} sec. – with a slight shift as the size increases to radius 30. These fluctuations are associated with gold adatoms moving over silver atoms embedded in terraces. Longer-lived fluctuations are associated with surface diffusion of gold with increasing coordination, so, for instance, the peak centered around 1 to 10 seconds corresponds to particular fluctuations of interest involving atoms at kink sites that expose 9-coordinated silver atoms. The difference in frequency distribution with particle size is straightforwardly explained as a Gibbs-Thomson effect: Surfaces on the $r = 8$ particles are extremely unstable and Ag terrace passivation is

controlled by adatom events, but as the radius increases the concentration of highly mobile low-coordination surface atoms decreases and a majority of the passivation events become controlled by lower-coordination surface atoms participating in attachment/detachment events at kink sites. As the longer-lived fluctuations are the ones that ultimately lead to porosity evolution, we associate P_{kink} and Δt with the longer-lived kink-site fluctuations, P_{kink} being the area under the peak associated with Δt_{kink}.

Using the independently measured values for the time interval, percolation and kink probabilities, and terrace concentration data into Eq. (2.4) we find good agreement with the model and the measured values of E_P (see Figure 2.4). The slopes for both the simulation and analytical models for 65 and 75 at.% Ag are approximately the same, but the slope for the 85 at. % simulation data is steeper than that predicted by Eq. (2.4). We resolve this discrepancy by noting that at high silver fractions, the pseudo-Wulff particle has approximately 15% of its surface silver atoms on (001) facets, in addition to the majority (111) positions. This means the average activation barrier for dissolution in this case is slightly smaller than $9E_b - E_P$. In fact, we find good agreement between model and simulation using $8.9E_b - E_P$ in Eq. (2.4) at the 85 at. % composition, as shown in Figure 2.4.

2.5 Conclusions

The work presented in this chapter impacts tuning the composition and morphology of dealloyed nanoparticles in the following ways. First, it may require surprisingly high electrochemical potentials to both fully dealloy a nanoparticle and ensure that every particle in a batch is porous. In experiments, this is often accomplished by electrochemical cycling which has the effect of "artificially" increasing the magnitude, lifetime and frequency of surface

compositional fluctuations. Second, the work here suggests that stymieing the surface mobility of the more noble (passivating) component can lead to more facile porosity evolution in nanoparticles, perhaps by adsorbing a self-assembled monolayer or dealloying under conditions where this component forms a stable oxide (*94*, *95*).

To summarize, the size dependence of surface site duration, percolation probability, and concentration of surface sites has been examined for binary alloy fcc nanoparticles. A first order rate equation provides a reasonable explanation of the increase in the electrochemical potential necessary for porosity evolution, and we identify the primary source of the increase to be a Gibbs-Thomson effect acting upon the gold-passivation layer on the particle. While for small particles there are many small fluctuations in the surface morphology, these fluctuations are too short-lived to lead to further dissolution. Porosity evolution occurs when fluctuations are long-enough lived to allow silver dissolution, and surface fluctuation lifetime increases with particle radius. The results presented in this chapter have been published in (*96*)

Chapter 3 Liquid Metal Dealloying: A New Concept in Porosity Evolution

3.1 Summary

Dealloying is typically considered an electrochemical process, but corrosion can occur in a variety of liquid environments, including liquid metals and molten salts. Liquid metal embrittlement is relevant for a variety of applications, such as galzanized coatings, solders, brazes, and weld-metals (*97–100*), but the concept of using this process for porosity evolution has never garnered interest or been extensively studied. In this chapter we challenge the notion that dealloying is restricted to electrochemical systems, and extend liquid metal corrosion to the fabrication of porous structures.

3.2 Background

3.2.1 Liquid Metal Dealloying

Liquid metal embrittlement is generally concerned with grain boundary weakening, and the accepted mechanism is that the liquid metal forms an intermetallic compound with the

parent metal at the grain boundary, destroying the internal interface and lowering the energy of the system (*97–100*). This field of study focuses on corrosion along grain boundaries and not within the grains themselves, and only considers alloy systems where the concentration of the dissolving component is very low. The idea of using a liquid metal to selectively dissolve a binary alloy (where the concentration of the dissolving component is higher) was introduced by Harrison & Wagner in 1959 when they dissolved noble metal alloys such as Cu-Au and Cu-Ni in metal baths of Bi and Ag, respectively (*39*). They observed a rough interface and the formation of a porous structure but this idea did not catch on as a fabrication method – presumably because the ligaments of the porous structure were hundreds of microns. As a result the idea remained untouched until 2011 when Kato and coworkers fabricated porous Ti using liquid Mg as a dealloying medium. As mentioned in Chapter 1, it is very challenging to fabricate porous materials out of elements with low standard reduction potentials such as Ti; there are very few alloying components that have a substantially lower reduction potentials and elements in this reduction potential range are prone to oxidation, inhibiting porosity evolution.

Another drawback to electrochemical dealloying mentioned in Chapter 1 is that the surface diffusivity of the remaining component cannot be too fast or too slow. To illustrate this point, a primary goal of this dissertation was to fabricate porous Ta by electrochemically dealloying V-Ta precursors (Figure 3.1). This alloy system met the first three requirements listed in section 1.4, however (in the opposite case of Chapter 2**)** the surface diffusivity of Ta was too low for porosity to evolve. A recent publication by Chen & Sieradzki provided a framework for porosity evolution as a function of the homologous temperature (reaction temperature normalized by the element's melting point), demonstrating that Pt is the highest

melting point element that can be fabricated at room temperature using electrochemical dealloying (*101*). Unfortunately, this work was not published until three years after this electrochemical dealloying experiment and there was no literature value for the surface diffusivity of Ta in electrolyte solutions. As a result, we did not fully understand the challenges of electrochemically dealloying V-Ta alloys and why porosity evolution did not occur.

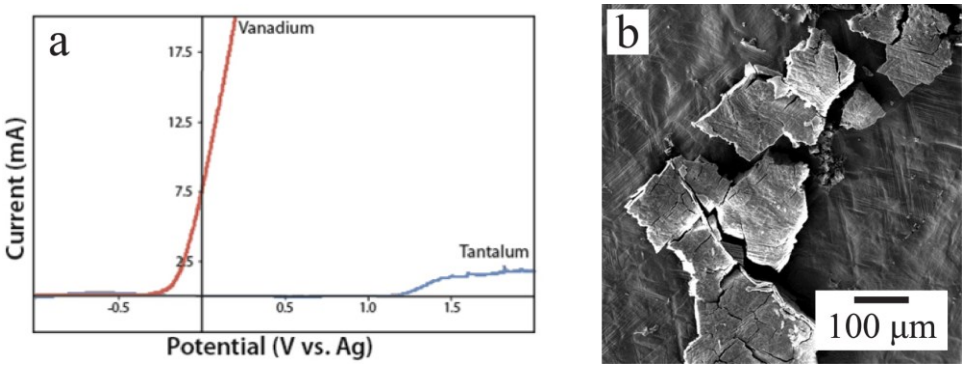

Figure 3.1. Failure of dealloying V-Ta. This systems meets the first three requirements of laid out in section 1.4: (a) Ta and V have a large distance between their onset potentials (greater than $1V$), is a solid solution, and we should expect to see dealloying over a similar composition range as the Ag-Au system. (b) The fault of this system is that the surface diffusion rate is too slow and the alloy falls apart when V is dissolved. The dark region is undealloyed Ta-V, and the white region is cracked Ta.

Liquid metal dealloying (LMD) overcomes this surface diffusivity challenge because the homologous temperature is much higher – metals are liquid at temperatures hundreds of degrees higher than electrolyte solutions – which enables porosity evolution. Instead of a critical potential, LMD uses enthalpies of mixing to control dissolution (*41*, *42*). Specifically, the liquid metal is chosen to have a negative enthalpy of mixing with the dissolving component(s) and a positive enthalpy of mixing with the remaining component(s). A schematic of LMD can be seen in Figure 3.2. Kato & Wada have since published several manuscripts

describing different LMD systems, focusing on dealloying in molten Mg to produce porous Fe, Cr, Nb, and Si.

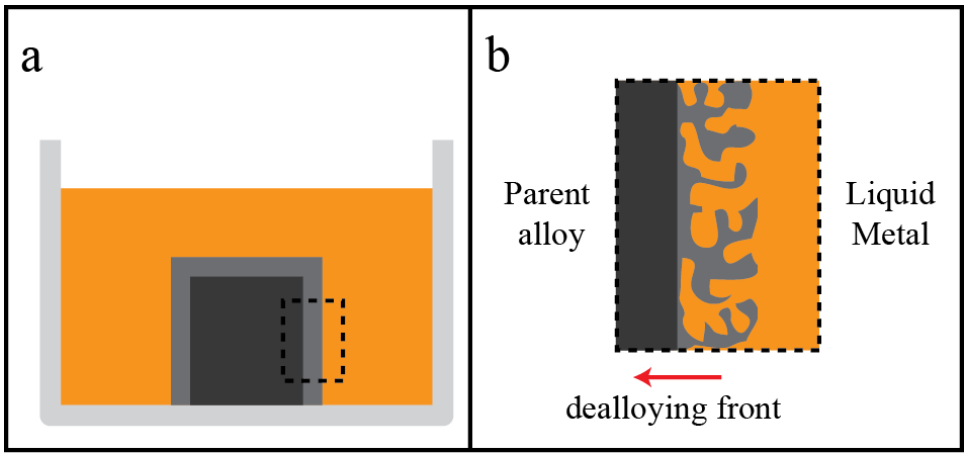

Figure 3.2. Schematic of liquid metal dealloying. (a) Parent alloy (dark gray) is immersed into a liquid metal bath (orange). (b) Zoom-in of the dashed region in (a) showing the dealloyed region (light gray) and the direction of the dealloying front (into the parent alloy).

3.2.2 The Ti-Refractory Element System

The remainder of the chapters in this thesis are centered on Ti-X alloys. Using Kato's work as inspiration we developed a unique liquid metal dealloying system by immersing Ti-rich refractory alloys into liquid Cu. Parent alloys of Ti-X, where X is a refractory element/alloy (e.g., W, Re, Os, Mo, Nb, V), are immersed in a bath of molten Cu. Cu has high Ti solubility but is immiscible with X. This concept is easily understood by examining a collage of Ti-Ta-Cu binary phase diagrams, Figure 3.3. Molten Cu dissolves Ti out of the alloy while allowing the refractory component to diffuse along the metal/liquid interface and reorganize into a porous network. Copper remains in the pores and fills the dealloyed phase volume as it penetrates into the parent alloy. The dissolved Ti diffuses out of the sample into the much larger Cu bath, which acts as a reservoir, effectively diluting it within the composite. After the dealloying process is completed, a dense bicontinuous composite with a characteristic ligament

diameter λ is formed upon cooling. A nanoporous structure can be excavated by electrochemically dissolving the Cu phase, and the low surface mobility of Ta at room temperature in an electrolyte prevents the material from coarsening while sitting in solution. Referring back to the idea of the homologous temperature, the ligament size can be tuned by altering the temperature of the bath. Generally, micron-sized ligaments are formed in Cu melts, but we can fabricate smaller ligaments by adding constituents to the bath, lowering its melting point. Specifically, by adding Ag and Bi to molten Cu we can fabricate molten baths with lower melting points across the range 400-1000 ^{o}C.

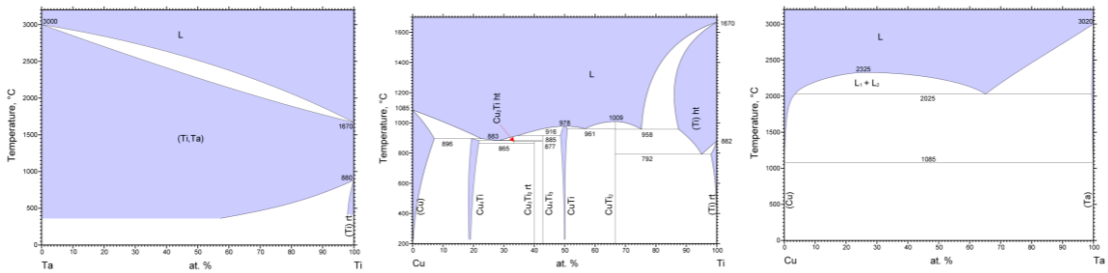

Figure 3.3 Relevant phase diagrams to understand liquid metal dealloying to make np-Ta. (left) Ti/Ta; this system forms a homogeneous solid solution over its entire composition range. (center) Ti/Cu; during LMD, Ti is dissolved from the Ti/Ta ingot and dissolved (up to 70 at. %) in molten Cu alloys. (right) Ta/Cu; during LMD, the remaining Ta does not dissolve in Cu, even molten copper, and reorganizes itself into a porous network via interface diffusion between itself and the melt.

Our dealloying strategy is general to all the refractory elements, but this chapter focuses on Ti-Ta and Ti-W alloys. It should be clarified that the bicontinuous structure is the result of a pattern forming instability during dealloying (identical to electrochemical dealloying) and all of the parent Ti-X alloys are homogenous, solid solution BCC alloys across the composition range at all processing temperatures.

3.3 Experimental Methods

$Ti_{65}Ta_{35}$, $Ti_{75}Ta_{25}$, $Ti_{85}Ta_{15}$, and $Ti_{75}W_{25}$ (99.9 wt.% Ti, 99.9 wt.% Ta, and 99.9 wt.% W) alloy buttons were prepared via arc melting Ti, Ta, and W powders by the Materials Preparation Center at Ames Laboratory, which is supported by the US DOE, Basic Energy Sciences. A ~30g $Ti_{95}Ta_5$ alloy was prepared in-house by radio-frequency (RF) induction using an Ambrel Ekoheat 45 kW system by melting Ti (99.995 wt.%), and Ta (99.95 wt.%) pellets from Kurt Lesker in a water-cooled copper crucible from Arcast Inc. under flowing Ar (99.999 wt.%). 1 cm^3 (~9 g) ingots were cut using wire electrical discharge machining (EDM), and then annealed via induction melting in an ultra-high vacuum (10^{-8} torr) environment at ~ 1500 ^oC for 72 hours in a ultra-high purity alumina crucible cast in-house using materials from Cotronics Corp. These ingots were then rolled into a foil 150 micrometers thick and 1-cm×1-cm foils were cut from this master foil. The smaller foil was then annealed in a cast alumina crucible for 8 hours via induction melting in an ultra-high vacuum (10^{-8} torr) environment at ~ 1500 ^oC.

Separately, the liquid metal bath (consisting of some ratio of Cu, Ag, and Bi, all 99.99% purity) was pre-melted in a graphite crucible using radio-frequency induction heating under flowing Ar gas and solidified to form a 5-10 g ingot. The annealed Ti-X foil was then placed in a different cast alumina crucible, the Cu/Ag/Bi ingot was placed on top of the foil, and the crucible was heated slowly using radio-frequency induction heating under flowing 5% H_2-95%Ar gas until the copper melted (see Figure 3.2 for reference to this experiment). The melt was maintained at the same power to keep the temperature constant, and power was applied for a fixed time (anywhere between 1 and 60 minutes). After this time the power was turned off and the system was allowed to cool to room temperature.

Dealloyed samples were examined using a JEOL scanning electron microscope (SEM) and energy-dispersive X-ray spectroscopy (EDS) was used to determine the composition of each phase. We examined both the composites formed after dealloying and the underlying porous refractory by chemically dissolving the Cu/Ag/Bi phase. The porous metals were smooth and easy to image, however the composites needed to be polished for imaging. Composite samples were mounted in Struers PolyFast conductive epoxy, and underwent: grinding steps of 400 grit, 600 grit; diamond polishing steps of 9 µm, 3 µm, 1 µm; and a final polishing step.

3.4 Results and Discusison

3.4.1 Proof of Concept

To test the idea laid out in section 3.2.2 we immersed a Ti-Ta sample into molten Cu for ~5 minutes and examined the dealloyed material. Figure 3.4.a shows the resulting Ta/Cu composite, where the light region is Ta and the dark region is Cu. In order to excavate the porous structure we immersed the sample in dilute nitric acid to dissolve out the Cu phase, Figure 3.4b. We performed an EDS map (Figure 3.4c,d), which confirmed our initial hypothesis that the Ta and Cu phases will not mix; there was, however, residual Ti in the Cu phase which will be addressed in Chapter 4. The structures created using molten Cu have large features, with ligaments on the order of 1 μm . We will address ligament refinement below.

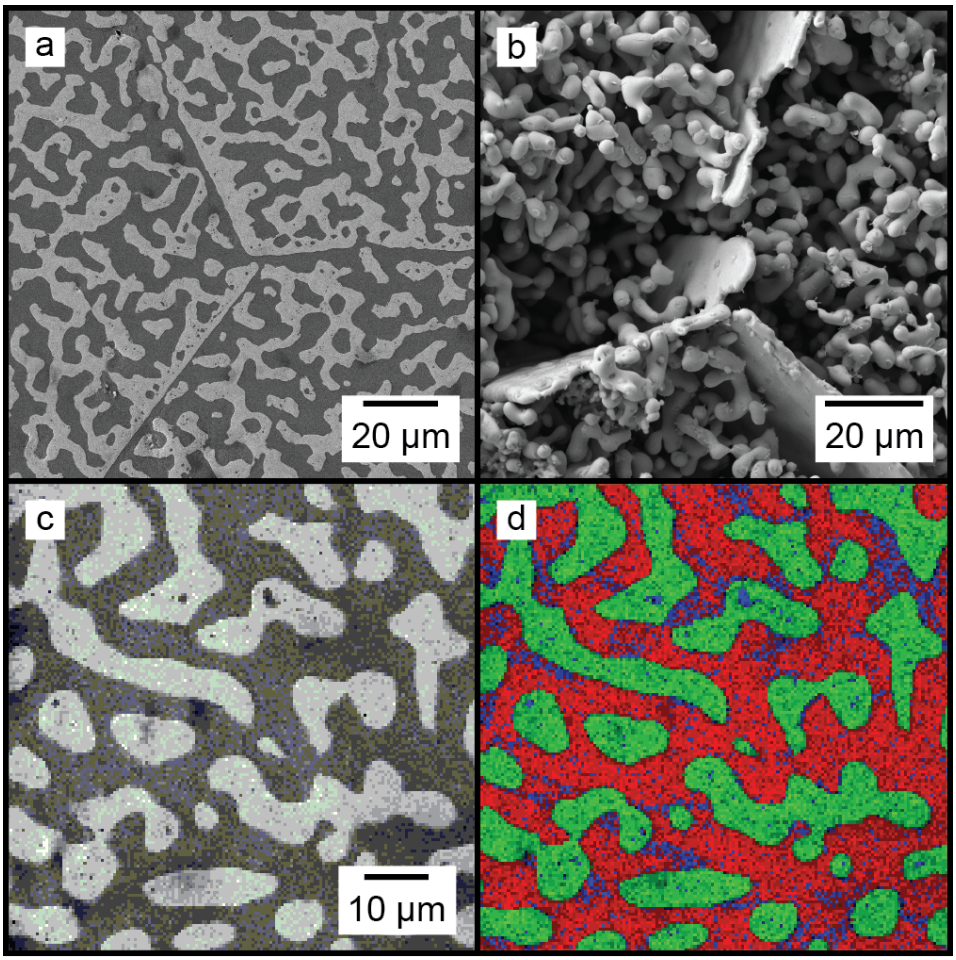

Figure 3.4 Bulk composites made by liquid metal dealloying. (a) Scanning electron microscopy (SEM) micrograph of a polished a Ta-Cu composite, showing a grain boundary triple junction. (b) SEM micrograph of a Ta-Cu composite with the Cu matrix phase dissolved away to reveal the nanoporous refractory dealloyed phase and a Ta-rich grain boundary. (c) SEM micrograph of a polished Ta-Cu composite for elemental mapping, with an ~5 μm ligament size. (d) Elemental mapping overlay of (c): Green is Ta, red is Cu, and blue is residual Ti in the Cu-rich matrix phase.

3.4.2 Temperature Effects

As mentioned in section 3.2.2, lowering the homologous temperature, and thus the surface diffusivity of the remaining component, will refine the ligament size in these materials; surface diffusivity has an Arrhenius dependence and will be suppressed at lower temperatures. This can be done by fabricating a lower melting point bath or altering the melting point of the

remaining component. To test this idea we immersed Ti-Ta samples into baths of $Cu_{32}Ag_{68}$ ($T_m \approx 780\,^{\circ}C$) and and $Cu_{20}Ag_{40}Bi_{40}$ ($T_m \approx 600\,^{\circ}C$), Figure 3.5. It was difficult to image the nanocomposite of these materials, e.g. Ta/ $Cu_{32}Ag_{68}$, so we chemically dissolved the Cu/Ag/Bi phase and imaged the nanoporous Ta, measuring approximate ligament sizes of 100 and 30 nm, respectively.

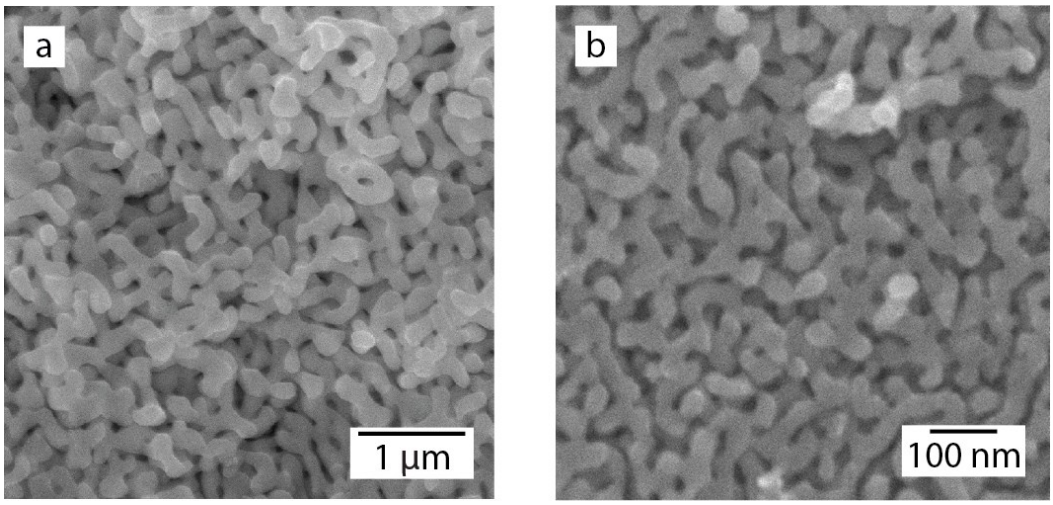

Figure 3.5 Dependence of ligament size on temperature in Porous Ta. (a) SEM micrograph of porous Ta with ~100 nm ligaments, dealloyed in $Cu_{32}Ag_{68}$ ($T_m \approx 780\,^{\circ}C$). (b) SEM micrograph of porous Ta with ~50 nm ligaments, dealloyed in $Cu_{20}Ag_{40}Bi_{40}$ ($T_m \approx 600\,^{\circ}C$).

We can also choose an element that has a higher melting point than Ta such as W. To test this idea we immersed Ti-W samples in molten Cu. W oxidizes in solution so the material was imaged as a composite and it can be seen that the ligament size is approximately 100 nm. Additionally, the Ti-W parent alloy only had 25 at.% W and as a result the composite has a much higher ratio of the Cu phase, which can alter the mechanical properties of the material. This will be addressed in Chapter 5.

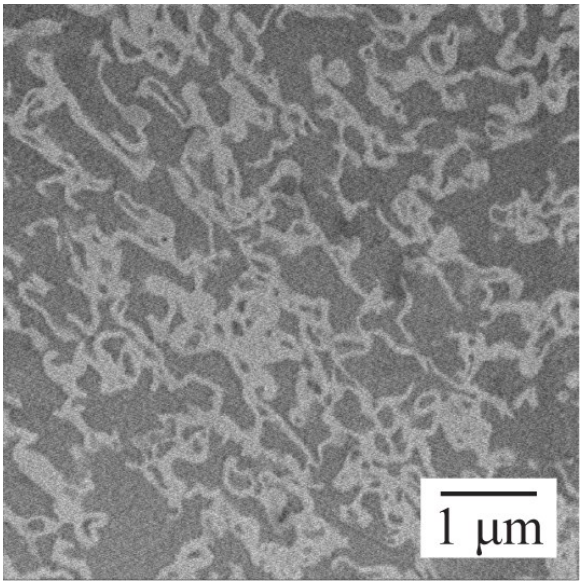

Figure 3.6 W-Cu nanocomposite fabricated by immersing Ti-W alloy in molten Cu. Due to its higher melting point, W rearranges into a porous structure with ~100 nm ligaments, compared to the 1 μm ligaments in Ta alloys dealloyed in molten Cu.

3.4.3 Morphology of the Dealloyed Structure

The bicontinuous structure is the result of concurrent dissolution and surface smoothening events, and considered a characteristic of nanoporous metals made via dealloying. For electrochemical dealloying the morphology is ubiquitous and there is no composition effect on the morphology. Dealloying $Ag_{60}Au_{40}$ or $Ag_{75}Au_{35}$ alloys yield the same porous Au structure, with minor differences in the ligament composition and the ligament:pore ratio. This is not the case for liquid metal dealloying and we observe dramatically different structures in Ti-Ta alloys dealloyed in Cu. It can be seen in Figure 3.7 that the morphology evolves from droplets (5 at.% Ta) into a connected bicontinuous structure (35 at.% Ta) as the Ta concentration increases.

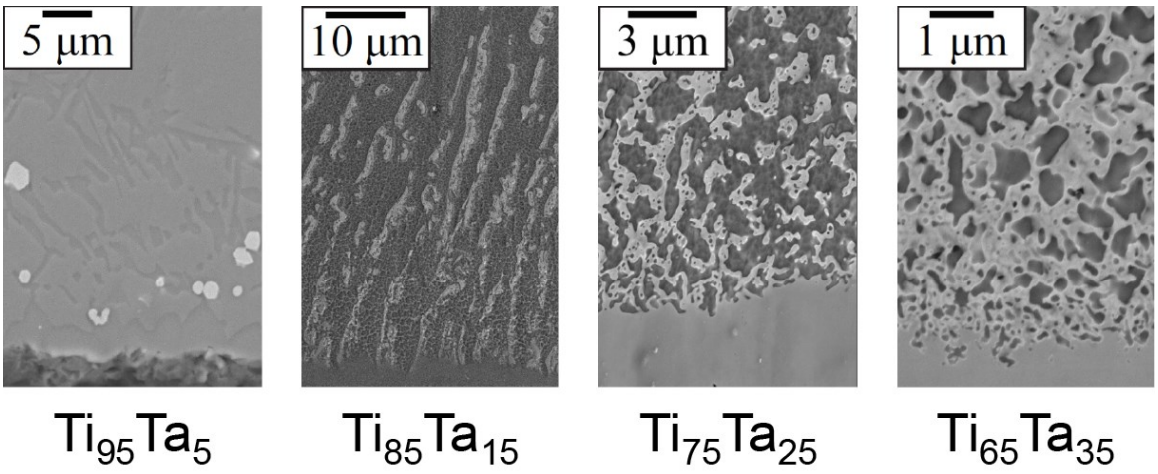

Figure 3.7 Morphology of TiTa samples at the dealloying interface (bottom of the images) at four different compositions. It is apparent that the structure becomes more connected as the Ta content increases.

We will only discuss this idea conceptually, but the kinetics of growth in LMD are governed by a competition of diffusion-coupled growth and interfacial spinodal decomposition. In electrochemical dealloying the initiation of porosity evolution is controlled by interfacial spinodal decomposition, but it is unclear how dealloying proceeds into the bulk of the material– owing to the short experimental time scales and difficulty in modeling the electrolyte solution. In contrast, liquid metal dealloying is easily captured using phase field modeling, which is a technique known for effectively modeling the solid/liquid metal interface. Using phase field modeling, it was recently shown that spinodal decomposition only occurs at the beginning of liquid metal dealloying (*102*). After the initial surface destabilization, bulk dealloying occurs by a diffusion-coupled growth mechanism (note that the Ta ligaments in the 15 at.% Ta sample looks very similar to eutectic lamellae). Similar to eutectic growth, lateral diffusion of Ta controls the growth at the dealloying interface; depending on the alloy composition, Ta at the interface is either able to maintain diffusion-coupled growth (such as in

25 and 35 at.% Ta), or the dealloyed structure detaches (5 and 15 at.% Ta) and new Ta-rich regions need to be reformed by interfacial spinodal decomposition. It might be thought that the interface velocity plays a role in the morphology, however dealloyed structures are self-similar and we have not seen the morphology at the interface change in experiments ($10^0 - 10^2$ seconds) or phase field modeling ($10^{-9} - 10^{-6}$ seconds).

This variety of morphologies has not been observed in electrochemical dealloying presumably because the dissolved species rapidly diffuses away into the electrolyte and does not remain near the surface of the porous structure. We have conducted preliminary LMD experiments which show that the concentration of the dissolved species in the liquid phase plays a role in the dealloying rate – increasing the concentration of the dissolved species lowers the driving force – and also the dealloyed morphology that forms – increasing the dissolved species results in a more connected structure although the mechanism is unclear. A detailed study of the kinetics of LMD will be addressed in Chapter 4**.**

3.5 Conclusions

In this chapter we demonstrated that liquid metal dealloying can be used to fabricate new porous materials that were unable to be fabricated using electrochemical techniques. Using Kato's work as inspiration, we developed a unique LMD system by immersing Ti-rich refractory alloys into molten Cu/Ag/Bi baths. During this immersion, Ti is selectively dissolved while the refractory element rearranges at the interface according to interfacial spinodal decomposition. This is identical to electrochemical dealloying, however, new morphologies in the dealloyed structure emerges due to the appearance of diffusion-coupled growth. Depending on the concentration of the remaining refractory component the resulting

structure can take the form of droplets, lamellae, or a connected porous network. In addition to tuning the morphology of the resulting structure the ligament size can be altered by changing the homologous temperature. The homologous temperature is a function of the reaction temperature, i.e. the bath temperature, and the melting point of the remaining component. The work laid out in this chapter has been included in a patent application and recently submitted work (*102*).

Chapter 4 Kinetics of Liquid Metal Dealloying

4.1 Summary

In this chapter we conduct an in-depth study of the kinetics and fundamental microstructure evolution mechanisms during liquid metal dealloying (LMD) using Ti-Ta alloys immersed in molten Cu as a model system. LMD has recently emerged as a novel technique to fabricate bulk nanostructures using a bottom-up self-organization process, however the literature lacks fundamental studies of this kinetic process. We developed a model that describes LMD after examining the effects of key parameters in our system by varying the alloy composition, dealloying duration, and dealloying temperature. Liquid metal dealloying has been analogized to electrochemical dealloying, however this work demonstrates several key differences. In particular, the rate-limiting step in electrochemical dealloying is the dissolution of a terrace atom whereas the rate-limiting step in LMD is diffusion of the dissolving component away from the dealloying interface.

4.2 Background

Liquid metal dealloying has recently been used to fabricate bulk nanoporous and nanocomposite materials for a variety of applications including electrochemical capacitors, Li-ion battery anodes, and high-strength structural materials (*4*, *7*, *40*, *45*, *103*). A majority of the work on this subject has focused on the characterization and properties of nanomaterials made by LMD. However, a recent phase field model has addressed some fundamental mechanisms of formation and the variety of morphologies that can be produced during LMD, which was briefly addressed in Chapter 3 [PA/Alain]. The purpose of this chapter is to experimentally investigate the kinetic parameters which affect dealloying, with an eye towards optimizing the fabrication of nanocomposite and nanoporous materials. For this study we chose our model LMD system of Ti-Ta alloys immersed in molten Cu. As demonstrated in the previous chapter, the Ti-Ta system is not limited to dealloying in molten Cu, and later in this chapter we briefly examine LMD of TiTa alloys in molten baths containing Cu, Ag, and Bi.

4.3 Experimental Methods

Experiments were carried out by immersing Ti-Ta alloy samples into Cu baths; we varied the alloy composition, immersion time and reaction temperature to investigate how these parameters affected the dealloying depth, ligament size, and concentration profile in the liquid phase.

Ti-Ta alloys were prepared in-house by radio-frequency (RF) induction using an Ambrel Ekoheat 45 kW system by melting Ti (99.995 wt.%), and Ta (99.95 wt.%) pellets from Kurt Lesker in a water-cooled copper crucible from Arcast Inc. under flowing Ar (99.999 wt.%). After casting the ingots were annealed under flowing Ar (99.999 wt.%) for a minimum of 10

hours and checked for homogeneity using energy-dispersive X-ray spectroscopy (EDS). Master ingots of ~30 g were made of the following compositions: $Ti_{70}Ta_{30}$, $Ti_{65}Ta_{35}$, $Ti_{55}Ta_{45}$, $Ti_{40}Ta_{60}$, $Ti_{30}Ta_{70}$, $Ti_{20}Ta_{80}$. Approximately 1g samples (roughly 6x2x10 mm) were cut for LMD from the master ingots using wire electrical discharge machining (wire EDM). After cutting, Ta wires were spot-welded onto one end of the sample for the immersion experiments and samples were lightly sanded with 600 grit to remove the recast layer from wire EDM.

Prior to immersion, a 40 g molten Cu (99.99 wt.%) bath was prepared in a high-purity alumina crucible cast in-house with materials from Cotronics at a preset temperature (1160, 1240, 1305, or 1360 ^{o}C). Temperature measurements were made using a Ircon Modline 5 infrared camera with a Yokogawa controller set to the emissivity of molten Cu. Prior to immersion, the sample was brought inside the RF coils –without touching the bath – and heated to avoid thermal gradients between the sample and the bath. The sample was then immersed into molten Cu for a fixed time (between 10 and 120 seconds) and then removed from the bath, halting the dealloying process.

Cross sections of the nanocomposites were prepared using wire EDM. The cross sections were mounted in Struers PolyFast conductive epoxy, and underwent: grinding steps of 400 grit, 600 grit; diamond polishing steps with grits of 9 µm, 3 µm, 1 µm; and a final polishing step of 0.05 µm. Composites were characterized using a JEOL scanning electron microscope (SEM) and ImageJ was used to measure dealloying depth and average ligament sizes. EDS was used to determine the composition of each phase as a function of depth. The dealloying depth was determined by averaging ~40 measurements taken from four images, which were from different regions of the sample. The average ligament size was determined by averaging

over ~20 measurements for a given depth. The composition for a given depth was determined by averaging over an area with a 1-5 μm diameter.

4.4 Results and Discussion

4.4.1 Dealloying Depth Data

Figure 4.1 shows raw data for dealloying depth as a function of time for three different compositions and four different temperatures. Error bars are not included, but all depth measurements had an error below 30 μm and the majority had an error below 15 μm. Three obvious trends are apparent: the dealloying depth increases with time, the dealloying depth increases with temperature (at fixed time), and the dealloying depth decreases with increasing Ta composition. The data also appears to have a power-law relationship with time. Below, we introduce a dissolution model to interpret our data and understand the dealloying depth's functional dependence on time and temperature. Figure 4.2 shows a panel of SEM images with typical cross sections (here, of $Ti_{55}Ta_{45}$ dealloyed for 20 seconds at four different temperatures), illustrating our measurements of dealloying depth.

4.4.2 Dissolution Model

We treat the LMD process as a 1-D Stefan problem, the general class of free boundary problems where a phase boundary can move with time (*104*). The original Stefan problem described the temperature distribution in the liquid phase during the solidification/melting of ice, which is analogous to the Ti concentration profile in the liquid phase during LMD.

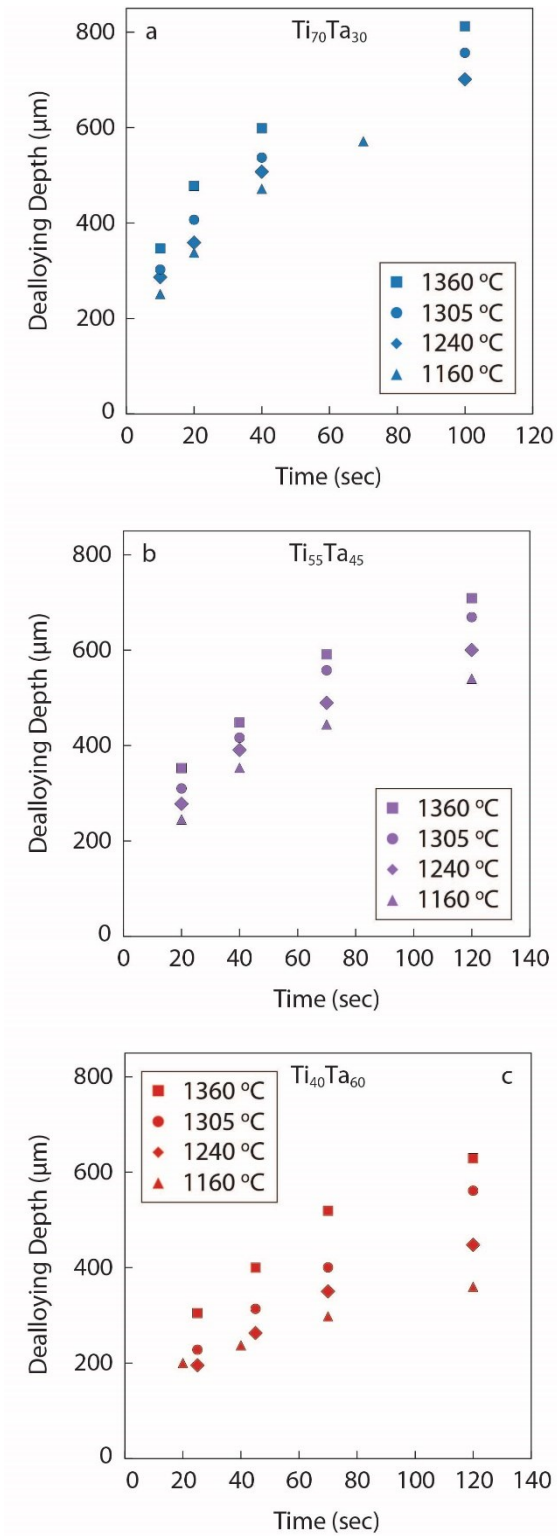

Figure 4.1 Dealloying depth versus time for the samples in this study. We studied four temperatures: triangle (1160 °C), diamond (1240 °C), circle (1305 °C), and square (1360 °C); four times (10-120 seconds); and three compositions: (a) $Ti_{70}Ta_{30}$ (blue), (b) $Ti_{55}Ta_{45}$ (purple), and (c) $Ti_{40}Ta_{60}$ (red).

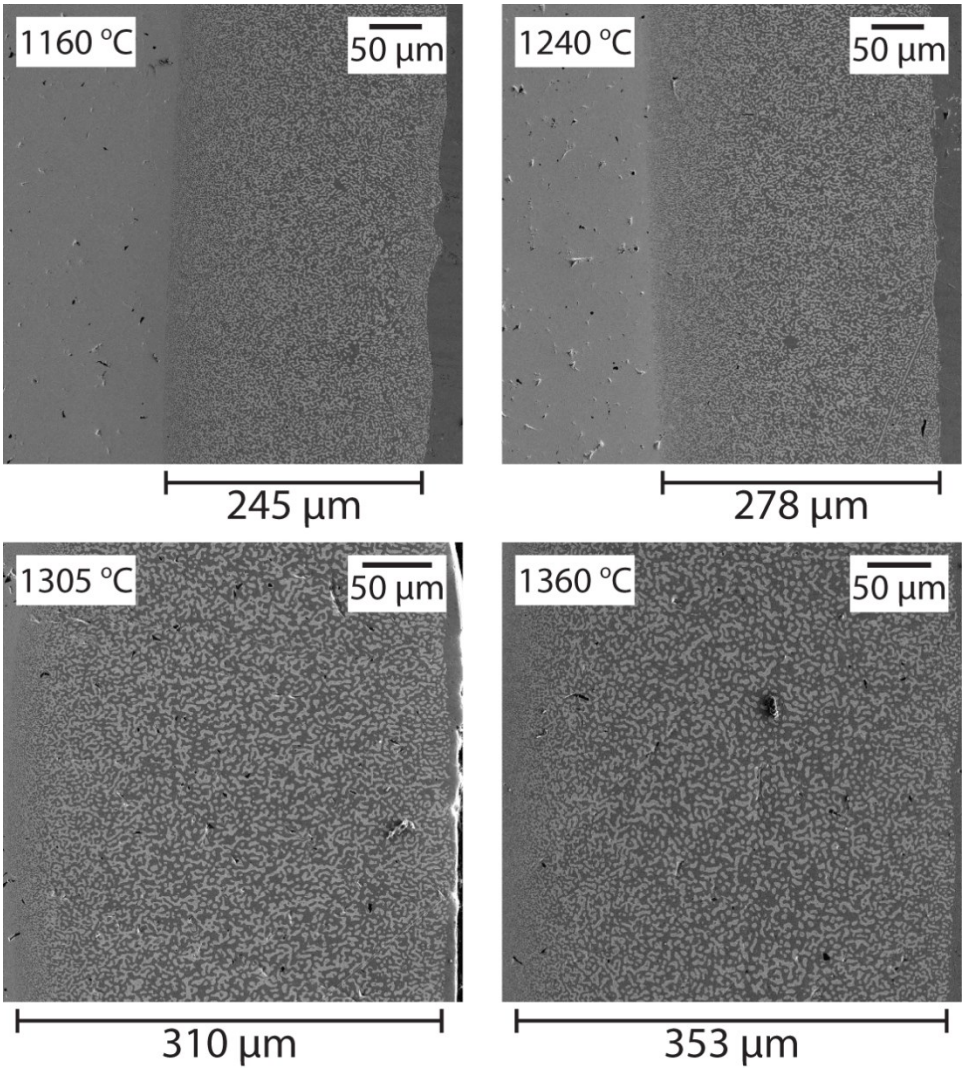

Figure 4.2 Scanning electron microscopy (SEM) micrographs of $Ti_{55}Ta_{45}$ samples dealloyed in molten Cu for 20 seconds at four temperatures. The dealloying interface is sharp and flat, and the dealloyed region has a natural contrast due to the different compositions; the dark phase is Cu and the light phase is Ta. The top two images were taken at 200x magnification and the bottom two were taken at 270x magnification, but it can be seen that dealloying depth increases with increasing time.

The PDE describing the Ti concentration distribution is discontinuous across the solid-liquid phase boundary, but the Stefan condition allows for a solution by expressing the velocity of the boundary as a function of the flux across the interface. This construction allows us to solve for the position of the dealloying interface and the concentration profile in the liquid within the dealloyed region as functions of time, which are central to understanding how to fabricate nanomaterials using this process.

Figure 4.3 illustrates LMD as a one-dimensional Stefan problem. Consider an isothermal system containing an infinite liquid bath of Cu and a semi-infinite block of Ti-Ta where $s(t)$ is the position of the interface between the two phases. When $t > 0$, the Cu phase dissolves Ti from the TiTa alloy, moving the interface into the solid. As the interface moves, the liquid phase collects the dissolved Ti, and the rate-limiting process is Ti diffusion away from the interface. If the rate-limiting process was Ti dissolution from a terrace site – as is the case in electrochemical dealloying – we would not expect to see a buildup of Ti inside the dealloyed region, however we show below that Ti accumulates in the dealloyed region and leads to a decrease in the dealloying velocity with increasing time. It is also possible that bulk diffusion in the solid may play a role, where the rate-limiting step is Ti diffusion from the bulk to the interface, but this is unlikely. This mechanism typically produces dendritic voids, a morphology not reported in this work, and the interdiffusivity in Ti-Ta is too slow. To compare, at 1200 ºC $D^{S}_{Ti\rightleftarrows}$ $10^{-9}\ cm^2 s^{-1}$ and $D^{L}_{Ti\rightarrow Cu} \approx 10^{-5}\ cm^2 s^{-1}$ (*105*, *106*).

The concentration of Ti in the liquid phase, $c(x,t)$, follows the diffusion equation:

$$\frac{\partial c}{\partial t} = D_L \frac{\partial^2 c}{\partial x^2} \tag{4.1}$$

where D_L is the diffusivity of Ti in liquid Cu. The Stefan condition at the moving boundary, $x = s(t)$, is

$$\frac{ds}{dt}\left(c_S^{Ti} - c_L^{Ti}\right) = D_L \frac{\partial c}{\partial x}\left(s(t), t\right) \tag{4.2}$$

where c_S^{Ti} is the concentration of Ti in the solid at the interface, and c_L^{Ti} is the concentration of Ti in the liquid at the interface.

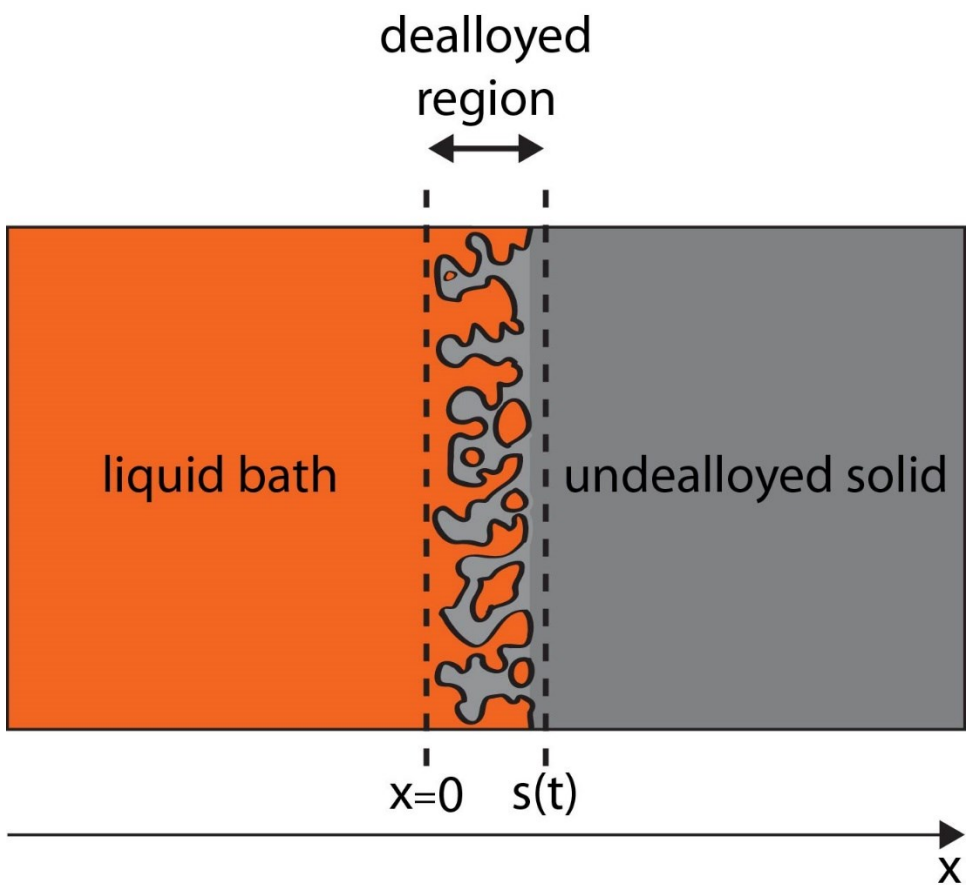

Figure 4.3. Illustration of liquid metal dealloying. The dealloyed region (dashed lines) is bounded on the left by molten Cu (orange) and on the right by undealloyed Ti-Ta (gray). The interface between the solid and the liquid Cu is initially at $x = 0$, and when $t > 0$ molten Cu dissolves Ti out of the solid, moving the interface, $s(t)$, towards the right ($s(t)_{t \to \infty^+} \to \infty^+$). The Ta atoms are left behind, reorganizing into a porous network.

An expression for the concentration profile is derived in Appendix B.1 and is given by Eq. (B.6), repeated here:

$$c(x,t) = \frac{c_L^{Ti} - c_{-\infty}^{Ti}}{erf(\lambda)} erf\left(\frac{x}{2\sqrt{D_L t}}\right) + c_{-\infty}^{Ti} \tag{4.3}$$

Here, $c_{-\infty}^{Ti}$ is the concentration in the Cu bath and λ can be fit experimentally or determined numerically from the analytical solution derived in Appendix B.2, Eq. (B.10), repeated here:

$$\lambda\left(erf(\lambda)\right)e^{\lambda^2} = \frac{c_L^{Ti} - c_{-\infty}^{Ti}}{\sqrt{\pi}\left(c_S^{Ti} - c_L^{Ti}\right)}. \tag{4.4}$$

It is noted in Appendix B.1**,** but we would like to emphasize that Eq. (4.3) accounts for the effects of induction heating and the solution given by Eq. (B.4) should be used if the LMD experiment uses resistive heating. In the case of induction heating we assume that the edge of the sample will always have the same Ti concentration as the bulk liquid, i.e. $c(x=0,t) = c_{-\infty}^{Ti}$. We introduce this assumption because induction melting induces eddy currents, which add convection to system outside of the dealloyed region. The degree of convection could be backed out by immersing samples at different rotation rates, controlling the convection and measuring the concentration profile (this is similar to a rotating disc electrode setup in electrochemistry), but that is experimentally challenging and beyond the scope of this work. The inherent convection caused by induction melting creates a beneficial and serendipitous steep concentration gradient at the outer geometric surface of the sample; we predict an increase in the dealloying rate compared to dealloying in a typical resistive-heating furnace.

4.4.3 Concentration Profiles

In general, Eq. 3 fits our data well, with one caveat. As shown by example in Figure 4.4, our data deviates from our model near the original outer surface of our samples, where the raw data shows a relatively greater concentration of Ti. We believe this deviation is due to coarsening of the Ta-rich ligaments, and is analogous to post-dealloying coarsening in electrochemical dealloying where the ligaments enrich in the noble component (*9*, *107*). During coarsening, Ti inside the ligaments become exposed to the surface through Ta-mediated surface smoothening and genus-reduction events, and then dissolve into the liquid phase (*35*). This surface diffusion process has an approximate $t^{-1/4}$ dependence and has a minor effect on the dealloying velocity (section 3.4) (*35*, *37*). The Ta-rich ligaments can be considered finite point sources of Ti, and it can be seen in Figure 4.5 that Eq. (4.3) better fits the concentration profile at later times when the ligaments near the edge of the sample become depleted in Ti. Using Eq. (B.5), we performed a least squares fit on the experimental data for 1240 ^{o}C for each composition ($Ti_{70}Ta_{30}$, $Ti_{55}Ta_{45}$, and $Ti_{40}Ta_{60}$), and obtained values for the diffusivity (Table 4.1) very close to the literature value (*106*). The literature value is from a series of experiments by Shurygin & Shantarin where they measured Ti dissolution in molten Cu across the range 1100-1400 ^{o}C using a rotating Ti rod to overcome connective transfer and determine a true diffusion coefficient for Ti in molten Cu. We excluded the portion where the experimental curves deviate from the model due to ligament coarsening during the fit, however as shown in Figure 4.5 this region is quite small for the longer times and is not a significant source of error.

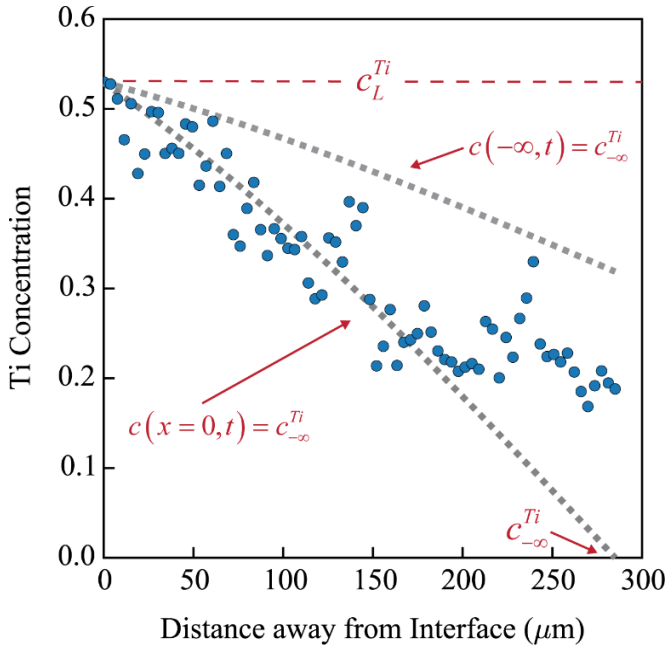

Figure 4.4. Comparison of Ti concentration in the Cu phase versus distance away from the dealloying interface between the experimental data (blue markers) and the analytical model (dashed lines) using the two different boundary conditions. The analytical model matches well if we assume the Ti concentration at the edge of the sample is always zero, which is the result of electromagnetic stirring caused by induction melting. The deviation between the model and the experimental data at distances far from the interface is due to ligament coarsening, which adds extra Ti to the Cu bath.

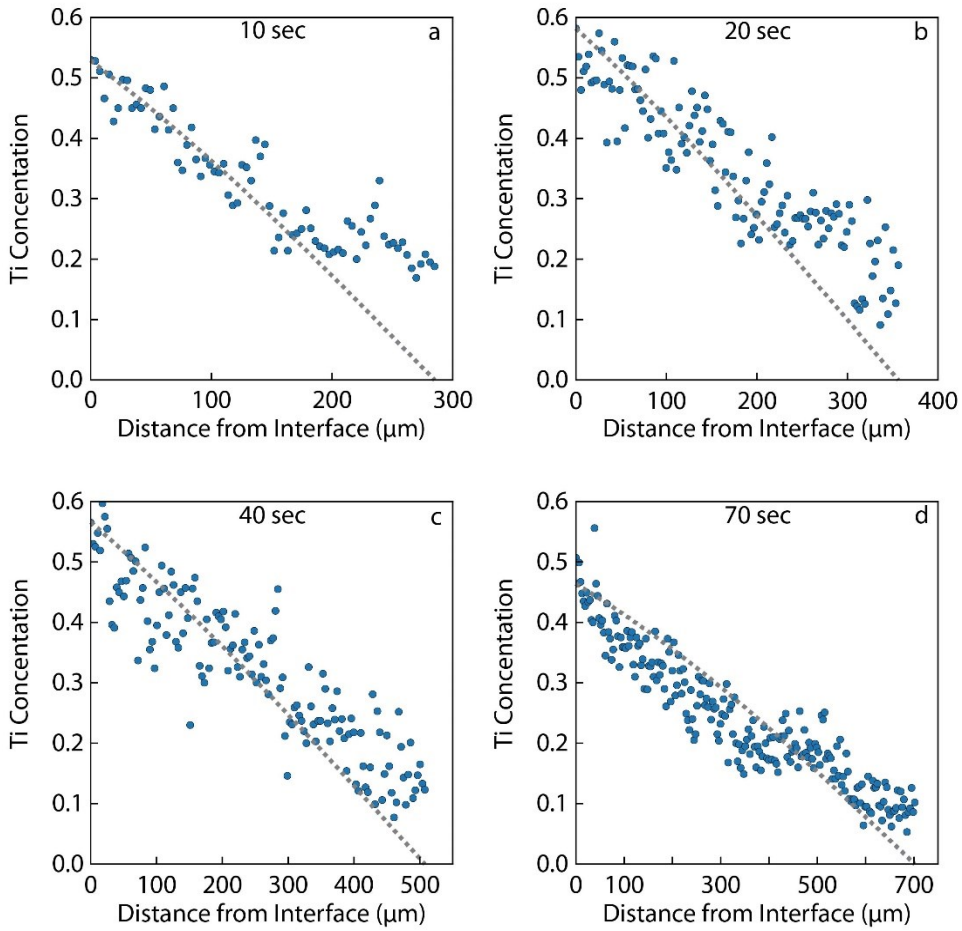

Figure 4.5. Ti Concentration versus distance away from the dealloying interface for $Ti_{70}Ta_{30}$ at 1240 °C. Experimental data (blue markers) compared with Eq. (B.5) at different times: (a) 10 seconds, (b) 20 seconds, (c) 40 seconds, and (d) 70 seconds. Eq. (B.5) was simultaneously fit across all times yielding $D_L(1240\,^{\circ}C)$ $6.5*10^{-5}\ cm^2 s^{-1}$, agreeing well with the literature value $D_{Ti\to Cu}(1240\,^{\circ}C)$ $7.0\times10^{-5}\ cm^2 s^{-1}$.

4.4.4 Dealloying Depth

An expression for the dealloying depth is derived in Appendix B.2, Eq. (B.11), repeated here:

$$s(t) = \sqrt{4\lambda^2 D_L t}\ . \tag{4.5}$$

We used Eq. (4.4) and the experimentally measured concentrations to determine λ for each composition, and backed-out the diffusivity and activation energy for each composition by collapsing the data from each temperature onto the curve $s(t) = \sqrt{4\lambda^2 t'}$, where $t' = t * D_L$, $D_L = D_0 \exp(-E_a / k_B T)$, E_a is the activation energy for Ti diffusion in molten Cu, and T is the temperature of the reaction. The values determined from this fit are listed in Table 4.1, and activation barriers for all compositions less than Ta_{60} agree well with literature values. However, the fit D_0 values differ by two orders of magnitude from the literature value. We suggest this discrepancy is due to the additional Ti added to the bath from ligament coarsening: i.e., extra Ti at the edge of the sample reduces the driving force for Ti diffusion away from the dealloying front, and a more rigorous form of Eq. (4.5) would include a second, albeit minor, term with a $t^{1/4}$ dependence to reflect this effect. It is also possible that the tortuosity of the dealloyed structure may interfere with Ti diffusion, increasing the diffusion path length from the dealloying interface to the edge of the sample. Thus, we hypothesize relaxing the form of Eq. (4.5) to

$$s(t) = \left(4\lambda^2 D_L t\right)^n \tag{4.6}$$

and allow the exponent n to be determined from the experimental fit. Figure 4.6 is a plot of the collapsed data versus t' and it can be seen that each data set has close groupings.

The values for the exponent were found to be close to $n = 0.5$, with $n_{Ti_{70}Ta_{30}} = 0.38$, $n_{Ti_{55}Ta_{45}} = 0.41$, and $n_{Ti_{40}Ta_{60}} = 0.45$. It is reasonable that the exponent for the $Ti_{70}Ta_{30}$ data set is lower than the $Ti_{55}Ta_{45}$ and $Ti_{40}Ta_{60}$ data sets because there will be more residual Ti in the Ta ligaments, which will lead to a larger effect from coarsening. Consistent with this idea, we see the exponent approach $n = 0.5$ as we increase the Ta concentration. The values of D_0 for all compositions using Eq. (6) to fit $s(t)$ are within an order of magnitude of the literature value and agree much better than the fit using Eq. (4.5). The activation energies for $Ti_{70}Ta_{30}$, $Ti_{55}Ta_{45}$ were found to be $0.67\ eV$ and $0.69\ eV$, respectively, which is very close to the literature value $E_{Ti \to Cu} = 0.715\ eV$. Interestingly, the value for $Ti_{40}Ta_{60}$, $E_a = 1.29\ eV$, was much higher than samples at lower Ta composition, suggesting a different mechanism became the rate limiting step. This could either be a switch to attachment/detachment-limited regime such as seen in electrochemical dealloying, or an effect of the morphology of the dealloyed structure, which will be addressed in section 3.6.2.

Table 4.1 Kinetic parameters determined for the compositions in this study.

Composition	D_L(1240 °C) $cm^2 s^{-1}$	λ	n	$D_0\ (cm^2 s^{-1})$	$E_a\ (eV)$
literature value	7.0×10^{-5}	-	0.5	1.7×10^{-2}	0.715
$Ti_{70}Ta_{30}$	6.5×10^{-5}	0.99	0.38	$4.6 \times 10^{-4,*}$ $3.4 \times 10^{-2,**}$	0.45^{*} 0.67^{**}
$Ti_{55}Ta_{45}$	3.3×10^{-5}	0.915	0.41	$8.2 \times 10^{-4,*}$ $6.5 \times 10^{-3,**}$	0.57^{*} 0.69^{**}
$Ti_{40}Ta_{60}$	4.8×10^{-5}	0.88	0.45	$4.8 \times 10^{-2,*}$ $1.2 \times 10^{-1,**}$	1.17^{*} 1.29^{**}

* indicates parameter fit using Eq. (4.5) **indicates parameter fit using Eq. (4.6)

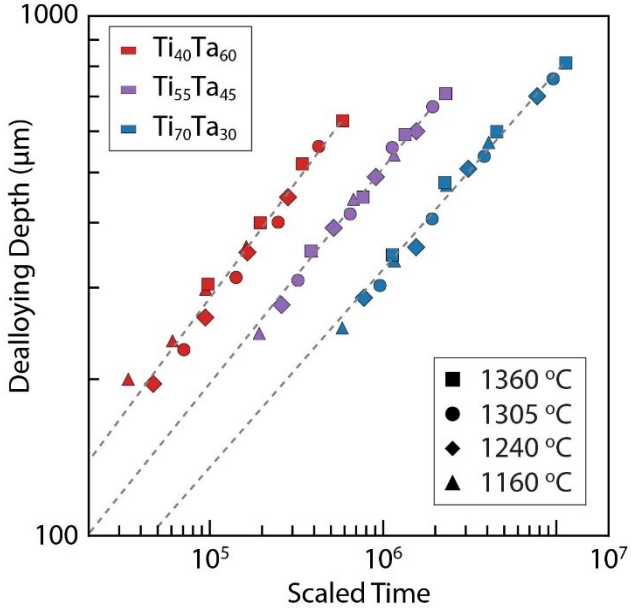

Figure 4.6 Collapsed dealloying depth versus scaled time $t' = t * D_0 * \exp\left(-E_a / k_B T\right)$ for $Ti_{40}Ta_{60}$ (red), $Ti_{55}Ta_{45}$ (purple), and $Ti_{70}Ta_{30}$ (blue). The symbol shape corresponds to the experimental temperature: triangle (1160 °C), diamond (1240 °C), circle (1305 °C), and square (1360 °C). Dashed lines: fits to the data using the relationship $s(t) = \left(4\lambda^2 D_L t\right)^n$. The values of λ, D_0, E_a, and n were determined for each data set and are listed in Table 4.1.

Our final comment on the dealloying depth is the effect of grain boundaries, which can significantly alter the kinetics. Figure 4.7 is a cross-section of a $Ti_{65}Ta_{35}$ sample (dealloying depth data not included in this work due to the ingot's small grain size) dealloyed at 1160 °C for 120 seconds. The dealloying interface is much rougher than the ones Figure 4.2, making it difficult to measure an accurate dealloying depth. We speculate that this is the result of different grains dealloying at different rates, but more importantly from grainboundaries themselves.

We observed grainboundaries are always dissolved first during LMD, replacing the solid-solid interface between adjacent grains with a solid-liquid-solid interface; at later times the

regions between grains fully detach and a thick Ta-rich region appears (Figure 4.7). It is not accurate to call these regions grain boundaries because the solid-solid interface is destroyed during dealloying, but we will use this name out of convenience. Dealloying is slower in regions where grainboundaries are perpendicular to the dealloying direction, and we think it is reasonable to conclude the boundaries impede Ti diffusing away from the dealloying interface. For this reason we made sure that all of the starting alloys in this study were sufficiently annealed, and most samples had an average grain size of ~500 um. We caution future work to be aware that boundaries can alter the kinetics, and it is desirable to have as large grains as possible to dealloy to large depths.

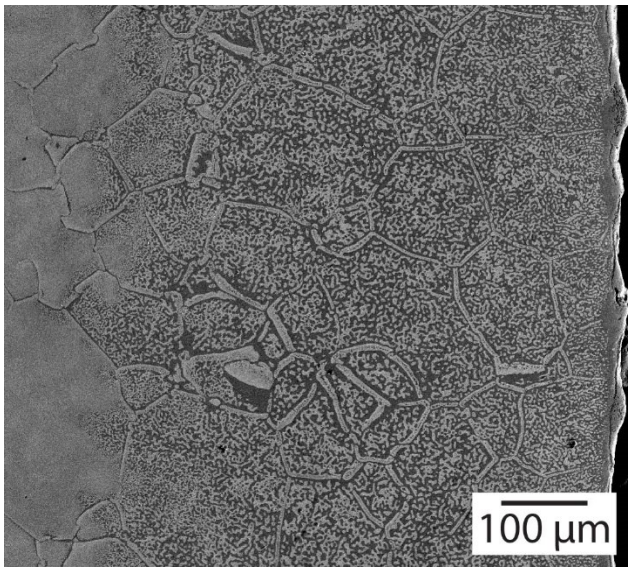

Figure 4.7. Effect of grain boundaries on dealloying kinetics. $Ti_{65}Ta_{35}$ (dealloyed depth data not included in this work) sample dealloyed at 1160 ºC for 120 seconds. The grains in this structure are small, causing an inhomogenous dealloying interface, contrasting with Figure 4.2. It can also been seen that the boundaries dissolve faster than the interior of the grains.

4.4.5 Parting Limit

We will briefly discuss the parting limit in liquid metal dealloying, which has been extensively studied in electrochemical dealloying (*18*, *23*, *108*). This concept was introduced in section 1.3.1, but it is worth reiterating that the parting limit, or percolation threshold p_c, is the critical alloy composition (defined in the percentage of the dissolving component) necessary for a structure to fully dealloy. For dealloying it is important to introduce the concept of high-density percolation, $p_c(m)$, which denotes that a percolation path exists composed of atoms [of the dissolving species] with at least m neighbors. We expect The Ti-Ta alloy system to have a higher percolation threshold than fcc dealloying systems such as Ag-Au because the bcc lattice has fewer nearest neighbors. This idea is corroborated by $p_c^{bcc}(1) \approx 24.5$, whereas $p_c^{fcc}(1) \approx 19$ at.%.

In this study we did not characterize a parting limit in detail; however, out data suggests it likely sits around 40 at.% Ti. We attempted to dealloy $Ti_{30}Ta_{70}$ and $Ti_{20}Ta_{80}$ samples but did not observe any significant dissolution. Samples from both alloys were immersed into molten Cu for several minutes, and we only saw small channels of Cu near the surface of the sample which were no wider than 500 nm and no longer than tens of microns. Previous work in electrochemical dealloying has demonstrated that surface dealloying can always occur due to low coordination at the surface, but this does not imply the sample will fully dealloy. Analogously, liquid metal embrittlement can occur in systems with no dissolving component such as Al embrittlement by Ga. We were able to dealloy $Ti_{40}Ta_{60}$, however the activation barrier for this composition was almost twice that of the activation barrier for $Ti_{55}Ta_{45}$ and $Ti_{70}Ta_{30}$; it is possible 40 at.% Ti is just above the percolation threshold. This low parting limit is surprising but other fcc dealloying systems such as Al-Cu and Zn-Cu have thresholds close

to ~20 at.%, the value for $p_c(1)$ (*109*). Our system could be a special case like Al/Zn-Cu, however a much older LMD study observed a similar percolation threshold, $30\,at.\% < p_c < 40\,at.\%$, in a familiar electrochemical dealloying system, Au-Cu, which has an electrochemical parting limit of 55 at.% (*39*). From a geometric standpoint the parting limit correlates to the size necessary for ion solvation; it is thus logical to speculate that as the effective size of an atom dissolving into a melt is smaller than a solvated metal ion dissolving into the solution, that the parting limit would be lower.

4.4.6 Ligament coarsening

We observed a significant amount ligament coarsening during LMD in molten Cu, with nm-sized features at the interface and μm-sized features at the edge of the sample. Figure 4.8a,b contrasts the ligament size in a $Ti_{40}Ta_{60}$ sample where the ligaments are ~80 nm at the interface and rapidly increase to ~ 1 μm at the edge of the sample. The morphology of the structures, see section 3.6.2, was composition dependent, but in general the lengthscale as it varied away from the interface was approximately the same regardless of the composition.

It was shown in previous work by Erlebacher that coarsening in nanoporous metals consists of two concurrent surface diffusion-mediated processes: surface smoothening and ligament pinch-off events (*35*). In an ideal case both have a $t^{1/4}$ dependence, but the mutual dependence of these two processes leads to a more complicated relationship for the surface evolution in nanoporous metals. Ligament pinch-off events decrease the genus of the material (the number of "handles"), however these events increase the local mass of a ligament, and future genus reduction events cannot occur until surface smoothening has redistributed this excess mass across the porous structure. It is therefore incorrect to say there is a simple relationship for

coarsening in porous metals. However, we are able to measure an activation energy associated with coarsening and use it here to comment on ligament coarsening during liquid metal dealloying.

Figure 4.8c shows the ligament size versus dealloyed depth for $Ti_{40}Ta_{60}$, dealloyed for 20 seconds at 1160, 1240, 1305, and 1360 ºC. Using Eq. (4.6) and our values listed in Table 4.1 we translate the ligament size to a function of time, included as Figure 4.8d. We only show the data for one composition, however the power-law exponents for all compositions (Figure 4.8d) were nearly identical and the associated activation energies were reasonably close: $Ti_{70}Ta_{30}$ ($E_a = 1.30\, eV$) , $Ti_{55}Ta_{45}$($E_a = 0.82\, eV$), and $Ti_{40}Ta_{60}$ ($E_a = 0.91\, eV$). It should be apparent from Figure 4.8c,d that there are two distinct ligament coarsening regions.

There appears to be a slight lag in the initial ligament size as a function of dealloying depth in Region I (Figure 4.8c), however this disappears when we convert to an estimated time (Figure 4.8d). It was shown in simulations that the ligament size will always lag a reduction in genus, however it is difficult to conclude this effect without estimating an average genus per volume (*35*). In Region I (Figure 4.8d) we observe a power-law exponent close to the ideal for coarsening ($n \approx 0.25$), and the average activation energy in this region was $E_A = 1.01\, eV$. This behavior is reasonable because at longer times, coarsening should be limited by mass transport across the surface and not genus reduction events. In Region II (Figure 4.8c,d), however, we barely notice any increase in the ligament size for a given temperature ($n \approx 0.03$), which we attribute to the structure approaching a genus of zero (over the scale of measurement). The ligaments at the edge of the samples have very low genus/volume values and can no longer increase their size through surface diffusion-mediated events. As a result the only way the average ligament size can increase is by two ligaments coming into contact and

fusing together. This appears to be a very slow process, and the ligament size does not increase significantly in Region II.

4.4.7 Morphology

In Chapter 3 we noted that the morphology of structures fabricated using liquid metal dealloying can be dramatically different depending on parent alloy composition. We observed a morphology transition from Ta droplets to a connected, porous Ta network as the parent alloy composition changed from $Ti_{95}Ta_5$ to $Ti_{65}Ta_{35}$. In this current study we are only examining connected structures, and report subtle changes in the morphology. Specifically we see an increase in the connectivity of the structures as we increase from 30-60 at.% Ta, which in turn affected the stability of the Ta network at longer times (Figure 4.9).

We observed good mechanical integrity when the Ta concentration was greater than ~30 at.%, owing to the connectivity in the porous network, which is a major reason why this work focuses on Ta-rich alloys. Samples with lower Ta concentrations were mechanically stable for short immersion times (less than 10 seconds), but fell apart during longer immersions (greater than 20 seconds). Only samples with at least 30 at.% Ta were robust enough to hold together during long immersion experiments (up to 120 seconds). Ligament pinch-off mediated coarsening decreases the connectivity of the porous structure with increasing time, and eventually ruins the mechanical integrity of the sample. Not only did the connectivity depend on time but also on the Ta composition. For comparison, Figure 4.9 shows the connectivity of the ligaments change at the edge of the sample from disconnected blobs in the $Ti_{70}Ta_{30}$ sample to a highly connected structure in the $Ti_{40}Ta_{60}$ sample. This effect is quite significant in Cu

baths, however it should be less obvious in lower-melting point baths where the ligaments do not coarsen significantly past their formation size.

It was mentioned in section 3.4 that the activation energy for Ti diffusion in molten Cu for the $Ti_{40}Ta_{60}$ composition was quite high, almost twice that for $Ti_{55}Ta_{45}$ and $Ti_{70}Ta_{30}$. It is possible that the high connectivity at the interface significantly limits the diffusion path for Ti atoms out of the dealloyed structure, and the limiting mechanism becomes a pinch-off event to allow the Ti atom to "escape" this highly tortuous region. This activation energy was very similar to the activation energy for coarsening in section 3.6.1, however it is very difficult to deconvolute pinch-off events from surface smoothening events.

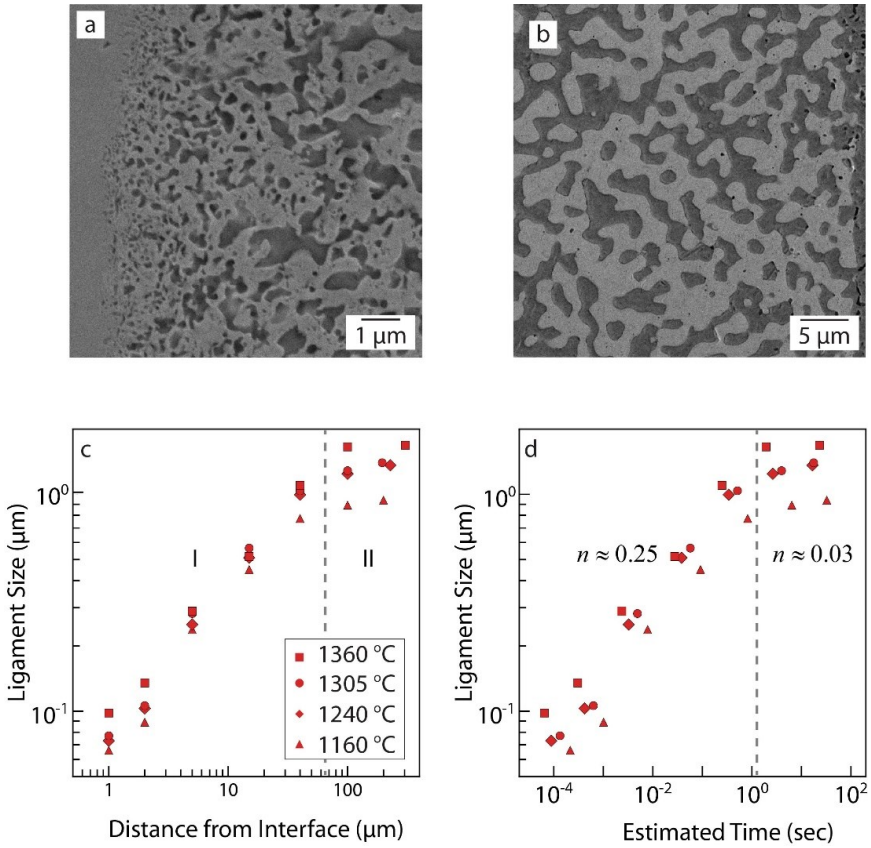

Figure 4.8. Ligament coarsening during LMD using $Ti_{40}Ta_{60}$ as an example. (a) SEM micrograph of the dealloying interface (bottom of the image) showing ligaments ~80 nm at the interface. (b) SEM micrograph of the edge of the sample (bottom of the image) showing ~1.5 µm ligaments at the edge of the sample. (c) Ligament size versus distance from interface. (d) Ligament size versus estimated time.

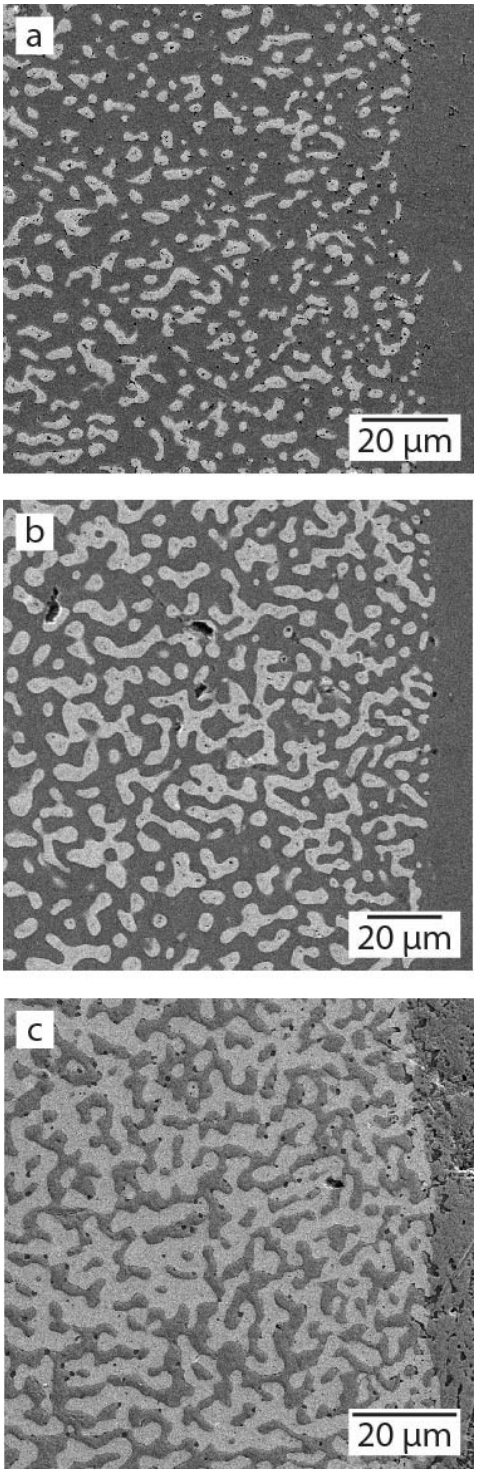

Figure 4.9. Difference in morphology at the edge of samples dealloyed for 20 seconds at 1305 °C as a function of alloy composition: (A) $Ti_{70}Ta_{30}$ showing mostly disconnected blobs, (B) $Ti_{55}Ta_{45}$ showing a mixture of disconnected blobs and connected ligaments, and (C) $Ti_{40}Ta_{60}$ showing a highly connected structure.

4.4.8 Homologous Temperature Effects

We demonstrated in Chapter 3 that by adding Ag and Bi to molten Cu we can fabricate molten baths with lower melting points and thus refine the ligament size of the porous structure. What we left out of that discussion was that each sample was dealloyed for a significant time, and the samples were only dealloyed to a depth of 150 μm .

The only drawback to making alloy baths is maintaining a high solubility of the dissolving component. Across this temperature range, Bi(ℓ) and Ag(ℓ) have at most 4 and 2 at.% Ti solubility, respectively, although it is unclear how Cu affects the solubility. Referring back to Eq. (B.10) and Eq. (4.6) the dealloying rate is highly dependent on the solubility in the liquid phase as well as the concentration in the liquid bath. As a result, the dealloying rate becomes very sensitive to the size of the bath, and large quantities are needed to dealloy thin samples. Future work will need to explore balancing the addition of components to the liquid bath to suppress coarsening without killing the dealloying rate.

4.5 Summary and Conclusions

We examined the kinetics of liquid metal dealloying by varying the parent alloy composition, dealloying temperature, and dealloying time. The values measured for the diffusivity and activation energy confirm that the rate-limiting step in the dealloying process is Ti diffusion away from the dealloying interface and out of the dealloyed structure, however a second mechanism may become dominant when the alloy composition is close to the parting limit. Serendipitously, induction heating adds convection to the system, and we predict an increase in the dealloying rate compared to dealloying using resistive heating. The dealloying depth has a power-law relationship with an exponent close to $n = 0.5$, with a deviation

attributed to ligament coarsening adding extra Ti to the Cu bath. Ligament coarsening is very fast at this temperature, increasing from 80 nm to 1 μm in just 10 seconds. We observe two distinct power-law exponents during coarsening owing to ligament pinch-off and surface smoothening events occurring simultaneously. To stymie coarsening we performed LMD experiments in lower-melting point baths, however the low Ti solubility in these baths made it difficult to dealloy to large depths (of order 1 mm). There is a challenge in LMD to fabricate bulk structures with nm-sized ligaments, and future work will need to address this issue. Nevertheless, this chapter is meant to develop a framework for liquid metal dealloying, and lays the groundwork for future research in this field.

Chapter 5 Mechanical Properties of Refractory-based Nanocomposites

5.1 Summary

In this chapter we explore the mechanical properties of nanocomposites fabricated using liquid metal dealloying (LMD). The compressive strength of metal single-crystalline micropillars has been shown to increase with decreasing diameter, but translating this size-dependent strength enhancement to bulk materials has been a challenge; joining of macroscopic materials is inherently challenging and it would be costly to create nano-truss materials using a similar technique (*110*). Recent efforts have produced ~1 mm^3 lattice materials 20 nm features, however this requires a complex combination of lithographic laser writing and decomposition of polymers (*110–112*). Here we utilize LMD as a potential fabrication route for bulk nanostructured materials. The LMD process results in nanocomposites with two distinct phases: a single-crystalline refractory metal network embedded in a Cu-rich matrix. The properties of each phase has the potential to be tailored, and the nanocomposites demonstrate an increase in yield strength that scales with network feature size.

5.2 Background

It is a well-established principle in the mechanics of crystalline materials that smaller microstructural features yield stronger materials. There are numerous manifestations of this effect, including variations in grain size, metallic film thickness, indentation depth, nanowire and micropillar diameter, and ligament diameter in nanoporous metals. The central idea is that dislocation activity is different in reduced volumes where interactions with free surfaces can lead to dislocation starvation, source truncation, or pileup (*113*). An important point of distinction is that these mechanisms can be divided into extrinsic factors (e.g. external crystal dimension) and intrinsic factors (e.g. precipitate size) (*114*). Modern physical metallurgy is founded on designing materials with precisely controlled intrinsic microstructures, e.g. solution and precipitation hardened materials, however extrinsic effects have the potential to play an important role because small-volume materials (e.g. metallic whiskers) approach the theoretical strength of a material (*113*, *115*, *116*). In order to develop new materials with extrinsic "microstructures" recent academic efforts have focused on assembling bulk structures out of nano-scale materials (*111*, *112*).

Nanoporous metals (np-metals) are an interesting class of materials because they are a self-assembled structure and $\sim 1\ mm^3$ of material can be fabricated easily in a laboratory setting (*43–45*). Electrochemical dealloying is quite slow, with an etch rate of $\sim 1\ nm/\sec$, however we showed in the previous chapter that liquid metal dealloying is capable of etching at a rate of $\sim 15\ \mu m/\sec$. Interestingly, the limiting factor in dealloying is the depth of a component, and large volumes could be produced providing the surface area of the component is much larger than its thickness. However, in full disclosure the largest np-metal fabricated to date is

$\sim 1\ cm^3$ and there are significant challenges in scaling up the material which will only be addressed when these materials have found an industrial application (*1*, *45*).

Despite only being used in laboratory setting, np-metals have a high degree of tunability, with the most obvious parameter being the ligament size. To illustrate this point, the as-fabricated ligament size of np-Au is ~10 nm, however the material can be coarsened to ~10 μm by heating in a furnace at 650 ºC for 10 minutes while retaining a self-similar structure (*13*, *35*, *82*). As discussed in the previous chapter the ligament size follows a $t^{1/4}$ relationship, and it is expected that larger ligament sizes ($>100\ \mu m$) could take days to fabricate. Additionally, the starting alloy composition can be altered, resulting in different densities as well as altering the final ligament composition. More radical changes have involved multiple-step dealloying to produce bimodal hierarchical porosity, or adding ternary alloying components to alter the surface chemistry.

5.2.1 Ligament Size Effect in the Yield Strength of Nanoporous Metals

The purpose of this section is to discuss the mechanical properties of np-metals reported in the literature. Using literature data from 15 different publications in Chapter 1, we will address the current limitations and provide an outlook on the future of these materials.

The wealth of the work on the size-dependence of the yield strength in np-metals has been performed on np-Au, however, the scaling laws are expected to be the same for all bicontinuous np-metals (*46–49*, *51*, *53–55*, *57*, *61*). The first important point to address is why yield strength values reported for np-Au have reduced properties compared to bulk Au. Examining Figure 1.5 reveals that only one research group measured yield strengths above the value for bulk Au (~100 MPa) (*117*, *118*). Np-metals have been commonly compared to metallic foams, which

have reduced properties compared to their bulk counterparts. Following the Gibson-Ashby (GA) relation for bending dominant behavior, $\sigma_y^{foam} \propto \left(\rho^*\right)^{3/2}$, where ρ^* is the relative density. The GA relation was derived for low-density foams with high aspect ratios (thickness/length ratio), however np-metals have low aspect ratios where $t/l \approx 1$ (*66*). Nevertheless, we should be able to construct a purely empirical relationship for the yield strength of np-metals as a function of the relative density. Before we can determine the yield strength dependence on relative density we need to establish what fully-dense material we can compare np-metals to. There are many possibilities – Au micropillars, nanocrystalline Au, Au nanowires, and Au thin films – but we will start be examining the size-dependent behavior of np-Au in literature.

Figure 5.1 shows a plot of three different data sets of np-Au: two are hardness data of two different densities compiled from References (*46*, *56*, *66*) , and one data set is compression data of a different density from Reference (*66*). Care was taken to use only relative densities $\rho*$ where there was a significant amount of data, and data sets with relative densities greater than 0.02 were not considered to be the same density. There is a disagreement in the field regarding conversion of hardness to a yield strength for nanoporous metals, which we will discuss below, but we ignore this for now because the conversion uses a scalar and we are only interested in the power-law exponent m from the data.

It is readily apparent that there is a different power-law exponent m associated with each relative density $\rho*$, even though in principle the exponent should be density-independent. Nevertheless, the three data sets display similar scaling, and averaging them yields a power-law exponent $m = 0.59$, which is in close agreement with the power-law exponent reported for single crystal Au micropillars ($m = 0.61$) by Volkert & Lilleodden (*119*) and the general power-law for micropillars ($m = 0.66$) reported by Dou & Derby (*72*). There is an obvious

error in our adaption of the hardness/yield data from the References (since they don't fall on each other), but there is also a seldom-reported error inherently in nanoporous metal data sets, namely, the ligaments in nanoporous metals are three-dimensional shapes and the standard deviation of an average ligament size and length can easily be $\pm 20-30\%$ within each data set. This variation is a direct result of coarsening in porous metals. It should also be expected that the larger ligaments are weaker and play a significant role in the macroscopic mechanical behavior. This idea could be tested by statistically analyzing what percentage of large ligaments would be necessary to induce premature failure.

Regardless, it is important to emphasize that the average value of the power-law is generally larger than the Hall-Petch exponent $m = 0.5$ and smaller than thin films where the strength scales with the inverse of the film thickness, which is to be expected because nanoporous metals are single crystalline within each grain and are not confined materials. We do not believe it is reasonable to compare np-metals to dislocation-starved structures because TEM studies by Balk & Minor have shown that these materials, as formed, have dislocations present which are activated during deformation and do not immediately run out of the sample as shown in *in situ* TEM studies on 200 nm Ni nanopillars (*60*, *113*, *120*). An interesting study on defect-free Mo micropillars showed that there was no increase in strength with decreasing feature size and the reported stress for every diameter was approximately the theoretical yield strength (*121*, *122*); this same work also reported that dislocation starvation did not occur in any of these structures after yielding. It is apparent that there are disagreements in the field of nanomechanics as to the underlying material behavior at the nanoscale and research is ongoing to fully explain experimental observations. In any case, we have shown that np-metals show size-dependent behavior with a power-law similar to that of micro- and nano-pillar materials.

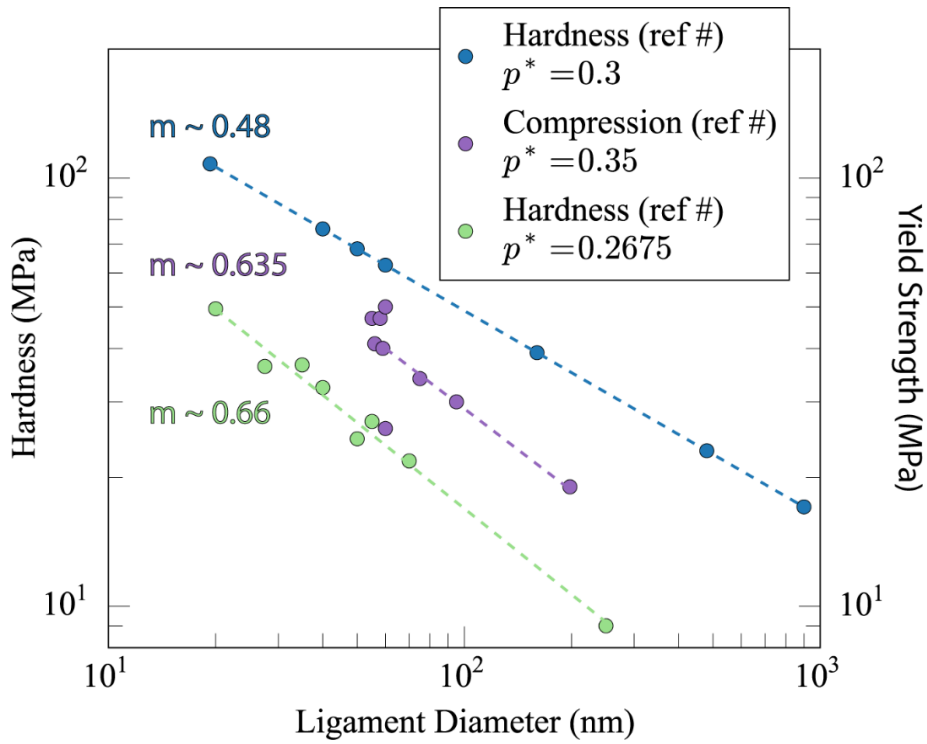

Figure 5.1. Hardness and yield strength data versus ligament diameter for three different densities from References (*46*, *56*, *66*). It is apparent that the strength increases with decreasing feature size, with a power-law exponent similar to that in single crystal micropillars.

As mentioned, Figure 5.1 includes hardness data, which is not an issue when considering size-dependent strengthening, but becomes relevant when comparing the data to yield strength values measured by compression and tension testing. For dense metals the hardness-to-yield strength conversion relationship is typically $H = 3\sigma_y$, where H is the Vickers hardness, but metallic foams with relative densities below 0.3 are fully compressible materials and all deformation is transferred into densification of the ligaments, resulting in the relationship $H = \sigma_y$ (*46*, *51*, *56*). There have been discrepancies between hardness and yield strength data in nanoporous metals deriving from conflicting observations of transverse plastic strain, which

is used to determine the plastic Poisson's ratio and ultimately the true H vs. σ_y relationship. Compression testing by Volkert et al. and Briot & Balk (*57*, *66*) yielded a plastic Poisson's ratio of ~ 0.2 for materials with $\rho^* = 0.33$ and $\rho^* = 0.35$, which yields the relation $H = 2.65\sigma_y$. In a different study, Jin and coworkers (*56*) determined a plastic Poisson's ratio of ~ 0.0 for materials with $\rho^* = 0.26$ and $\rho^* = 0.275$, however there was a limited number of samples tested so it is difficult to confirm this result. Despite observing no plastic strain, the authors in the latter work agreed that the hardness values matched well with their compression values when they used the conversion $H = 3\sigma_y$. It is difficult to make a conclusion regarding the plastic Poisson's ratio because neither group tested the same relative density.

Simulation work has also examined the effect of a plastic Poisson's ratio: finite element modeling by Huber et al. (*64*) demonstrated the plastic transverse strain went to zero with increasing disorder/randomization in the ligaments. A set of molecular dynamics experiments by Farkas et al. (*62*) demonstrated a plastic Poisson's ratio close to zero for samples tested in compression, and a large plastic Poisson's ratio ($0.45 - 0.6$) for samples tested in tension; and a recent MD study by Bao-nam et al. (*63*) showed no transverse strain in compression testing. Unfortunately, these MD simulations looked at materials with relative densities $\rho^* \leq 0.3$ and are not directly applicable to experimental differences. A third set of MD simulations by Sun et al. (*71*) looked at different densities in tension but did not comment on transverse strain.

Despite the differences between these research groups, the hardness data matches well with the compression and tension data if a scalar prefactor 2.65 or 3 is used. Thus, we think it is reasonable to conclude that $H \neq \sigma_y$ is likely most appropriate. For the following discussion we used a prefactor of 2.65.

The above discussion suggests that the function form of the size-dependent yield strength of np-Au is similar to that of micropillars. If we can make such an analogy, it follows that we can treat Au micropillars as a fully-dense material ($\rho^* = 1$) and solve for the Gibson-Ashby (GA) parameters C_σ and n_σ by collapsing the three data sets in Figure 5.1 onto the Au-micropillar data; this exercise yields average values of $C_\sigma = 1.38$ and $n_\sigma = 2.71$. These are similar to the values reported by Briot & Balk (*66*), where $C_\sigma = 1.939$ and $n_\sigma = 2.618$, and significantly different from the values of C_σ and n_σ expected in bending-dominant behavior underpinning Equations (1.1) and (1.2). It was pointed out by Liu & Antoniou (*123*) that the GA relation is true for long-cell walls, but nanoporous metals have short ligaments with low aspect ratios and are expected to behave differently. Unfortunately these empirically derived constants do not reveal the underpinning deformation mechanism(s) of nanoporous metals, and in situ experiments will be necessary to conclude their true behavior.

The goal of determining the GA parameters is to negate the effect of the relative density to compare size-dependent strengthening for a variety of nanoporous materials using the relationship $\sigma_y^{foam} = C_\sigma \sigma_y^{bulk} \left(\rho^*\right)^{n_\sigma}$. The data in Table A.1 represents σ_y^{foam}, and we can back out σ_y^{bulk} using the values of C_σ and n_σ determined above. Figure 5.2a shows the bulk yield strength versus ligament size we would expect if these materials were fully dense. The dashed line corresponds to a fit using the data from Au micro- and nanopillars (*119*), and appears as an average for the corrected data. Finally, Figure 5.2b is the bulk yield strength, material-normalized data for all mechanical data on nanoporous metals, including values of nanoporous Ag, Cu, Pd, and Ti. Unfortunately there is still significant deviation, an order of magnitude, reflecting how difficult it is to fabricate consistent samples between research groups.

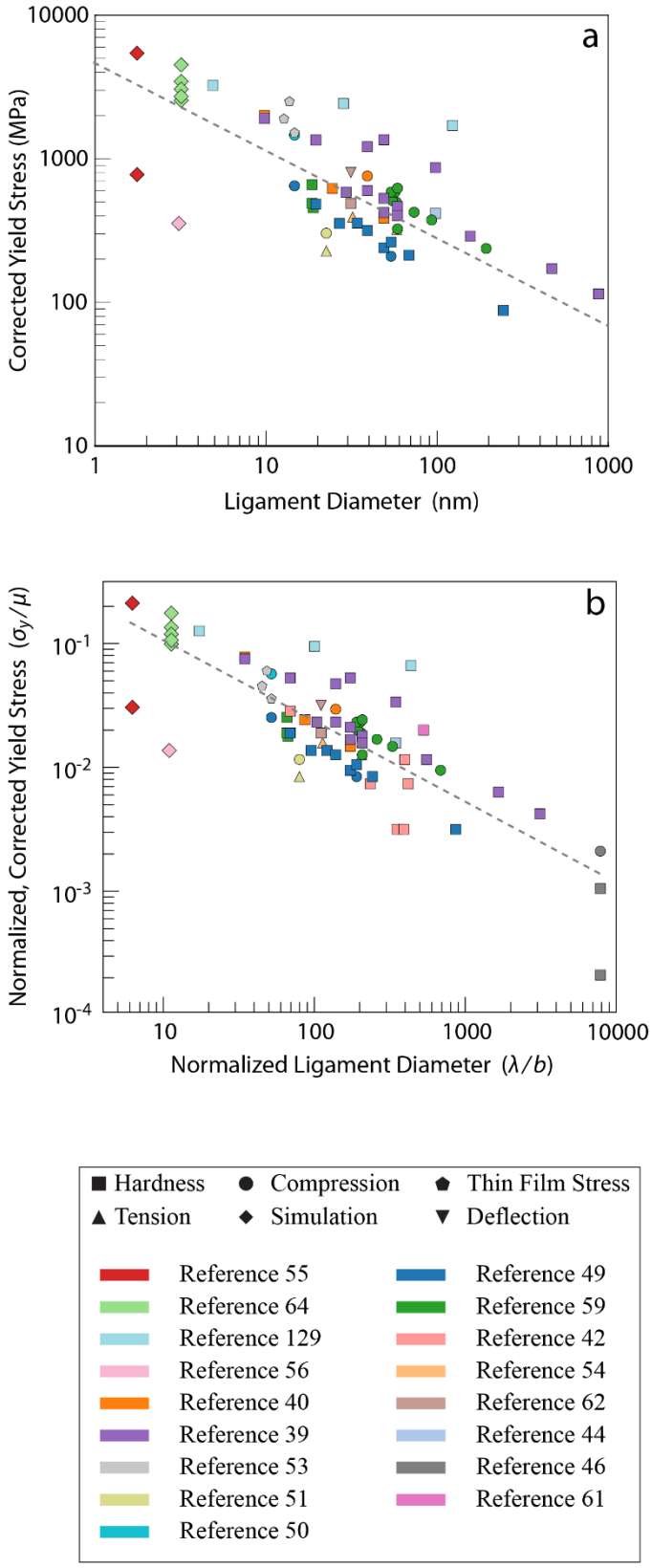

Figure 5.2. Corrected and normalized yield strength data for np-Au and all nanoporous metals.

5.2.2 Nanoporous Metal-Based Composites for Enhanced Ductility

The previous sections have shown that nanoporous metals show size-dependent strengthening, however their low-densities diminish the effects of this property. Additionally, as mentioned in Chapter 1, these materials are macroscopically brittle. Clearly there is a need to develop strategies to improve the mechanical integrity of these materials in order for them to find real-world application. Researchers have developed several different strengthening/toughening strategies to enhance the mechanical properties of dealloyed nanoporous metals. These strategies include creating core-shell structures, refining the pore size, and filling the void space with an electrolyte or polymer (*43–45*, *59*, *76*, *124*, *125*).

The first observation of altering the properties in np-Au was reported by Senior & Newman (*125*), where they observed that np-Au became very flexible when the pores were filled with DI water. This work was briefly explored in (*126*), however, the material had a yield strength and elastic modulus lower than np-Au because it was a metal-water composite. Abdolrahim et al. (*59*) explored the idea of coating the ligaments of np-Au with Ni, and observed a five-fold increase in the strength of the material compared to np-Au. The Ni phase underwent significant twinning, accommodating plasticity in the material and may have allowed for work hardening in the Au phase, leading to a macroscopically ductile material. Similar strengthening has been observed in coated micropillars and confirm that the performance increase is not the result of a skin-thickness effect. More recent strengthening strategies to improve the mechanical properties of nanoporous metals have involved infiltrating the porous phase with a secondary material. Wang & Weissmuller (*43*, *44*) examined metal-polymer composites, and saw significant increases in ductility and strength, even achieving 10% strain in tension. These composites are fully dense materials and are expected to undergo different modes of

deformation, similar to those observed in (*59*, *127*, *128*), and Gibson-Ashby relations are not applicable in these materials. We will explore this in the following sections, but a size-dependent rule of mixtures model may be more appropriate.

In this chapter we expand on the idea of filling the pores of nanoporous metals, using the LMD process to create high-strength *composite* materials by allowing the dealloying medium to solidify inside the pores. The composite materials we fabricated show a ten-fold increase in yield strength when we decrease the feature sizes from 10 μm ($\sim 250\,MPa$) to 70 nm ($\sim 2.5\,GPa$), while still retaining plastic behavior. This is the first report of metal-metal bicontinuous nanocomposite materials and the first assessment of their mechanical behavior.

5.3 Experimental Methods

5.3.1 Ingot and Bath Preparation

50g $Ti_{65}Ta_{35}$, $Ti_{20}Ta_{80}$, and $Ti_{75}W_{25}$ alloy buttons were prepared by the Materials Preparation Center at Ames Laboratory. The raw materials used were Ti (99.9 wt.%), Ta (99.9 wt.%), and W (99.9 wt.%). The Ti-W alloy has an extremely high melting point, and the as-received button was not fully dense; the button was remelted by Arcast, Inc. using a water-cooled cold crucible. Approximately 1 cm^3 ingots for LMD were cut using wire electrical discharge machining (EDM), and then annealed via induction melting in a ultra-high vacuum (10^{-8} torr) environment at ~ 1500 ^oC for 72 hours.

Metal baths for the LMD process were prepared by premelting ~20 g ingots of Cu, and $Cu_{32}Ag_{68}$. Commercially pure Cu (99.99 wt .%), and Ag (99.99 wt. %) pellets were melted in a graphite crucible under flowing Ar. Control samples of $Cu_{90}Ti_{10}$, $Cu_{75}Ti_{25}$, $Cu_{65}Ti_{35}$, and

$Cu_{50}Ti_{50}$ were fabricated in-house using induction melting using Ti (99.98 wt.%) and Cu used above.

5.3.2 Composite Fabrication

Composites were fabricated using an LMD process by immersing individual Ti-X ingots into a 20 g bath of molten Cu/Ag in an ultra-high purity alumina crucible cast in-house using materials from Cotronics Corp. Induction melting was used to heat the samples under flowing Ar (99.99%), and the LMD process was run for a set time. Samples details are included in Table 5.4.

Table 5.1. Mechanical data from microtensile tests.

Sample	Ligament Size (μm)	Immersion Time (sec)	Number of Tests	Type of Test
Ta/Cu	10.56 ± 0.31	20	4	compression
Ta/Cu	7.65 ± 0.36	15	6	compression
Ta/Cu	5.24 ± 0.44	10	7	compression
Ta/Cu	3.00 ± 0.58	5	3	compression
Ta/CuAg	0.500 ± 0.020	20	20	nanoindentation
Ta/CuAg	0.117 ± 0.014	10	20	nanoindentation
Ta/CuAg	0.071 ± 0.015	5	20	nanoindentation
W/Cu	0.656 ± 0.107	20	4	compression
W/Cu	1.154 ± 0.200	15	4	compression
W/Cu	1.500 ± 0.050	15	10	microindentation
W/Cu	0.200 ± 0.040	10	10	microindentation
W/Cu	0.109 ± 0.021	5	10	microindentation
W/Cu	0.049 ± 0.08	3	10	microindentation
W/Cu	0.030 ± 0.015	2	10	microindentation

We cut, polished and imaged cross sections to ensure full Cu penetration into the Ti-X ingots and that the nanocomposites had a uniform ligament size. Nanocomposite samples were mounted in Struers PolyFast conductive epoxy, and underwent: grinding steps of 400 grit, 600 grit; diamond polishing steps of 9 μm, 3 μm, 1 μm; and a final polishing step of .05 μm. Composites were characterized using a JEOL scanning electron microscope (SEM) and ImageJ was used to measure dealloying depth and average ligament sizes. EDS was used to determine the composition of each phase as a function of depth. Average ligament sizes were determined by drawing lines across SEM images in ImageJ and measuring ligaments diameters along the line. At least 50 ligaments were measured from multiple images. We did not quantify the grain size in the Cu phase or the volume fraction and size of the CuTi precipitates although they are expected to play an important role in the mechanical properties. Compositions of the Ta and Cu phases in the composites were measured using energy-dispersive X-ray spectroscopy (EDS). A summary of the compositional data can be found in Table 5.2.

Table 5.2. Compositional data for Ta/Cu and Ta/CuAg composites.

Material	$Ta\,(at.\%)$	$Cu\,(at.\%)$	$Ti\,(at.\%)$	$Ag\,(at.\%)$
Ta phase (3,5.2 μm)	80 ± 5	0	20 ± 5	0
Cu phase (3,5.2 μm)	0	75 ± 8	25 ± 8	0
Ta phase (7.7,10.6 μm)	80 ± 5	0	20 ± 5	0
Cu phase (7.7,10.6 μm)	0	90 ± 3	10 ± 3	0
Ta phase (70, 117, 500 nm)	77 ± 10	0	23 ± 10	0
CuAg phase (70, 117, 500 nm)	0	35 ± 2	59 ± 2	6 ± 2

5.3.3 Mechanical Testing

Microtensile testing was performed at a strain rate of 2×10^{-4} using a $445\ N$ load cell with a resolution of 0.426 N, and strain was measured using a digital image correlation method reported in previous works (*129*, *130*). The cross-sectional area was determined from five SEM measurements per sample with a standard deviation of $\pm 3\%$, which corresponds to a stress variation of ± 8 MPa. Compression testing was performed at a strain rate of 2×10^{-3} using a $20\ kN \pm 45\ N$ load cell, and strain was measured using digital image correlation. Compression sample dimensions were measured using Mitutoyo digital calipers, and the total error in stress measurement was ± 16.9 MPa. Details of the stress-strain curves and digital image correlation for strain estimates are included in Appendix C.1.

Nanoindentation testing was performed using a Nanomechanics iNano indenter with a Berkovich tip. A continuous stiffness measurement technique was used and samples were indented at a constant strain rate of $0.2\,s^{-1}$ up to a depth of 500 nm, and values were averaged over the depth range 200–500 nm.

5.3.4 W/Cu TEM and APT Preparation

W/Cu nanocomposite specimens were prepared for Transmission Electron Microscopy (TEM) and atom problem tomography (APT) by Eric Xu and Mingwei Chen at Tohoku University, Sendai, Japan.

Thin foils for scanning transmission electron microscopy (STEM) observations were prepared by ion milling at the ion energy of 2 kV and an incident angle of ±6. The TEM specimens were cooled by liquid N2 during ion milling. Sharp tip specimens for atom probe tomography (APT) were made by electrochemical micro-polishing and followed by focused

ion beam milling to reduce the size of the tips down to a few hundred of nanometers (JIB-4601F, JEOL). The finished tip profiles were examined by scanning electron microscopy (SEM) for APT reconstruction. The data acquisition was performed using a local electrode atom probe (LEAP 4000HR) equipped with an energy compensated reflectron, by which the mass resolution can be greatly improved. The APT acquisition temperature was set at 50 K, and the pulse frequency and pulse fraction were 200 kHz and 20%, respectively. The CAMECA Integrated Visualization and Analysis Software (IVAS 3.6.6) package was used for data processing and three-dimensional (3-D) atomic reconstruction.

The STEM observations were conducted on a JEOL JEM-2100F instrument equipped with double spherical aberration correctors for probe forming and image forming lenses. High-angle annular dark-field (HAADF) STEM images were taken using an annular-type detector with a collection angle ranging from 100 to 267 mrad, while bright-field (BF) STEM images were simultaneously recorded using a STEM BF detector. Chemical analyses were carried out by means of electron energy loss spectroscopy (EELS) and energy dispersive X-ray spectroscopy (EDX). EELS and EDX elemental mapping and spectra were acquired using a Gatan GIF Tridiem and JEOL JED-2300T, respectively.

5.4 Results and Discussion

5.4.1 Tantalum-based composites

5.4.1.1 Compression and Hardness Testing

Figure 5.3 displays bulk, metal-metal composite samples fabricated by our own variation of the LMD process. In this figure we show ~1 cm^3 Ta/Cu material fabricated from a TiTa starting material with ~500 µm grains. Figure 5.4 illustrates the features of this bicontinuous composite: The new material is polycrystalline, consisting of individual, single-crystal bcc refractory micropillar networks (the “dealloyed phase”), and a rapidly solidified Cu phase (the “matrix phase"), containing Cu-Ti intermetallic precipitates**.**

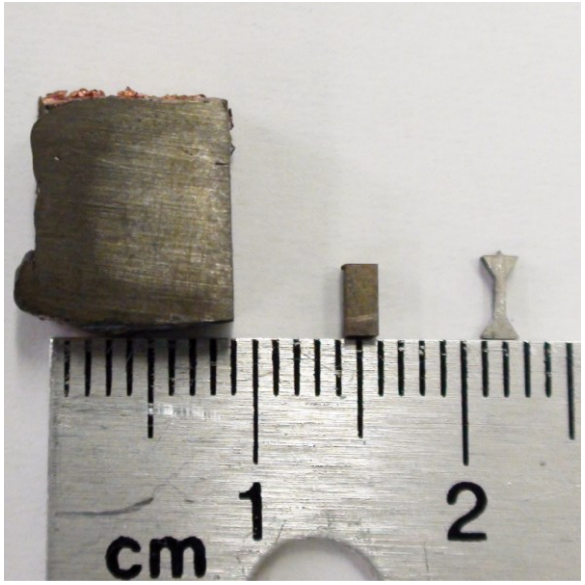

Figure 5.3. Bulk nanocomposites made by liquid metal dealloying. (A) Examples of as-made Ta-Cu nanocomposites; ~1 cm^3 ingot (left), compression testing sample (center), microtensile sample (right).

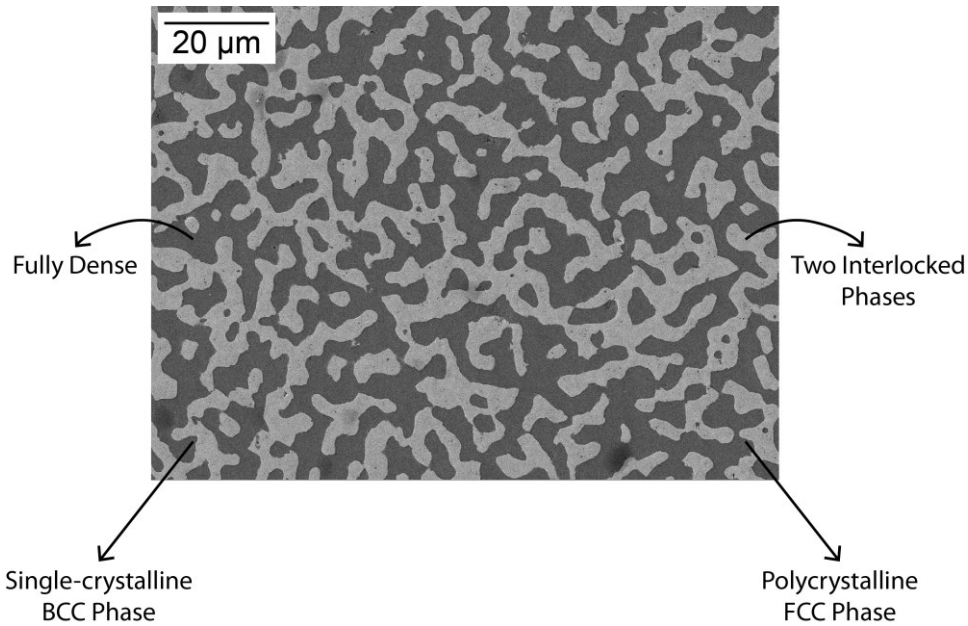

Figure 5.4 Bicontinuous metal/metal composite. This is a new microstructure, featuring two interpenetrating phases. Unlike precipitation hardening the secondary phase is continuous, and unlike multilayered materials the phases are constrained in two dimensions.

Figure 5.5a shows graphs of engineering stress versus engineering strain from compression tests on macroscale samples (~5-7 mm^3) at a strain rate of $2\times10^{-3}\,s^{-1}$. There is an increase in yield strength σ_y for samples with smaller ligament size λ and all samples show significant plastic strain before failure. There is an obvious question as to whether or not we can compare these four compression samples with each other. Table 5.2 illustrates that the Ta phase ligaments are approximately the same however the Cu phase has significantly different compositions. Table 5.3 shows that the yield strength for reference samples of $Cu_{90}Ti_{10}$ and $Cu_{75}Ti_{25}$ differ significantly ($\sim 350\ MPa$), however a rule of mixtures estimate for the bulk composite (yield strength multiplied by volume fraction) shows the yield strength is only off by $\sim 100\ MPa$. It is likely there are additional discrepancies in the microstructure of the Cu phase at different ligament sizes which were unable to be captured by our reference samples

such as the grain size and intermetallic precipitate size. This can be conceptualized by considering solidification of the Cu phase in finite volumes (the pores between Ta ligaments), but this is not an easy task to model. We performed EBSD on our composites (not shown in this work), and the Ta phase was readily captured but it was very difficult to get clean data on the Cu phase. This was due to a combination of difficulty in polishing composite samples and the inherent heterogeneity of the Cu phase. It would be useful to characterize the size-dependent microstructures using TEM, however this is out of the scope of this work.

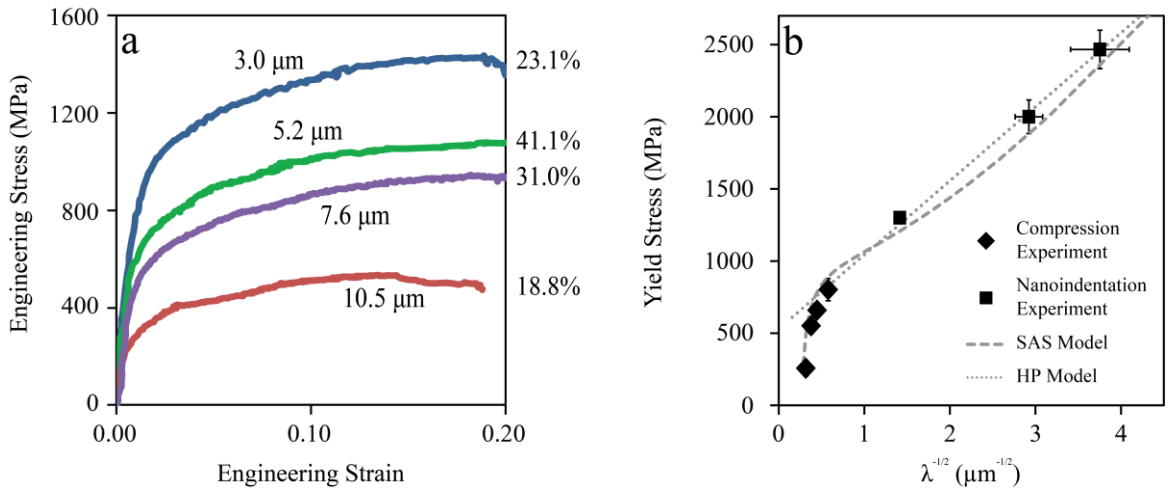

Figure 5.5. Mechanical characterization of the Ta-Cu composites in compression. (a) Stress-strain curves for Ta-Cu composites with different ligament sizes. Curves were cut off at 20% strain; strains to failure are indicated next to each curve. (b) Plot of yield strength vs. ligament size: (black diamonds) experimental measurements on Ta-Cu composites from compression experiments; (black squares) experimental measurements on Ta-CuAg composites from nanoindentation experiments; (large dashes) strength estimate using the single-arm dislocation source model with a linearly decreasing dislocation density at yield $\rho(\lambda)$; (fine dashes) strength estimate using the Hall-Petch model.

In addition to the compression samples, we fabricated smaller ligament composite samples (Figure 5.6) in order to probe the size dependence of our material at the nanoscale. We were able to make samples with smaller ligaments by using a liquid metal bath with a lower melting point than Cu, e.g. $Ag_{62}Cu_{32}$, whose solidified fcc phase has similar mechanical properties to

Cu, Table 5.3. We assessed these materials using nanoindentation and estimated the yield strength using $\sigma_y = 2.65 * H$. The materials were exceptionally hard and the data is included in Figure 5.5b along with the yield strength data from compression testing.

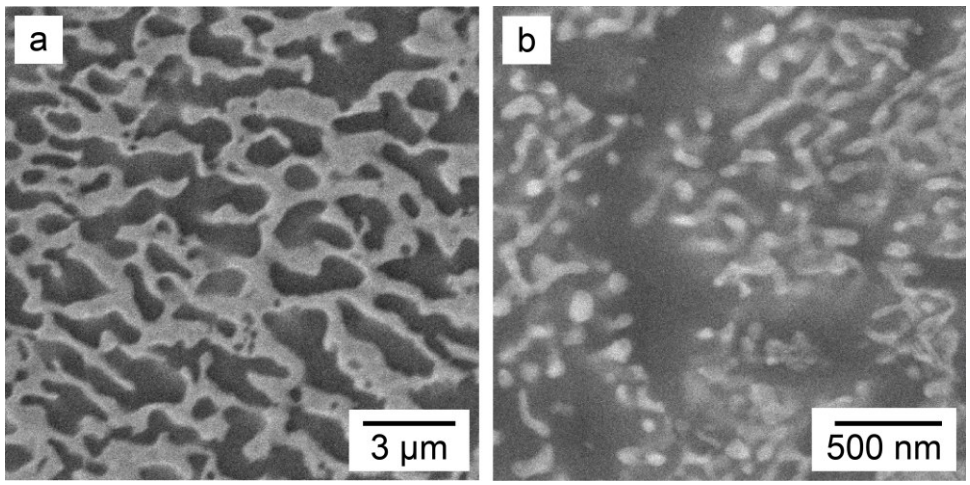

Figure 5.6. Ta composites were fabricated with smaller ligament sizes using a CuAg (~780 ºC melting point) liquid metal bath. (A) ~500 nm Ta-CuAg nanocomposite. (B) ~70 nm Ta-CuAg nanocomposite. The 50 nm final polishing step can cause damage to surface ligaments when the ligaments are of a comparable size.

In order to understand our material's size dependent strengthening we compared the yield strength data to two popular strengthening models used for nanostructured materials: the single arm source dislocation model and the Hall-Petch model. The parameters used in the following discussion can be found in Table 5.3. The single arm source model is used to describe the strengthening behavior in single-crystal micropillars, and the critically resolved shear stress τ_{CRSS} is given by

$$\tau_{CSRR} = \tau_0 + 0.5\mu b\sqrt{\rho} + \frac{\alpha\mu b}{\bar{\lambda}}\ln\left(\bar{\lambda}/b\right) \tag{5.1}$$

where τ_0 is the lattice friction stress, μ is the shear modulus, b is the magnitude of the Burgers vector, ρ is the dislocation density at yielding, α is a geometric constant with a value ~ , and $\bar{\lambda}$ is the average length of the weakest single arm dislocation source (*131*). The Hall-Petch model is used to describe the strengthening behavior in nanocrystalline and multilayer materials, and reasonably captures the data for layers and grain sizes larger than 100 nm. The yield strength σ_y is given by

$$\sigma_y = \sigma_0 + kh^{-1/2} \tag{5.2}$$

where, σ_0 is the lattice friction stress, k is the strengthening coefficient, and h is the characteristic lengthscale of the microstructure (typically grain size but ligament diameter in our case) (*132*).

The Hall-Petch model does not fit our large ligament data, as the yield strength has a clear non-linear relationship with $\lambda^{-1/2}$, but we see good agreement with our smaller ligament samples (3 µm, 500 nm, 117 nm, 70 nm), yielding $k = 0.51 MPa\sqrt{m}$, and $\sigma_0 = 530\, MPa$. The value of σ_0 is higher than our largest ligament sample, but is comparable to a rule of mixtures estimate $\sigma_y^{Ta-Cu} = 559\ MPa$ using the yield strength of $Ti_{20}Ta_{80}$ and $Cu_{25}Ti_{75}$ (Table 5.3). The strengthening coefficient for the composite is slightly higher than either component, $k_{Ta} = 0.31\ MPa\sqrt{m}$, and $k_{Cu} = 0.14\ MPa\sqrt{m}$, but is still in reasonably good agreement (*133*).

The single arm source model captures the significant size-dependent strengthening we see at all composite lengthscales under the hypothesis that the dislocation density at yield is itself a function of the ligament size. This is a similar analysis to Conrad who proposed the Hall-Petch effect is the result of a higher dislocation density at smaller grain sizes (*134–136*); this is simply the result of considering smaller slip lengths in finite volumes. In this model, for

a given strain the dislocation density the dislocation density follows a $d^{-1/2}$ relationship. Adding a similar relationship we produce a modified single arm source model that accounts for constrained volumes because we qualitatively expect significant pile up in our composites. Fitting the model to the yield strength for the 10.5 μm ligament sample we estimate a dislocation density at yield of $\rho \approx 7.0 \times 10^{13}\ m^{-2}$, and fitting the model to match the yield strength for the 70 nm ligament sample yields an increased dislocation density of $\rho \approx 1.4 \times 10^{15}\ m^{-2}$. Plotting the dislocation density at yield versus ligament size shows a linear increase in the dislocation density with decreasing λ. This estimated range of values for dislocation densities in the composites are reasonable, and consistent with dislocation densities reported for micropillars (*75*, *127*).

Table 5.3 Material parameters used in our analysis.

Material	$\sigma_y\,(MPa)$	$E\,(GPa)$	$\mu(GPa)$	$b(\mathring{A})$	$\rho(g/cm^3)$	$\tau_0\,(MPa)$
$Cu_{90}Ti_{10}$	566 ± 48*	159 ± 6*	61 ± 2**	2.556^{Cu}	7.25*	34.8^{Cu}
$Cu_{75}Ti_{25}$	900 ± 52*	142 ± 11*	55 ± 4**	2.556^{Cu}	6.75*	34.8^{Cu}
$Ti_{20}Ta_{80}$	376 ± 41*	200 ± 10*	77 ± 4**	2.83^{Ta}	9.55*	47^{Ta}
Ta/Cu	442^{ROM} 559^{ROM}	180 ± 10*	69 ± 4**	2.68^{RoM}	8.8*	40^{RoM}
Ta/CuAg (500 nm)	1300 ± 33***	170 ± 6*	65 ± 2**	-	-	-
Ta/CuAg (117 nm)	1200 ± 117***	158 ± 12*	61 ± 5**	-	-	-
Ta/CuAg (70 nm)	2466 ± 133***	175 ± 10*	67 ± 4**	-	-	-
CuAg	220 ± 16***	157 ± 6*	60 ± 2**	-	-	-

* -Experimentally measured
** -Estimated from experimental using the relationship: $\mu = E/2.6$
*** -Converted from hardness using the relationship: $\sigma_y = hardness\,/\,2.65$
GA-Gibson-Ashby estimate
Cu-Property of elemental Copper (*115*), Ta-Property of elemental Tantalum (*140*)
ROM-Rule of mixtures estimate

In the composites here, the Ta phase is essentially a single crystal, but the Cu phase is polycrystalline, and one mechanism (single arm source or Hall-Petch) may dominate depending on the ligament size. Each phase in the composite is geometrically constrained so we expect both phases to have the same strain, $\varepsilon_{Ta} = \varepsilon_{Cu}$, but we do not expect both phases to have the same stress because they do not have equal volume fractions. This is a complex system and it is not obvious that Equations (5.1) or (5.2) can fully capture dislocation evolution and interactions in these bicontinuous composites without refinement. Regardless of the

strengthening mechanism(s), excavation of the dealloyed refractory phase after deformation shows evidence of dislocation activity through the presence of slip traces (Figure 5.7a,b) in the Ta phase. The Ta ligaments (Figure 5.7c) have obvious Cu-rich inclusions (confirmed by EDS) that result from Rayleigh instabilities during coarsening and are not seen in the parent alloy (*35*).

Similar to coated micropillars or passivated thin films, dislocation activity in the NPM composite was neither stochastic nor catastrophic (*128*, *137*, *138*). For these reasons, the composites studied here are able to strain harden and support large plastic strains, and ultimately fail via delamination within grains (Figure 5.7c). Moreover, the composite architecture allows for incorporation of size-scale effects without the collapse that occurs in cellular materials and foams (*111*). Previous studies on the mechanical properties of dealloyed nanoporous metals show that individual ligaments are ductile, but the overall structure is not able to undergo significant macroscopic plastic deformation in tension (*58*, *61*). Plasticity has been reported in compression, with densification, dislocation motion, and dislocation storage occurring simultaneously (*56*). In contrast, the fully-dense network microstructure of our bulk composites manifests size-dependent mechanical properties associated with the internal lengthscales that evolved during dealloying without any additional strain associated with densification.

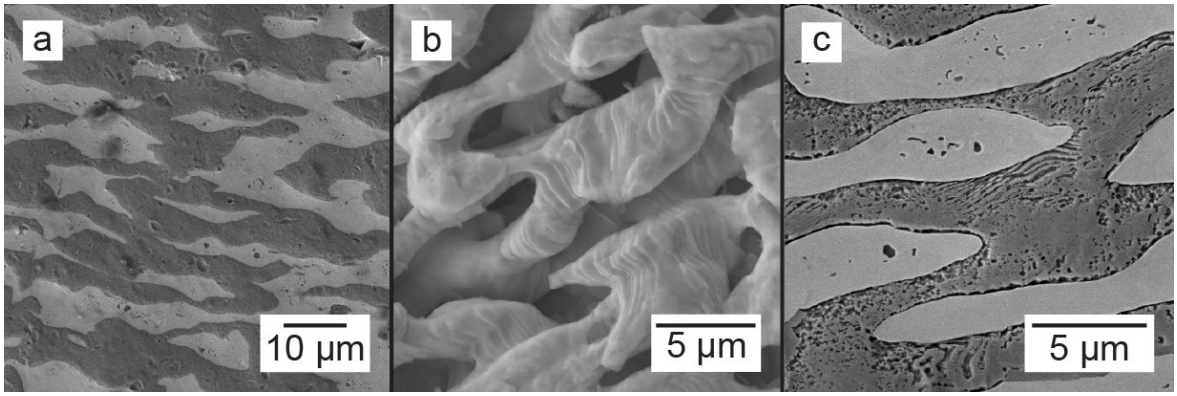

Figure 5.7. Deformed Ta-Cu composites. (a) SEM micrograph of the deformed composite. (b) SEM micrograph of the dealloyed Ta phase, excavated after deformation. (c) SEM micrograph of a deformed Ta-Cu composite near to failure, showing delamination between the Ta and Cu phases.

5.4.1.2 Microtensile Results

Due to a difficulty in sample preparation, we only tested a small number of Ta/Cu samples, 3 of which were ductile. The three ductile samples were from a preliminary batch and the four brittle samples were from a second batch of dealloyed samples. We will discuss in the following section the origins of ductile and brittle behavior in these materials, but for now we will refer the reader to Figure 5.8 and Figure 5.9 to show how drastically different the two batches were. Table 5.4 includes the yield strength data determined from the samples tested in tension along with Ta and Cu references.

The average ligament size of the samples was ~ 6 μm and the average yield strength of the ductile samples was $\sim 645\,MPa$, which agrees well with the observed trend in our compression measurements (our modified SAS model predicts $\sigma_y\left(6\ \mu m\right) \approx 600\ MPa$). Figure 5.10 compares a stress-strain curve of the Ta/Cu composite to curves for pure Ta and pure Cu. The composite is stronger than either component (although these are not representative components), but is not as ductile. During all load tests the grips often lagged and we did not have good correlation with the DIC software during the initial loading. As a result the modulus

values during the initial loading are not accurate and the modulus needed to be determined during load/unload cycles. The load/unload cycles resulted in accurate modulus values for the Ta and Cu samples, but we observed a hysteresis during two load/unload cycles for one of the three Ta/Cu samples (Figure 5.11), and measured a very low modulus value ($\sim 75\ GPa$). It is possible there is time-dependent behavior associated with reversible twinning in the Cu phase or destruction of the Ta/Cu interface, but we need to perform more tests to conclusively determine what happened.

Interestingly, all of the composites experienced their maximum stress at yield. Once the samples began to yield the behavior was almost perfectly plastic. In compression we observed work hardening at all ligament sizes, but we do not have enough statistics to conclude the behavior in tension. In section 4.4.7 we discussed how the connectivity of the structure is strongly dependent on composition, time, and temperature; it is possible the samples we tested in tension did not have a high enough connectivity to take advantage of the interlocked structure. This work was performed before our in-depth kinetic study and it will be worthwhile to revisit these experiments with our new knowledge base. Large batches of samples for microtensile testing can dipped into baths of Cu and the microstructure can be more finely tuned. Nevertheless, it is quite promising that some of the tensile samples were ductile because this is the first reporting of a ductile nanoporous material.

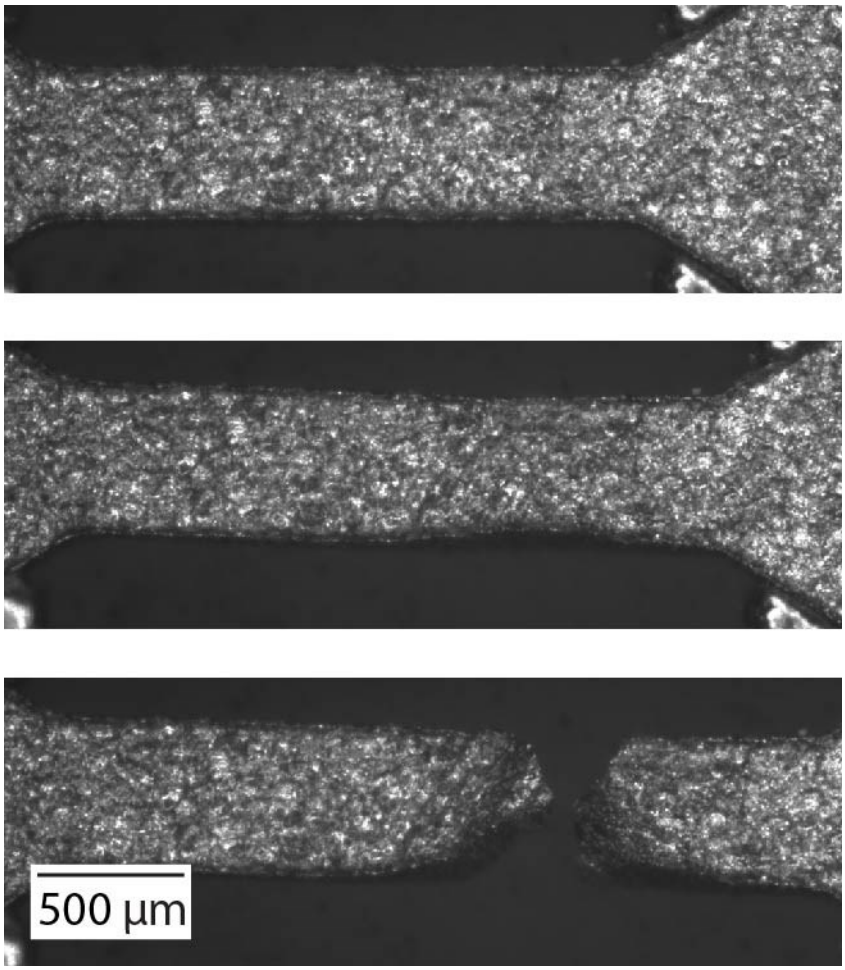

Figure 5.8. Example of microtensile test showing ductile behavior for a Ta/Cu composite. Note the necking and cup/cone shape in the failed region.

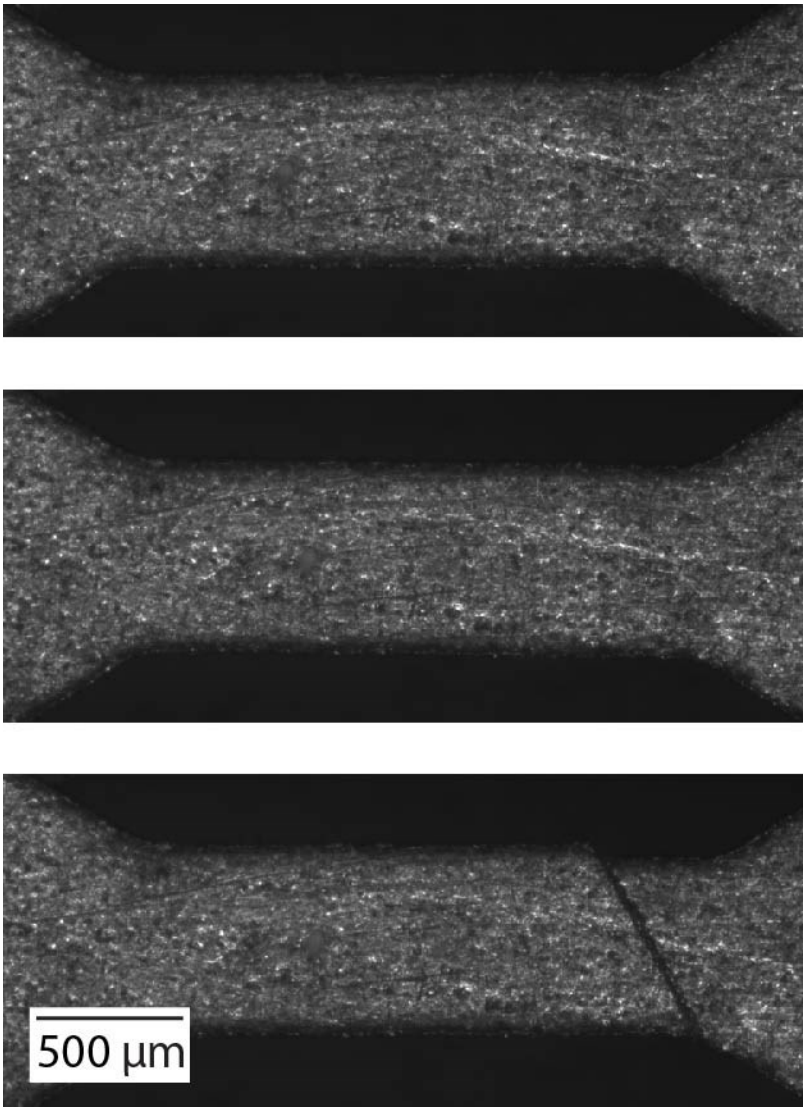

Figure 5.9. Example of microtensile test showing a ductile behavior for a Ta/Cu composite. Note the sharp crack at ~45° angle and lack of plastic deformation in the sample.

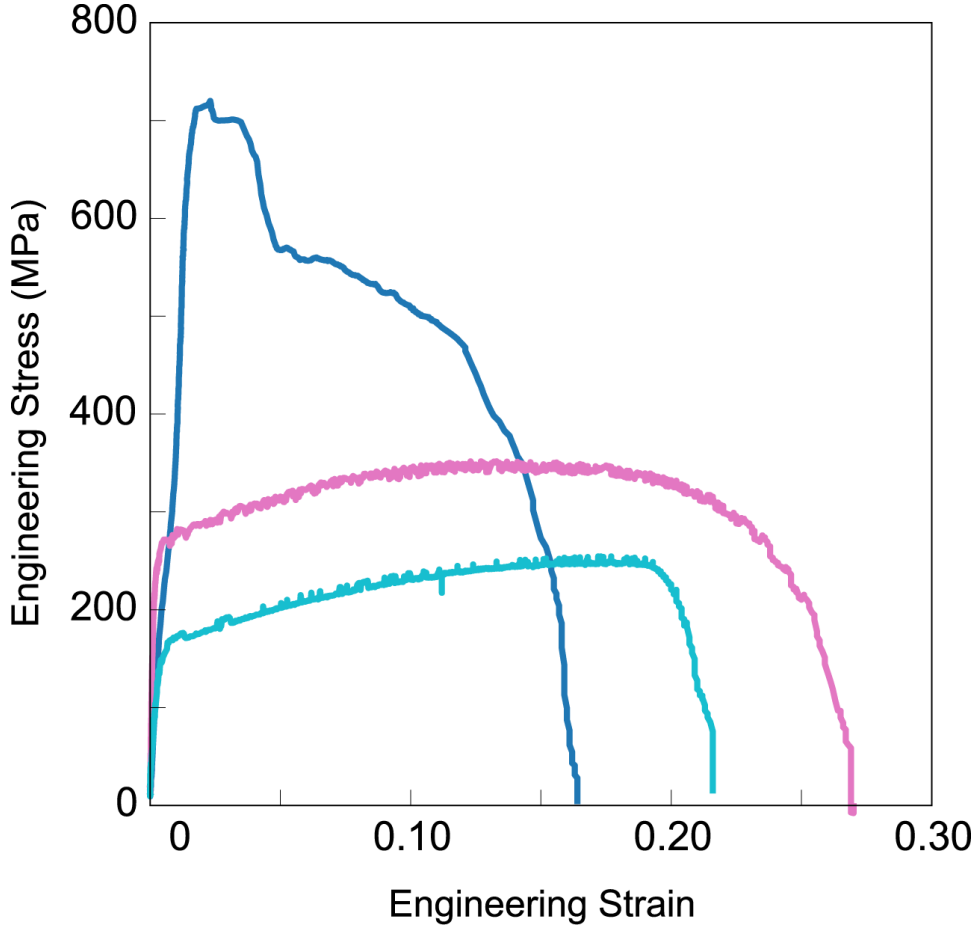

Figure 5.10. Comparison stress strain curve from microtensile testing: composite sample (blue), pure tantalum (pink), and pure cu (teal). The composite is stronger than either component but surprisingly less ductile. This is not a rigorous comparison but meant to illustrate that the material – at the very least – is not weaker than the pure components.

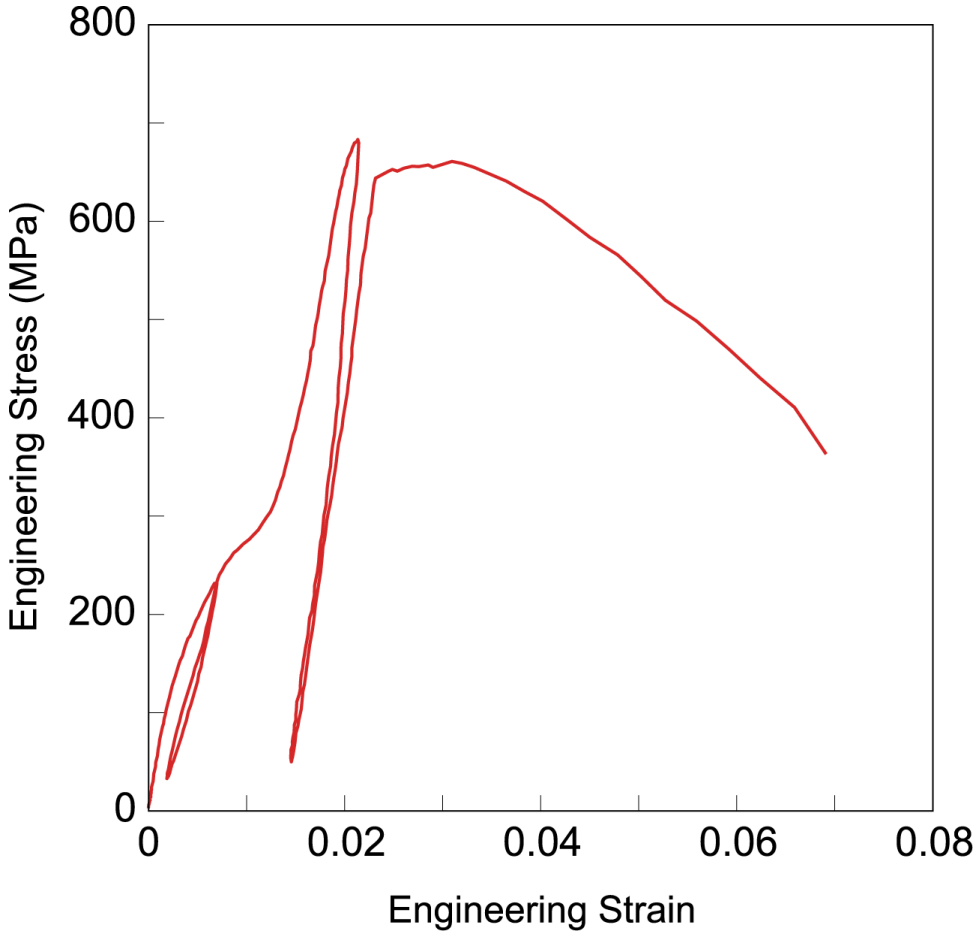

Figure 5.11. Stress strain curve for one of the Ta/Cu composite samples where two unload/load cycles were performed. There was significant lag and a slight hysteresis in the behavior.

Table 5.4. Mechanical data from microtensile tests.

Sample	Yield Strength (MPa)	Maximum Stress (MPa)	Modulus (GPa)	Strain at Failure
Ta/Cu 1	720	*	-	0.108
Ta/Cu 2	535	*	-	0.164
Ta/Cu 3	683	*	74	0.069
Ta/Cu 4	255	*	-	0.0015
Ta/Cu 5	225	*	-	0.0028
Ta/Cu 6	170	*	-	0.0029
Ta/Cu 7	142	*	-	0.0012
Ta 1	230	363	180	0.269
Ta 2	215	352	175	0.35
Ta 3	210	366	-	0.22
Cu 1	120	237	85	0.30
Cu 2	110	220	80	0.224
Cu 3	112	254	-	0.216

*indicates same as yield strength

5.4.1.3 Grain Boundary Character

High tortuosity in the interface between the matrix and dealloyed phases helps delay direct delamination between phases and early failure as seen in multilayers (*139*) and allows for large strains compared to the constituent phases alone. However, there are still subtle effects of the structure of grain boundaries on work hardening and failure at scales much larger than the ligaments (Figure 5.12). For instance, within a batch of compression samples with 7 μm feature sizes, all had the same yield strength, but some samples underwent significant deformation – over 65% strain – and significantly work hardened to compressive engienering stresses near 2.0 GPa without failing while others failed at ~950 MPa and 31% strain (Figure 5.12a). Similar effects were observed in microtensile tests (Figure 5.12b): samples with identical feature sizes and compositions had drastically different plasticity behaviors. Unlike in compression, where all samples underwent some amount of plastic deformation, microtensile specimens were either ductile or brittle.

The primary difference between the samples in Figure 5.12c,d and the samples in Figure 5.12e,f was their grain boundary structure. The high-strength, large-strain samples all showed Ta-rich grain boundaries interconnecting adjacent grains Figure 5.12c,d) in contrast to “detached” grain boundaries seen in the weaker samples (Figure 5.12e,f). The Ta grains in our nanocomposites are quite large, ~500 μm in diameter, and only a few are needed to span the microtensile and compression samples. We speculate that cracks can easily propagate along the "detached" grain boundaries, and interconnected boundaries add fracture resistance. We showed in Figure 5.7c that if the material does not fail prematurely at a grain boundary it eventually fails via delamination between the matrix and dealloyed phases. This dependence on grain boundaries is troubling from a materials fabrication perspective but we think that this

can be overcome and requires a detailed study on bulk mechanical properties with carefully designed morphologies and microstructures, i.e. different starting alloy compositions ($Ti_{40}Ta_{60}$ versus $Ti_{85}Ta_{15}$) and different grain sizes (10 µm versus 500 µm)

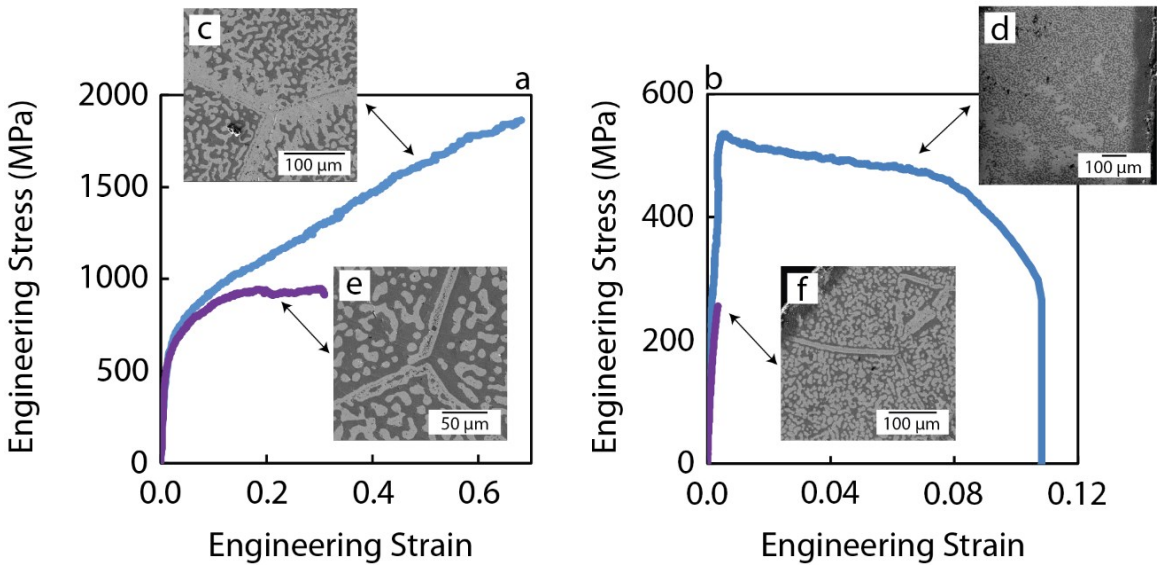

Figure 5.12. Deformation behavior dependence on grain boundary structure. (A) Compressive stress-strain curve for two 7-micron Ta-Cu composites with drastically different grain boundary structures. (B) Tensile stress-strain curve for two 3-micron Ta-Cu composites with two different grain boundary structures. (C) and (D) SEM micrographs of the grain boundary structure in the blue curve sample, which resulted in large plastic strains. (E) and (F) SEM micrographs of the grain boundary structure in the purple curve sample, which resulted in significantly lower plastic strains.

5.4.2 Tungsten-based compositions

5.4.2.1 Compression and Hardness Testing

We were also interested in studying the mechanical properties of W/Cu composites because we can fabricate smaller ligament samples than Ta/Cu composites without needing to use lower temperature baths. An additional benefit is that W/Cu is more of a classic composite material, consisting of a hard brittle phase (W) and a ductile soft phase (Cu).

We fabricated compression samples of W/Cu composites with ~650 nm and ~1.1 μm ligaments, but the dealloying was too sluggish to reliably create samples for compression testing with smaller ligaments. Microhardness testing was used to measure the properties of the smaller ligament sizes and we plotted the hardness versus ligament size in Figure 5.13. We converted the compression yield strength values to a hardness value because the majority of the data were hardness measurements, and used the relation from section 5.2.1, $\sigma_y = H/2.65$. Performing a Hall-Petch fit we determined $k_{W/Cu} = 0.77\ MPa\sqrt{m}$ and $\sigma_0 \approx 1\ GPa$, compared to $k_{Cu} = 0.14\ MPa\sqrt{m}$ and $k_W = 3.1\ MPa\sqrt{m}$. A rule of mixtures estimate for the composite yields $k_{W/Cu} = 0.81\ MPa\sqrt{m}$, in close agreement.

It is obvious that with decreasing ligament size the composite becomes stronger than either of these estimates. We did not include a GA analysis for the bulk composite because we showed in section 5.4.1.1 that deformation in the composite is very different from the porous material. For comparison we included two rule of mixtures estimates for the hardness of the bulk W/Cu composite. There are two estimates because the composition of the Cu phase varied significantly depending on the ligament size, with smaller ligaments being associated with higher Ti concentrations. Table 5.5 shows that although the CuTi compositions were quite different the hardness values of the $Cu_{75}Ti_{25}$, $Cu_{65}Ti_{35}$, $Cu_{50}Ti_{50}$, compositions were nearly

identical. For ans estimate of the W phase we measured a hardness value of $4.6 \pm .2\ GPa$ for pure tungsten. In any case these values appear to be a good lower bound for the W/Cu composite materials.

Table 5.5. Summary of the Cu phase composition for the W-Cu ligament sizes tested

Ligament Size (nm)	Cu-Ti atomic composition	Vickers Hardness of the Cu phase (HV)
30 ± 15	$50-50$	390 ± 20
49 ± 7.5	$65-35$	380 ± 18
109 ± 21	$75-25$	386 ± 22
200 ± 40	$75-25$	386 ± 22
1500 ± 50	$90-10$	279 ± 14

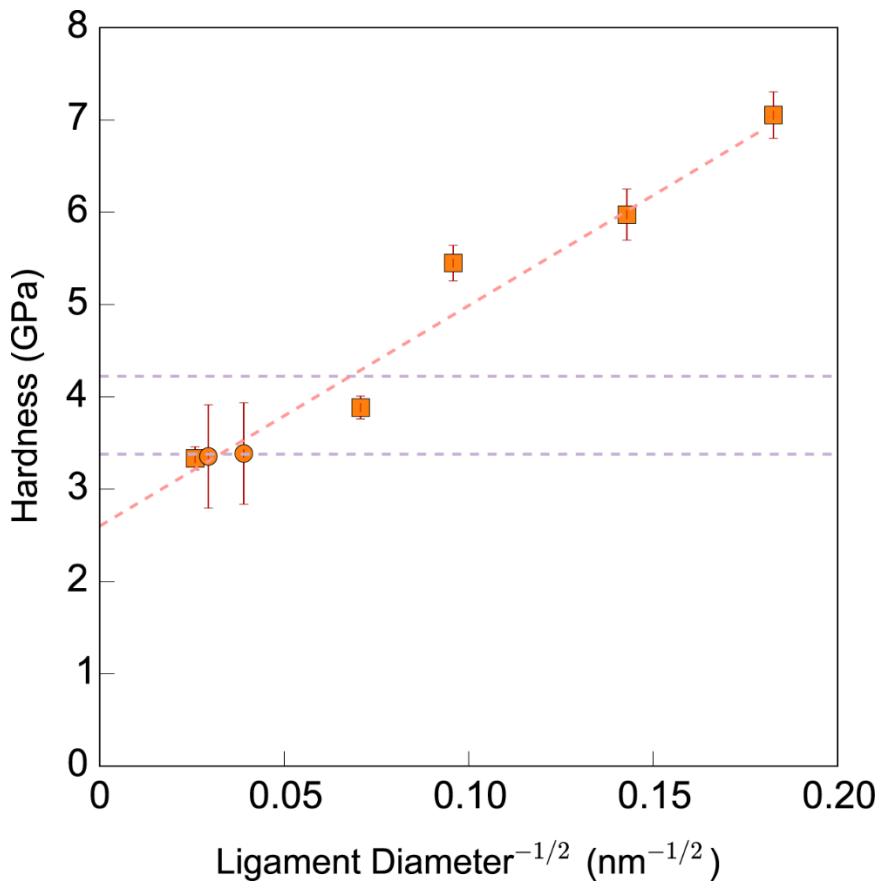

Figure 5.13. Hardness versus ligament diameter for W/Cu. Values measured from Vickers microhardness (orange squares), yield strength from macrocompression (orange circles) converted to hardness, Hall-Petch fit (orange dashed), upper and lower bounds rule of mixtures estimates (purple dashed).

Interestingly, and unlike the Ta-Cu composites, we do not observe a significant increase in strength until the ligament size is below ~ 250 nm. A similar trend has been reported in compression and tension experiments on tungsten micro- and nanopillars (*140*). This decreased sensitivity to the sample diameter was attributed to a higher lattice resistance to dislocation motion in W at room temperature and a stronger size dependence should be expected above the critical temperature for W (~760 ^{o}C). This behavior at larger ligament sizes strongly suggests that the refractory phase dominates the mechanical properties of these materials, but further studies varying the ratio of the two phases are necessary before a conclusion can be made.

Despite the fact that W has a higher yield strength than Ta, the W/Cu composites are weaker than Ta/Cu composites of equivalent sizes, Figure 5.5b. This is easily explained by noting that the Ti-W parent alloys only had 25 at.% W whereas the Ti-Ta parent alloys had 35 at.% Ta. If we assume the strength increase is only due to the refractory phase we estimate the yield strength for a W_{35}/Cu_{65} composite with ~70 nm ligaments would be ~2860 MPa, which would place it slightly stronger than the Ta_{35}/Cu_{65} composite with ~70 nm ligaments (~2500 MPa). It is interesting to consider which phase is actually controlling the mechanical properties, but we also need to factor in the morphology (ligament connectedness), the composition of the ligaments (not always pure refractory), and the composition of the Cu phase (anywhere between 70 and ~0 at.% Ti). Controlled studies varying these parameters are forthcoming.

5.4.2.2 TEM and HRTEM Observations

Owing to their nm-scale ligaments and bulk sample size, W/Cu specimens were examined at Tohoku University by Eric Xu and Professor Chen using Transmission Electron Microscopy (TEM). The primary goal was to better understand the structure of our composites, however we were particularly interested in the Ti concentration across the W/Cu interface given the results from Chapters 3 and 4.

Figure 5.14a-c shows a TEM micrograph of a W/Cu composite with ~50-100 nm ligaments and Figure 5.14d-g are elemental maps of the enclosed region, and Figure 5.14h is a color EELS map highlighting the Ti concentration. Similar to the EDS mapping we performed for Ta/Cu composites in Chapter 3, the W and Cu phases are distinctly separate. This is expected because the two elements are immiscible, but the TEM elemental mapping demonstrates the interface is very sharp and appears to only be several nm wide. Additionally, due to the slow diffusion kinetics in this system the Ti concentration is quite high. This is beneficial because according to Table 5.5 the Cu phase becomes stronger with increasing Ti concentration.

It is also possible the Ti concentration can improve the quality of the interface between the W and Cu phases. Simulation work by our collaborators (not shown), which mirrored the morphology work in Chapter 3, reported a dramatic decrease in the Ti concentration at the interface from the Cu phase (high) to the refractory phase (low). During dealloying, Ti atoms are dissolved locally, leading to a very low concentration in the W phase and a high concentration in the Cu phase. In order to compare theory to experiments we prepared a W/Cu sample for atom probe tomography, Figure 5.15. As expected the Ti concentration is higher in the Cu phase although the concentration difference is marginal. Nevertheless, we can also confirm that the interface between the two phases is quite small, ~3 nm wide.

Finally, high-resolution TEM (HR-TEM) was also performed to study the quality of the interface between the two phases, which has been shown to be incredibly important for the mechanical properties of multilayer materials (*139*, *141–143*). HR-TEM micrographs in Figure 5.16a-h show that the interface between the two immiscible phases is semi-coherent. This is not observed in fcc/bcc multilayer materials, such as Cu/Nb, where there are periodic misfit dislocations between the two phases to account for the different crystal structures. The difference between the composites here and multilayer materials is how they are fabricated. Multilayer materials are sputtered or evaporated (gas-to-solid growth) whereas the composite materials in this work are solidified (liquid-to-solid growth) (*132*). This potentially allows for a more benign crystallization, and thus a more coherent interface between the two phases. It can be seen in the Fourier transforms in Figure 5.16c-h that the fcc Cu phase adopts an orientation that matches closest with the W ligament's crystal orientation. We did not perform any TEM on deformed structures and are not able to comment whether this coherency aids in plasticity across the layers or if dislocation activity is confined to each respective phase.

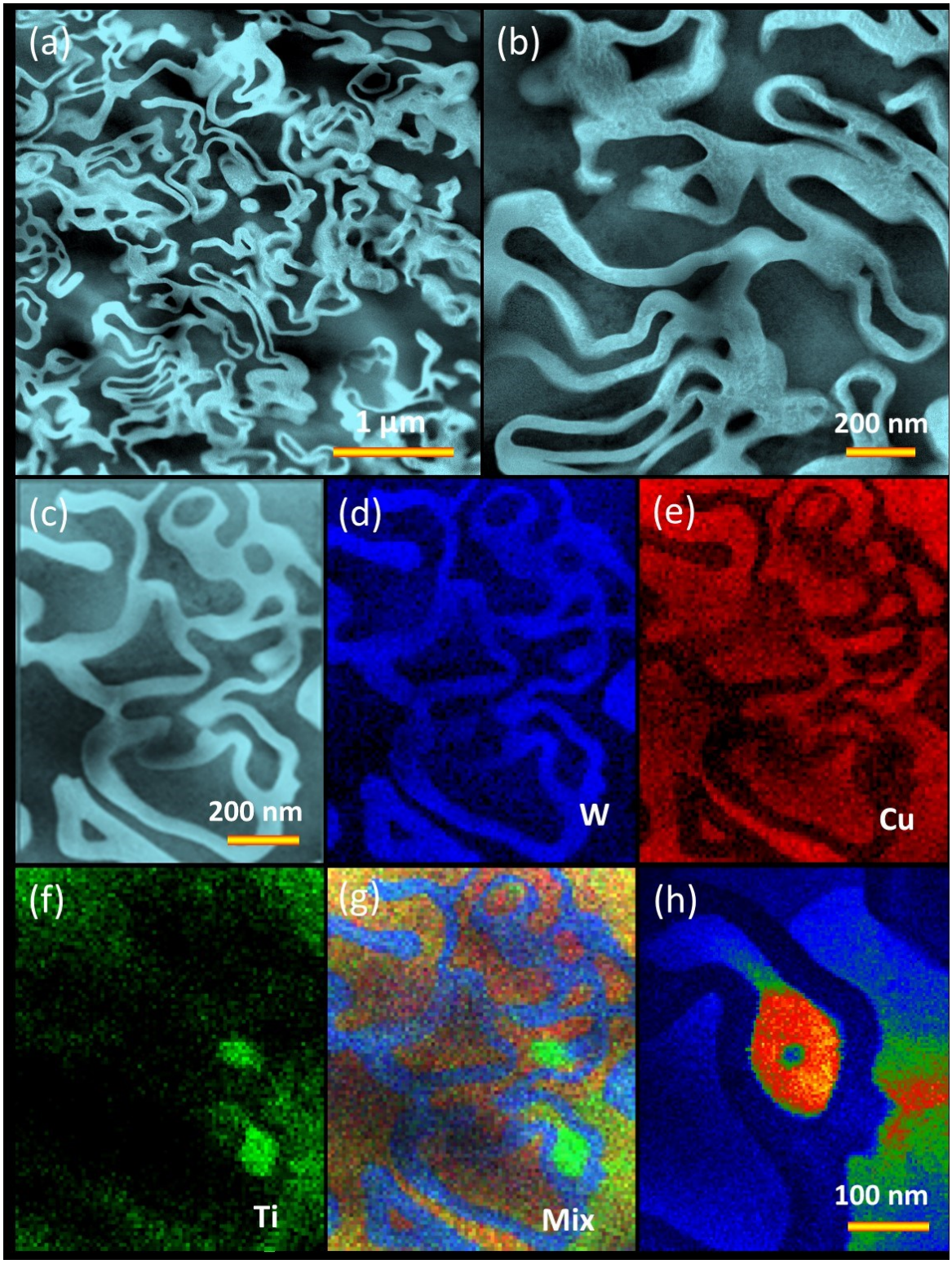

Figure 5.14. (a-c) HAADF STEM of W/Cu composite. (d-g) EDS mapping of region (c). (h) Color EELS map showing concentration variation centered at a Ti-rich phase.

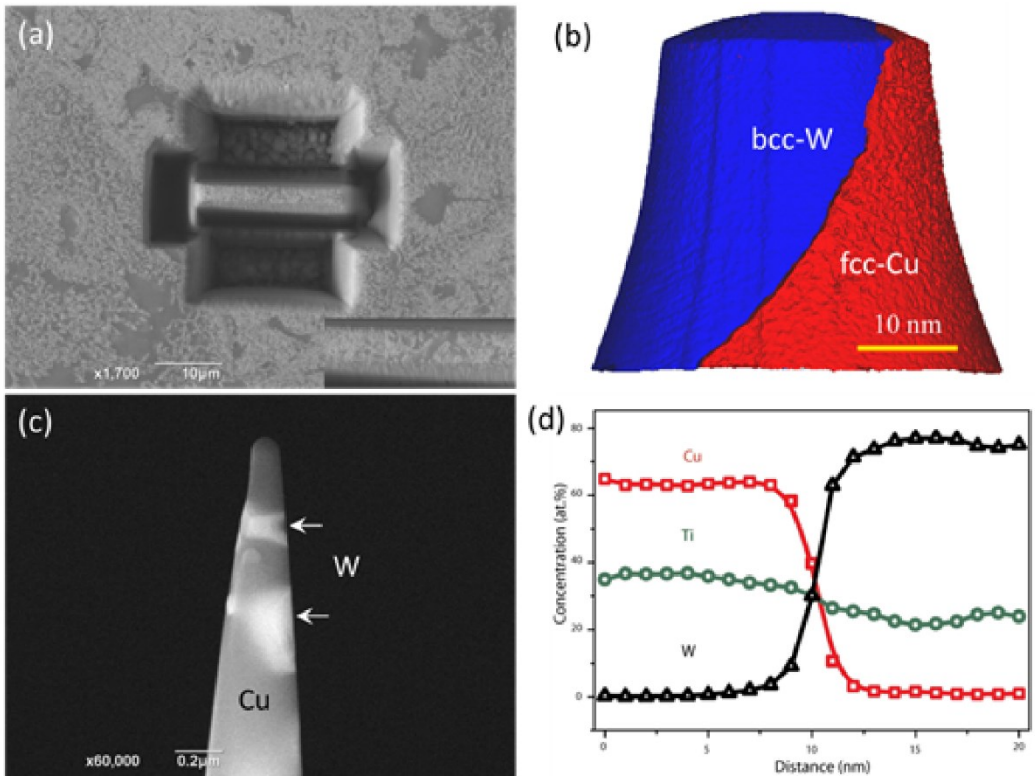

Figure 5.15. (a) FIB liftout of the ROI and shaped to needle (c) for atom probe tomography (APT). (b) The reconstructed APT. (d) Line concentration profile across interface showing a sharp change between the W and Cu phases.

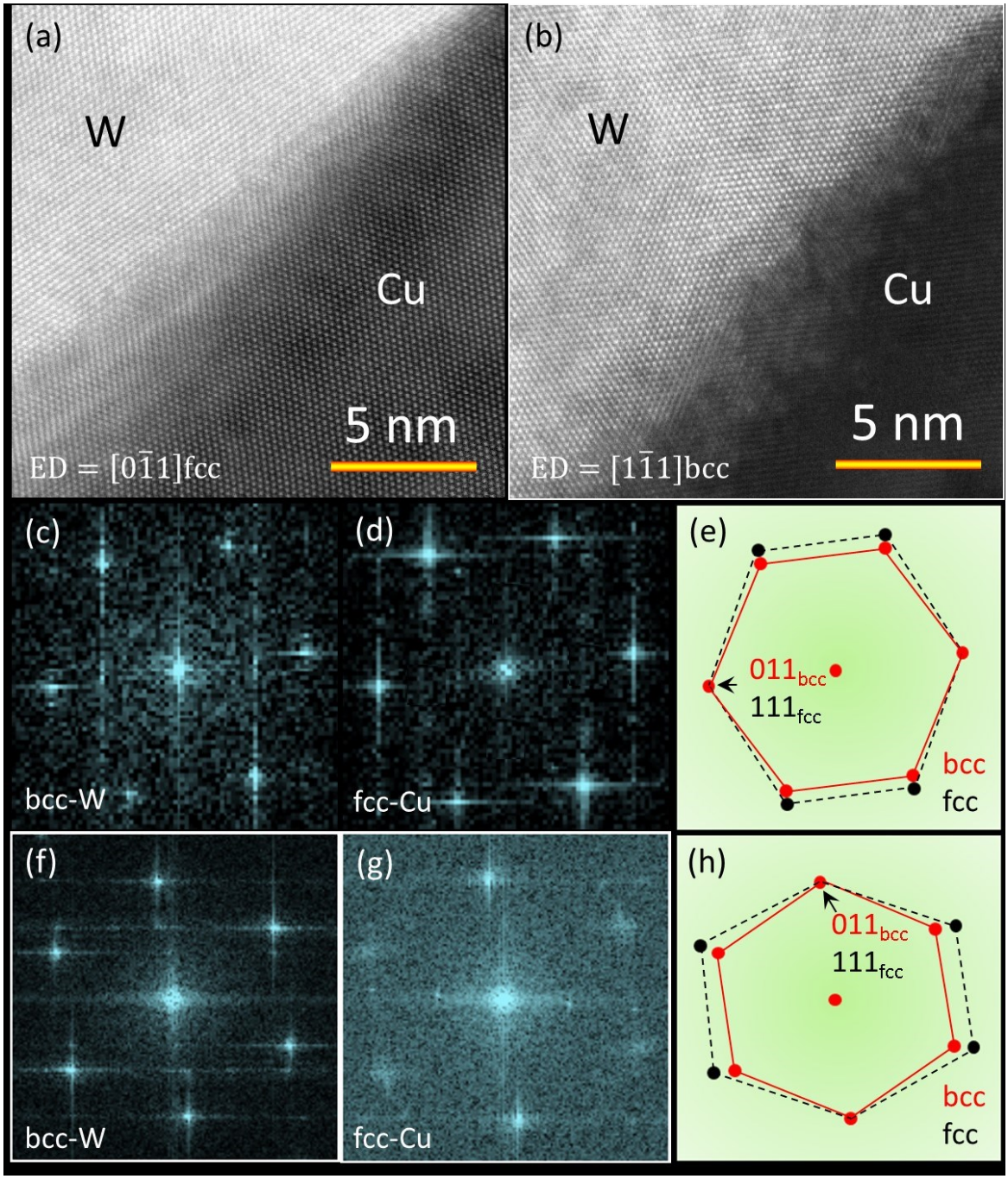

Figure 5.16. Unfiltered HR-STEM images of the two phases, each phase were aligned along electron beam directions. The K-S orientation relationship can be obtained

5.5 Summary and Conclusions

In this chapter we examined the mechanical properties of nanoporous metals and bicontinuous composites. We showed that nanoporous metals have size-dependent strengthening, but are weaker than expected because they are high-density metallic foams. This challenge was overcome by creating fully-dense composite materials using liquid metal dealloying. This work focused on Ta/Cu and W/Cu composites, but the results presented here can extend to other liquid metal dealloying systems. We attempted to qualitatively explain this by presenting a modified Taylor-strengthening law which included size-dependent terms for truncated dislocation sources and dislocation densities. However, there is still significant work left to be done before we can fully understand the underlying mechanisms in these materials. Careful preparation of the Cu phase is necessary (grain size, volume fraction and size of CuTi precipitates) in order to correctly report the size-dependent strengthening in these materials.

This chapter points the way to improvements in the mechanical properties of metals through the design of bulk three-dimensional bicontinuous nancomposites, and these materials will likely find many applications in structural applications that require high strength, ductility, and high density of internal interfaces. The results presented in this chapter have been published in (*45*).

Chapter 6 Conclusions and Future work

At the start of this thesis dealloying was limited to the fabrication of six relatively noble metals (Ag, Au, Ni, Cu, Pt, and Pd), and the majority of studies focused on fabrication and the physical properties of these nanoporous materials. Now, nearly every industrially relevant metal can be made into a porous form factor using a dealloying process, Figure 6.1. This is largely due to the innovation of liquid metal dealloying. We did not touch upon the possibility of using

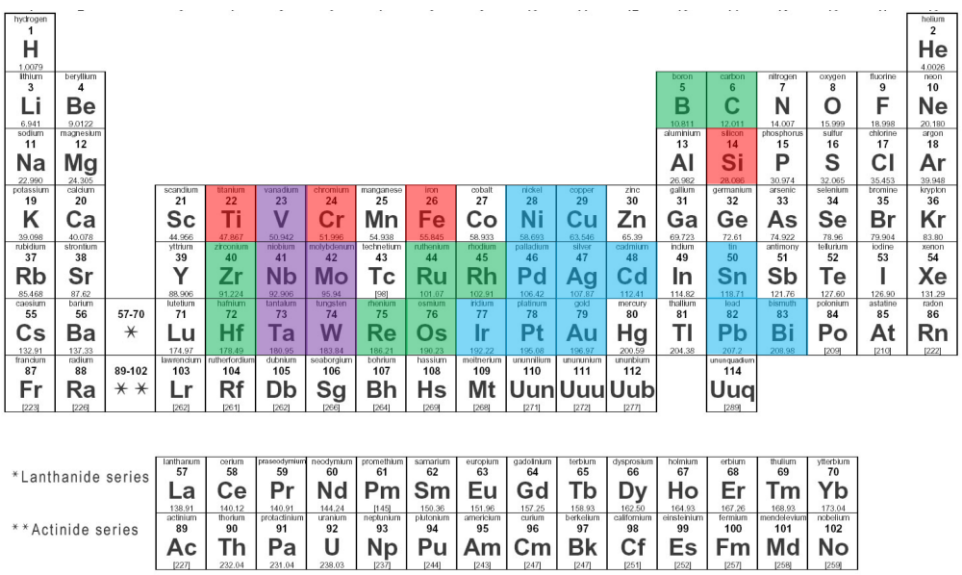

Figure 6.1. Periodic table comparing the outlook of nanoporous metals made by dealloying at the time of this thesis. (blue) Elements which have been successfully made porous via electrochemical dealloying. (red) Elements which have been successfully made porous via liquid metal dealloying by Kato and coworkers. (purple) Elements which can be made porous via liquid metal dealloying using the Ti-X dealloying system in this work. (green) Other possible elements which can be made using other liquid metal dealloying systems.

molten salts, however it is likely other elements not listed and new systems of elements currently listed can be dealloyed using this technique.

The underlying motive of this work was to study the limits of dealloying and explore the kinetics involved during pattern formation. Traditionally, work on dealloying is focused on kinetics of the dissolving species, but the kinetics of the remaining species heavily influences the properties and morphology of the final material; for example, the surface diffusivity of the remaining species during dealloying dictates the length scale of the ligaments and pores. Focusing on this concept we studied nanoparticle systems where the surface diffusion rate is increased due to higher local curvatures, and dealloying of refractory systems where the surface diffusion rate is much lower due to their high melting points. In addition, we studied the mechanical properties of refractory-based composite materials.

It is important to remember that a dealloyed structure is metastable and will always undergo coarsening to decrease its surface area. In fact, every dealloyed structure we experimentally observe is a coarsened structure. For the case of np-Au it has been numerically calculated that the initial roughening of the surface is ~ 1 nm, but observations of dealloyed films show ~ 10 nm ligaments, and bulk dealloyed samples (~ 1 mm^3) show ~ 30 nm ligaments. As the electrolyte penetrates deeper into the alloy, the previously dealloyed structure will coarsen until the electrolyte is rinsed out. It follows that surface diffusion is the most important parameter in dealloyed materials because it dictates the feature size as well as the ability, or limit, of how large a sample can be made using a dealloyed technique.

During electrochemical dealloying, the critical potential represents the point where the dissolution rate becomes comparable to the surface diffusion rate. The surface diffusivity has been observed to change in different electrolyte solutions, and other tricks to control it have

been developed such as adding ternary components to the alloy to increase or decrease this rate. We showed that the surface diffusion rate can change significantly in finite systems where local curvatures, and thus local chemical potentials, dominate. Surface fluctuations become short lived as the particle size decreases, and the critical potential needed to increase in order to dealloy a system over this slower time period.

When attempting to fabricate a porous refractory material via dealloying we observed that the surface diffusivity was too low to produce a coherent structure. Turning to the idea of the homologous temperature, the reaction temperature necessary to produce np-Ta would ~ 400 ^{o}C. We were able to achieve this by developing our own variation of liquid metal dealloying. Immersing Ti-rich refractory alloys into baths of Cu/Ag/Bi, we can span a dealloying temperature range of 400 - 1600 ^{o}C, and fabricate ligaments across the range of 30 nm - 10 μm. It may be possible to fabricate Ta with 10 nm ligaments, but the homologous temperature is only a rough guideline; due to coarsening it is not accurate to claim a specific ligament size for a given homologous temperature, and the reported trend is only for structures that were coarsened for extended periods of time.

From a superficial standpoint, liquid metal dealloying is identical to electrochemical dealloying: a component is selectively dissolved while the other is allowed to remain and diffuse along the metal/liquid interface. However, there are several key differences. First, the characteristic morphology of electrochemically dealloyed materials is no longer present; depending on the alloy composition, LMD can be used to produce droplets, lamellae, partially connected structures, and fully connected structures. In full disclosure, we are not certain if we can call any of these dealloyed structures bicontinuous. Possibly owing to the bcc lattice – which has fewer nearest neighbor diffusion pathways – we observed significant amounts of

enclosed regions that are the results of inverse Rayleigh instabilities; future work will need to address the topologies in these different structures. Second, the rate limiting step during LMD is diffusion of the dissolving component away from the interface. In electrochemical dealloying it has been extensively shown that the dissolution of a high coordinated site such as a terrace atom is the rate-limiting behavior. Unlike liquid metal dealloying, once an atom is dissolved it is rapidly transported away into the electrolyte solution. Third, the parting limit appears to be much lower in LMD. Geometrically, the parting limit is considered to be the space necessary for a surface atom to be complexed by ions in solution. Atoms in a liquid metals are less "clunky" than metal-anion complexes and it is reasonable to expect the parting to be lower. These differences lead to interesting implications for LMD. Because dissolution is not rate-limiting the dealloying velocity is very fast, however it decays with time following $\sim t^{-1/2}$ relationship. Electrochemical dealloying of bulk Ag-Au samples (~1 mm^3) can take several hours, or days, whereas LMD can accomplish this in several minutes. This is partially due to significantly higher temperatures, but the different mechanism is the primary reason.

After we sufficiently understood how to dealloy refractory-based alloys we chose to focus on the mechanical properties of these materials. The mechanical behavior of np-metals has been extensively studied due to their unique form factor (a self-assembled bulk nanostructure), but little work has been done to effectively explain the origin of the strength of these materials. Compiling all of the current mechanical data we plotted the yield strength (mostly converted from hardness values) versus ligament size. Unfortunately there was significant scatter sample-to-sample, but this was understood by considering np-metals to be foams which have reduced strengths and moduli from their bulk counterparts. After normalizing the materials by their relative densities the data collapsed and an obvious size-

dependence appeared. The size-dependent strengthening was similar to single crystal micropillars, however it is important to emphasize that the raw yield strength data have generally low values. In order to fully utilize the strength effect from these small-scale ligaments the void space needs to be filled with a secondary phase.

Serendipitously, a secondary phase infiltrates the porous material during liquid metal dealloying. These composite materials were quite strong, showing increasing strength with decreasing ligament size but we believe the more interesting feature of these materials are their high interfacial area and interconnected structure. It has been shown that materials with high interfacial areas are excellent candidates for radiation-damage tolerance. The high surface area acts as a large sink for defects, and the inherent tortuosity of the composite should lead to a relatively high toughness; the curvature requires a propagating crack to change its path frequently, making failure difficult.

Looking towards the future of these materials, one of the largest challenges remaining in the field of nanoporous metals made via dealloying is controlling coarsening that can occur while the remainder of the material is being dealloyed. As shown in Chapter 4 this is extremely important for liquid metal dealloying systems: the ligament size at the dealloying interface is ~ 80 nm, however the structure coarsens to ~ 1 μm in one second. Coarsening can also play a role in the grain boundary structure, leading to weaker, detached structures at longer coarsening times. There have been many recent papers on adding ternary components to suppress coarsening from several research groups and we believe a solution to this issue is coming soon (*107*, *144–146*). Nevertheless, this work points towards the fabrication of new materials and a new class of composite materials, all of which show promising results.

Appendix A

A.1 Table of Mechanical Data

Table A.1. Yield strength values adapted from literature values of nanoporous gold.

Relative Density	Ligament Diameter (nm)	Yield strength (MPa)*	Test	Ref
0.2	20	24	Hardness	(*46*)
0.25	10	62	Hardness	-
0.25	30	19	Hardness	-
0.25	50	14	Hardness	-
0.3	40	32	Hardness	-
0.3	50	28	Hardness	-
0.3	60	25	Hardness	-
0.3	60	21	Hardness	-
0.3	160	15	Hardness	-
0.3	480	9	Hardness	-
0.3	900	6	Hardness	-
0.3	50	72	Hardness	-
0.33	40	83	Hardness	-
0.35	100	69	Hardness	-
0.35	19.3	37	Hardness	(*66*)
0.42	19	64	Hardness	-
0.42	19	87	Hardness	-
0.2675	20	19	Hardness	(*56*)
0.2675	27.5	14	Hardness	-
0.2675	35	14	Hardness	-
0.2675	40	12	Hardness	-
0.2675	50	9	Hardness	-
0.2675	55	10	Hardness	-
0.2675	70	8	Hardness	-
0.2675	250	3	Hardness	-
0.4	5	373	Hardness	(*118*)
0.4	29	279	Hardness	-
0.4	126	196	Hardness	-
0.25	10	65	Hardness	(*47*)
0.25	25	20	Hardness	-
0.25	50	12	Hardness	-
0.42	100	55	Hardness	-
0.36	15	30	Hardness	(*51*)
0.36	13	38	Hardness	-
0.36	14	50	Hardness	-

0.359	32	42	Hardness	(*69*)
0.35	59	40	Hardness	(*66*)
0.35	56	41	Hardness	-
0.35	75	34	Hardness	-
0.35	58	47	Hardness	-
0.35	55	47	Hardness	-
0.35	95	30	Hardness	-
0.35	60	50	Hardness	-
0.35	60	26	Hardness	-
0.35	198	19	Hardness	-
0.275	15	27	Compression	(*56*)
0.26	55	8	Compression	-
0.33	15	100	Compression	(*57*)
0.3	40	40	Compression	(*47*)
0.3	23	16	Compression	(*58*)
0.33	59.45	22	Tension	(*61*)
0.33	32.8	27	Tension	-
0.3	23	12	Tension	(*58*)
0.352	32	65	Tension	(*69*)
0.25	1.8	175	Simulation	(*62*)
0.25	1.8	25	Simulation	-
0.24	3.26	130	Simulation	(*71*)
0.27	3.26	137	Simulation	-
0.3	3.26	161	Simulation	-
0.33	3.26	174	Simulation	-
0.36	3.26	235	Simulation	-
0.297	3.16	18.2	Simulation	(*63*)

*yield strength for hardness data was estimated using the relationship $\sigma_y = H/2.65$

"-" indicates data is from the same the reference above it

Appendix B

B.1 Concentration Profile

Consider an isothermal system containing an infinite liquid bath of Cu (concentration $c_{-\infty}^{Ti}$) and a semi-infinite block of Ti-Ta (concentration c_S^{Ti}) where $s(t)$ is the interface between the two phases and $s(0)=0$. When $t>0$, the Cu phase dissolves Ti from the TiTa alloy, moving the interface in the positive x direction. We assume diffusion in the solid is frozen so c_S^{Ti} is constant for all t. We also assume this process is near equilibrium and is constant for a given Ti-Ta composition for all t.

There are two possible boundary conditions for the liquid phase: first, the bath is much larger than the sample so the concentration of the liquid does not change over time and is always its initial value $c(-\infty,t)=c_{-\infty}^{Ti}$ ($c_{-\infty}^{Ti}=0$ corresponds to a bath of pure Cu, but the Cu-Ti phase diagram indicates the bath could reasonably be any Cu_xTi_{1-x} concentration where $x \geq 30$ at.%); second, $c(x=0,t)=c_{-\infty}^{Ti}$, which accounts for electromagnetic mixing from the RF induction coils pulling Ti away from the edge of the sample.

Summarizing our system we have:

Solid, $s(t)<x$

$c(x,t)=c_S^{Ti}$

Liquid, $-\infty \leq x < s(t)$

$c(-\infty,t)=c_{-\infty}^{Ti}$, or $c(x=0,t)=c_{-\infty}^{Ti}$

Boundary, $x=s(t)$

$s(0)=0$

$$c\left(s\left(t\right),t\right)=c_L^{Ti}. \tag{B.1}$$

In order to solve for $c\left(x,t\right)$ we rescale the problem using the substitution $\eta \equiv \frac{x}{2\sqrt{D_L t}}$ and define a function $F\left(\eta\left(x,t\right)\right)\equiv c\left(x,t\right)$. Eq. (4.1) becomes:

$$\frac{x}{\sqrt{D_L t}}\frac{dF}{d\eta}+\frac{d^2F}{d\eta^2}=0 \tag{B.2}$$

with the solution

$$F\left(\eta\right)=\frac{C_1\sqrt{\pi}}{2}erf\left(\eta\right)+C_2$$

$$c\left(x,t\right)=F\left(\frac{x}{2\sqrt{D_L t}}\right)=\frac{C_1\sqrt{\pi}}{2}erf\left(\frac{x}{2\sqrt{D_L t}}\right)+C_2. \tag{B.3}$$

Using our boundary conditions from Eq. (B.1) and the solution from Eq. (B.3) we have two possible solutions depending on the liquid phase boundary condition:

$$c\left(x,t\right)=\frac{c_L^{Ti}-c_{-\infty}^{Ti}}{\left(1+erf\left(\frac{s\left(t\right)}{2\sqrt{D_L t}}\right)\right)}erf\left(\frac{x}{2\sqrt{D_L t}}\right)+\frac{c_L^{Ti}-c_{-\infty}^{Ti}}{\left(1+erf\left(\frac{s\left(t\right)}{2\sqrt{D_L t}}\right)\right)} \tag{B.4}$$

$$c\left(x,t\right)=\frac{c_L^{Ti}-c_{-\infty}^{Ti}}{erf\left(\frac{s\left(t\right)}{2\sqrt{D_L t}}\right)}erf\left(\frac{x}{2\sqrt{D_L t}}\right)+c_{-\infty}^{Ti} \tag{B.5}$$

Figure 4.4 compares the raw data along with fits for Eqs. (B.4) and (B.5) using a literature value for the diffusivity of Ti in molten Cu, $D_{Ti\to Cu}(1240\,^{\circ}C)$, $7.0\times10^{-5}\ cm^2s^{-1}$. It is readily apparent that the best fit is Eq. (B.5), which assumes that the edge of the sample will always have the same Ti concentration as the liquid, i.e. $c\left(x=0,t\right)=c_{-\infty}^{Ti}$. This is a reasonable

assumption because induction melting induces eddy currents, which add convection to system.

We can further simplify Eq. (B.5) by defining a variable $\lambda \equiv \frac{s(t)}{2\sqrt{D_L t}}$, yielding:

$$c(x,t) = \frac{c_L^{Ti} - c_{-\infty}^{Ti}}{erf(\lambda)} erf\left(\frac{x}{2\sqrt{D_L t}}\right) + c_{-\infty}^{Ti}. \tag{B.6}$$

Eq. (B.6) is the final form for the concentration in the liquid phase. λ can be solved numerically by fitting Eq. (B.6) to experimental data or analytically using the derivation in Appendix A.2.

B.2 Dealloying Depth

We can use Eq. (4.2) to derive a relationship for the dealloying depth. First we define the time derivative of the interface:

$$\frac{ds}{dt} = \frac{\lambda\sqrt{D_L}}{\sqrt{t}} \tag{B.7}$$

and the spatial derivative of Eq. (B.6) is given by

$$\frac{\partial c}{\partial x}\left(s(t),t\right) = \frac{c_L^{Ti} - c_{-\infty}^{Ti}}{erf(\lambda)}\left(\frac{e^{-x^2/4Dt}}{\sqrt{\pi D_L t}}\right) = \frac{c_L^{Ti} - c_{-\infty}^{Ti}}{erf(\lambda)}\left(\frac{e^{-\lambda^2}}{\sqrt{\pi D_L t}}\right). \tag{B.8}$$

Eq. (4.2) becomes

$$\frac{ds}{dt}\left(c_S^{Ti} - c_L^{Ti}\right) = \frac{\lambda\sqrt{D_L}}{\sqrt{t}}\left(c_S^{Ti} - c_L^{Ti}\right) = D_L \frac{\partial c}{\partial x}\left(s(t),t\right) = \frac{D_L(c_L^{Ti} - c_{-\infty}^{Ti})}{erf(\lambda)}\left(\frac{e^{-\lambda^2}}{\sqrt{\pi D_L t}}\right) \tag{B.9}$$

and the analytical solution for λ is

$$\lambda\left(erf(\lambda)\right)e^{\lambda^2} = \frac{c_L^{Ti} - c_{-\infty}^{Ti}}{\sqrt{\pi}\left(c_S^{Ti} - c_L^{Ti}\right)}. \tag{B.10}$$

We determined λ for each composition using Eq. (B.10) and the values for c_L^{Ti} and c_S^{Ti}, which were measured using EDS, and these values can be found in Table 4.1. Now that we have solved for λ we can explicitly write the expression for the interface

$$s(t) = \sqrt{4\lambda^2 D_L t} \,. \tag{B.11}$$

Appendix C

C.1 Complete Compression Data and DIC Analysis

Digital image correlation was used to determine the engineering strain in the compression and tensile testing (*130*). The samples did not need any surface patterning because the recast layer from the EDM provided a textured surface that was easy to track with the DIC software, Figure C.1.

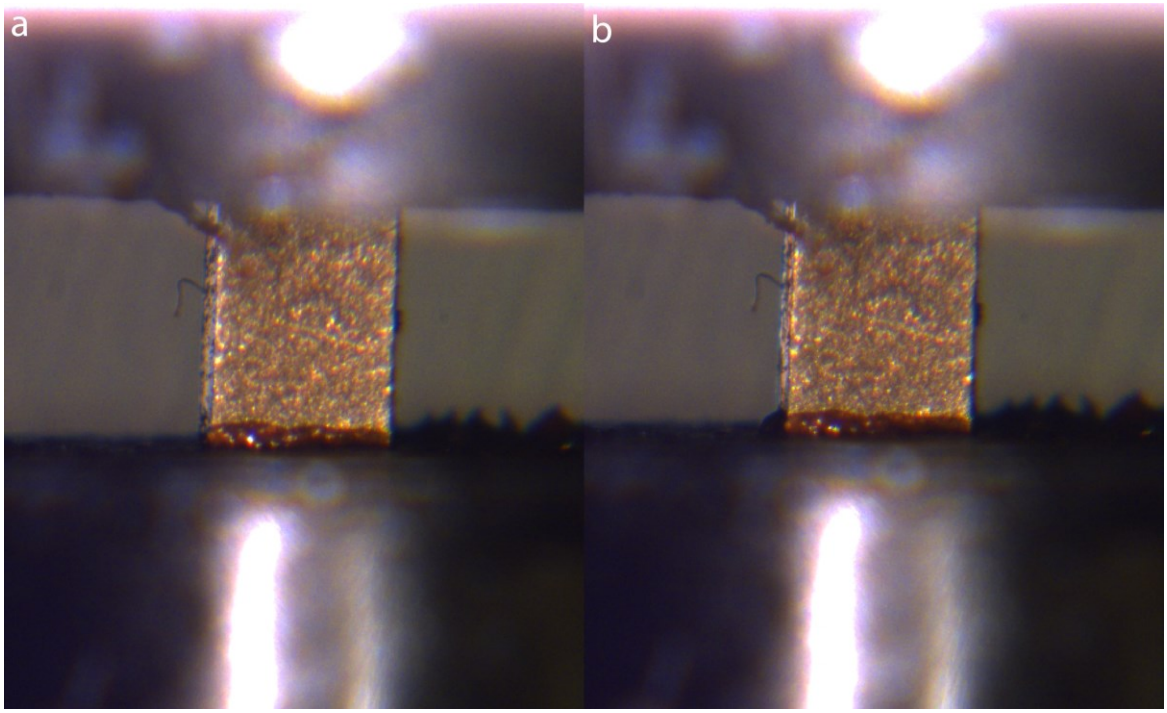

Figure C.1. Ta/Cu sample for compression testing. (a) Initial sample, (b) sample after 200 seconds of deformation, ~ 4 % strain.

The recast layer was measured to only be ~ 10 μm, which contributes a negligible error to the stress measurement for the bulk compression samples. At the beginning stages of this work we tested the reliability of the DIC software and what was the appropriate resolution to accurately track the strain. For the sample shown in Figure C.1 we chose different pixel resolutions for tracking and compared the measurements to those directly measured from the images, Figure

C.2. It can be seen that even for large windows such as 100 x 100 (where only 4 spots on the sample were tracked) the measured values were very close to the high resolutions such as 2 x

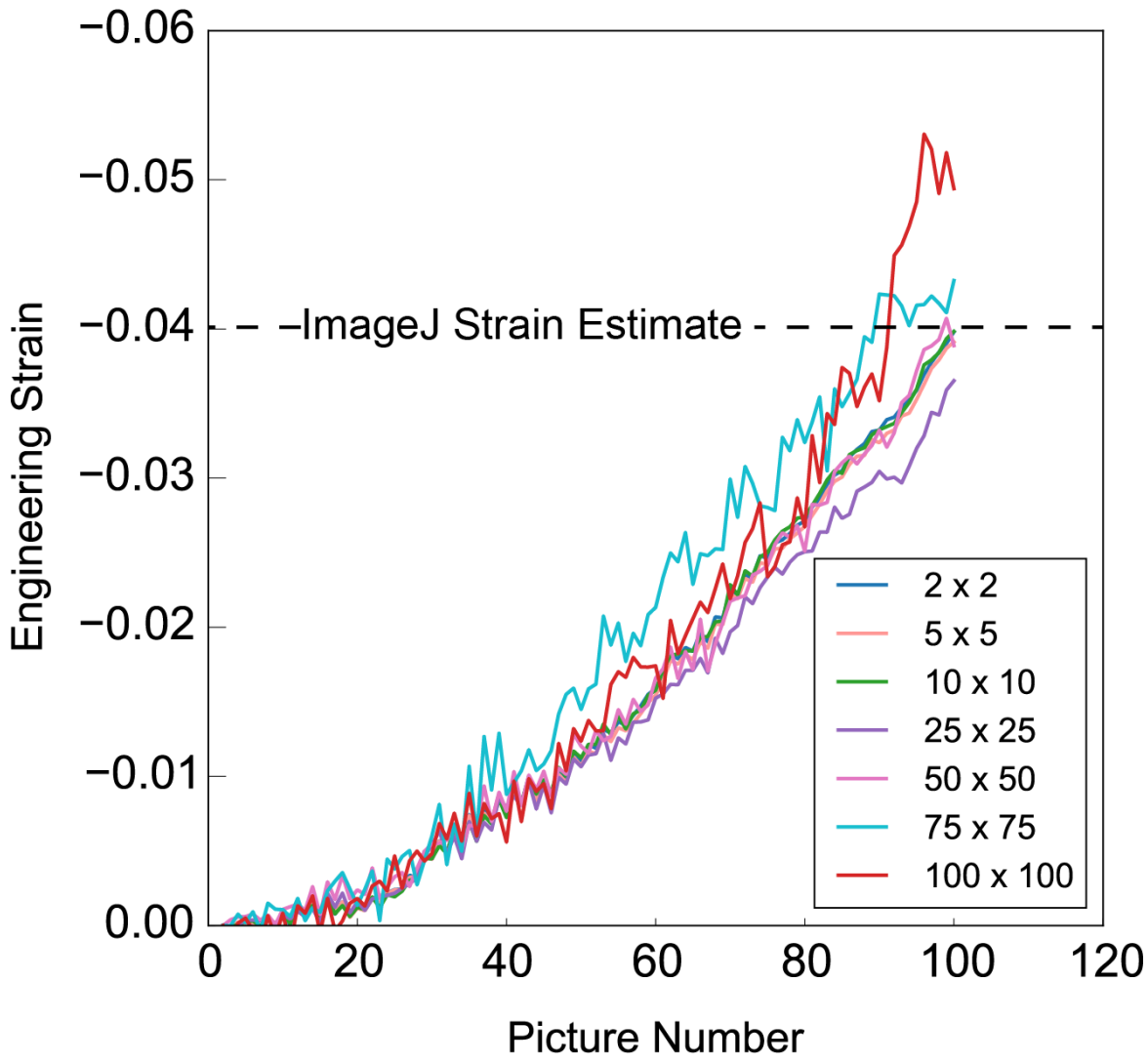

Figure C.2. Engineering stress versus pictures for the first 200 seconds of a Ta/Cu compression test. It can be seen that as the grid gets more refined (changing from a resolution of 100 x 100 to 2 x 2) the values converge and the oscillations become damped. The ImageJ estimate is the strain difference from picture one and picture one hundred.

2. The major observable difference is the estimated strain value dampens and becomes smooth with increasing resolution. Ideally, we would use the maximum resolution, 1 x 1, but the computation time increases with increasing resolution and the analysis becomes labor

intensive. For the majority of tests we used a 10 x 10 resolution, and occasionally cross-checked the measurements with ImageJ and higher resolution runs. The remainder of this

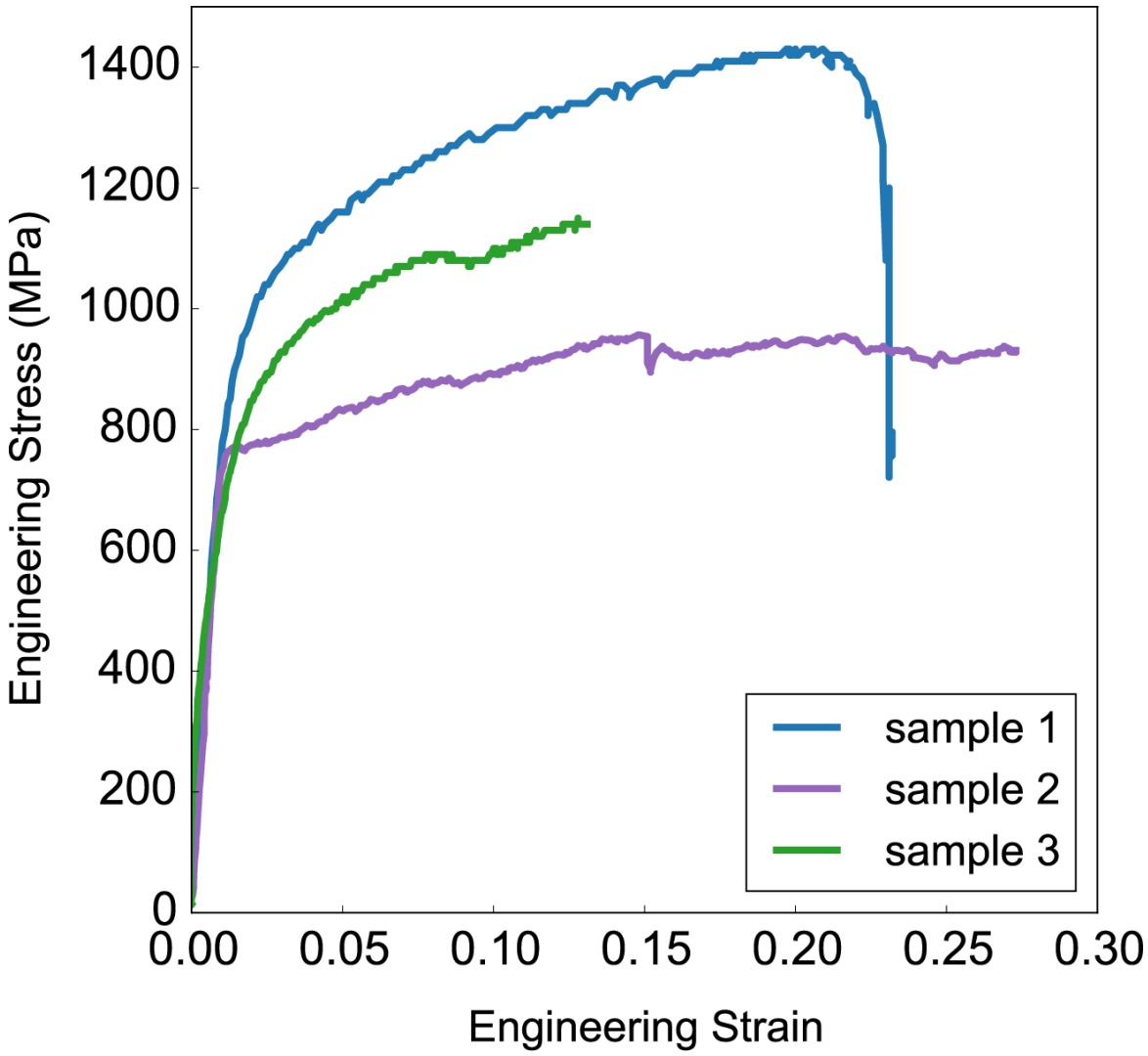

Figure C.3. Engineering stress-strain curves for Ta/Cu composites with 3 μm features.

section includes the compiled stress-strain data from the compression measurements.

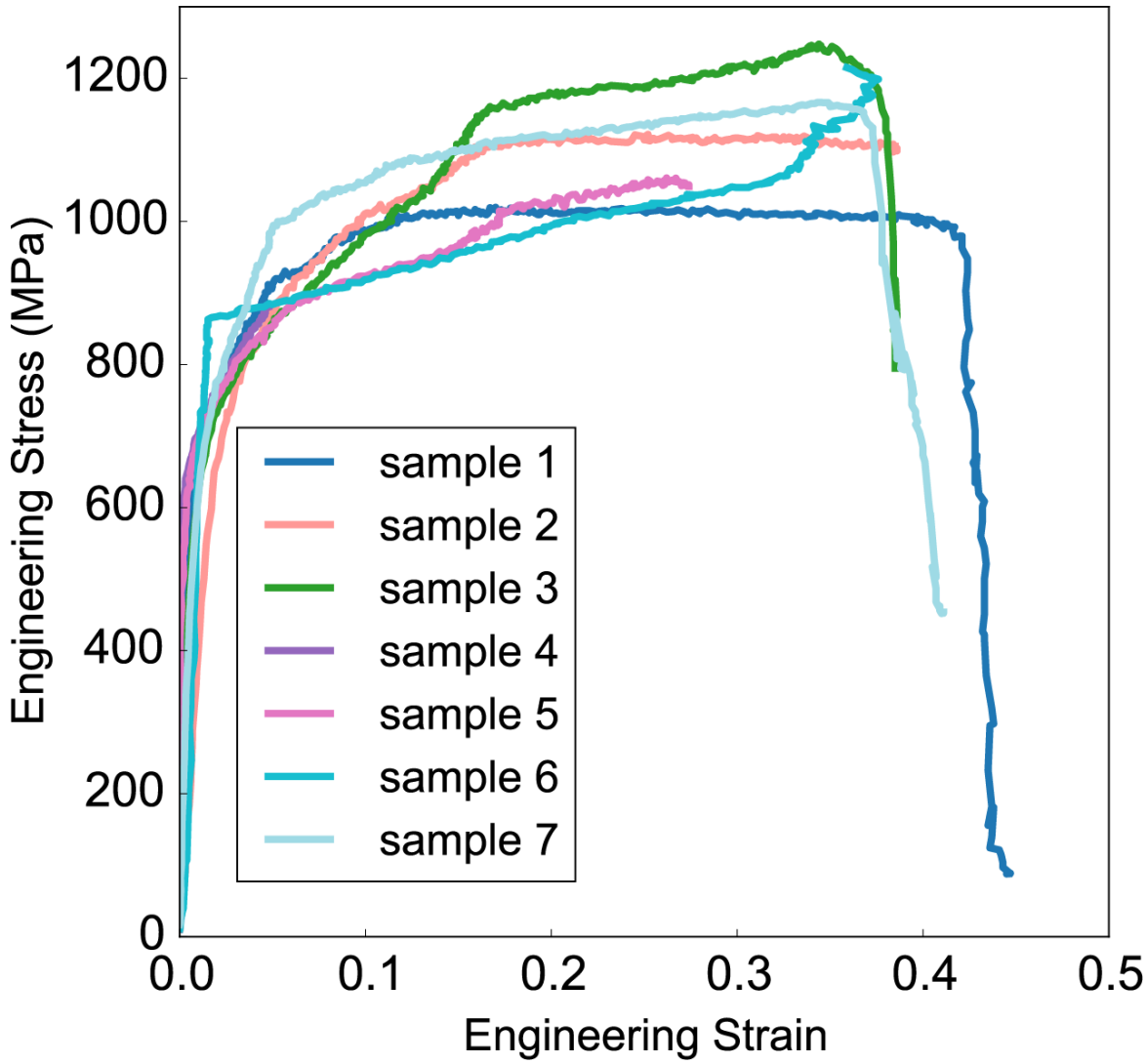

Figure C.4. Engineering stress-strain curves for Ta/Cu composites with 5.2 µm features.

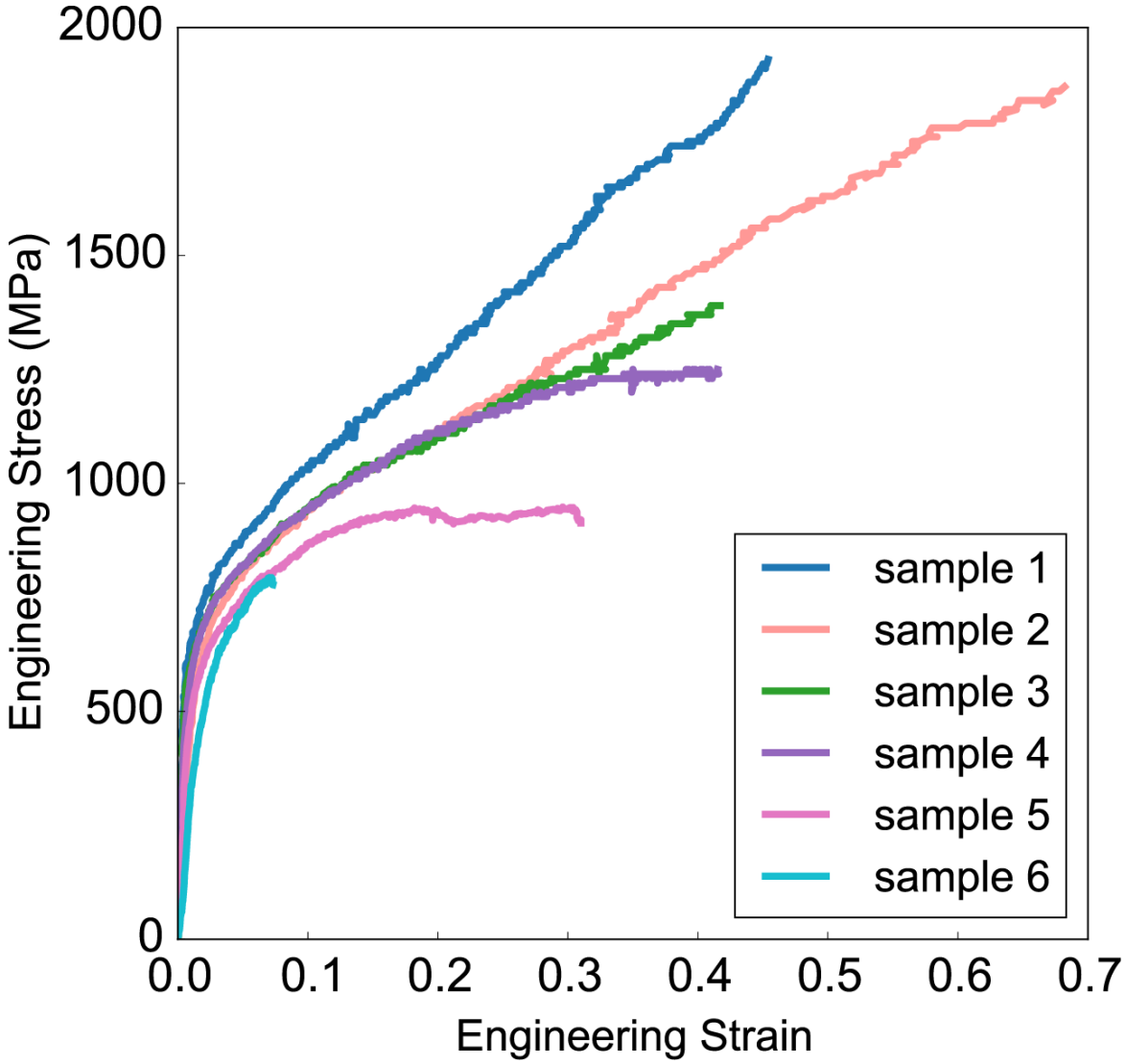

Figure C.5. Engineering stress-strain curves for Ta/Cu composites with 7.6 µm features.

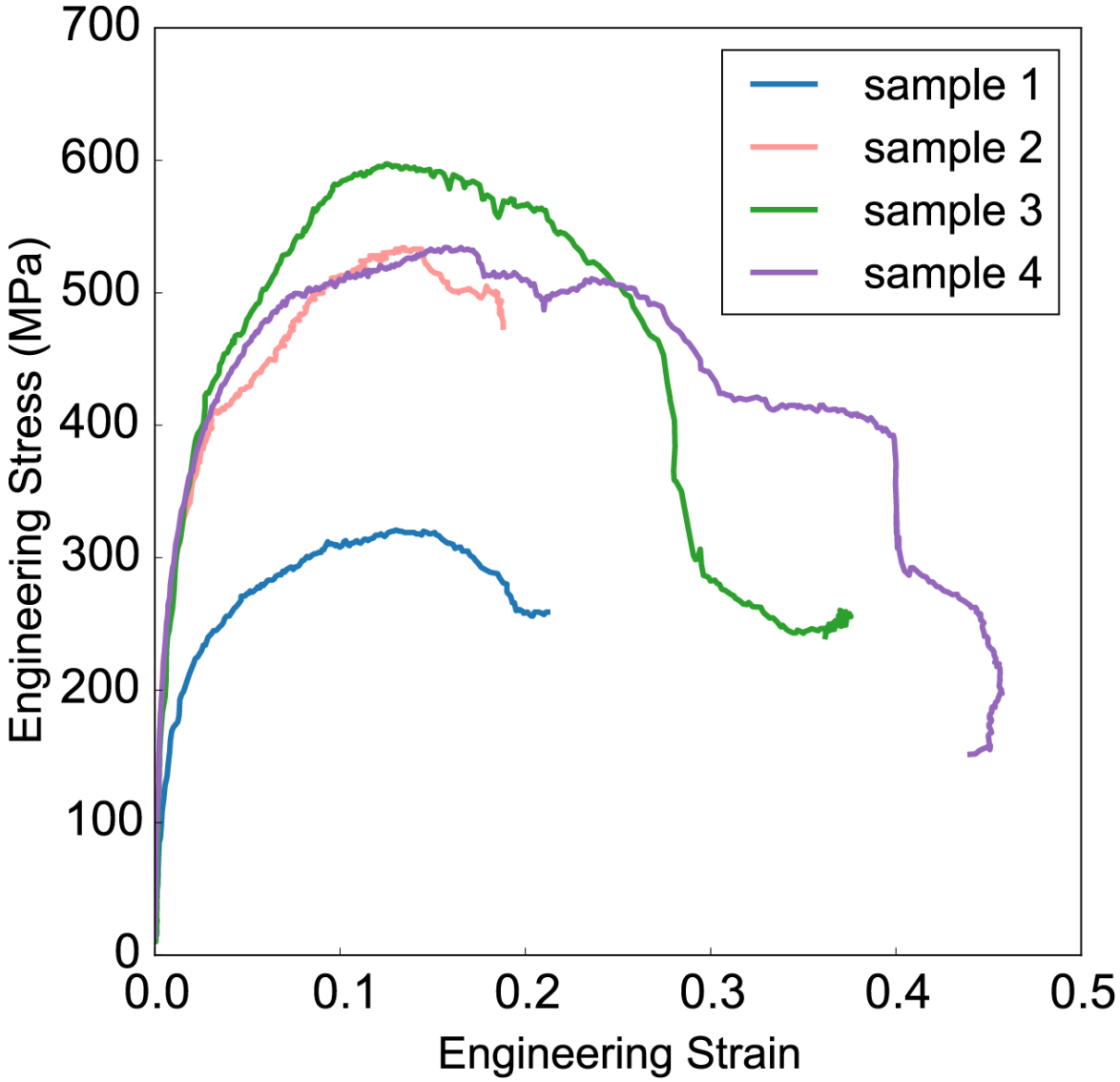

Figure C.6. Engineering stress-strain curves for Ta/Cu composites with 10.5 μm features.

References

1. J. Snyder, K. Livi, J. Erlebacher, Oxygen Reduction Reaction Performance of [MTBD][beti]-Encapsulated Nanoporous NiPt Alloy Nanoparticles. *Adv. Funct. Mater.* **23**, 5494–5501 (2013).

2. K. Hu, D. Lan, X. Li, S. Zhang, Electrochemical DNA Biosensor Based on Nanoporous Gold Electrode and Multifunctional Encoded DNA−Au Bio Bar Codes. *Anal. Chem.* **80**, 9124–9130 (2008).

3. H. Jin, J. Weissmuller, A Material with Electrically Tunable Strength and Flow Stress. *Science (80-.).* **332**, 1179–1182 (2011).

4. J. W. Kim *et al.*, Optimizing niobium dealloying with metallic melt to fabricate porous structure for electrolytic capacitors. *Acta Mater.* **84**, 497–505 (2015).

5. X. Lang, A. Hirata, T. Fujita, M. Chen, Nanoporous metal/oxide hybrid electrodes for electrochemical supercapacitors. *Nat. Nanotechnol.* **6**, 232–236 (2011).

6. Y. Ito *et al.*, High-quality three-dimensional nanoporous graphene. *Angew. Chemie - Int. Ed.* **53**, 4822–4826 (2014).

7. T. Wada *et al.*, Bulk-nanoporous-silicon negative electrode with extremely high cyclability for lithium-ion batteries prepared using a top-down process. *Nano Lett.* **14**, 4505–4510 (2014).

8. J. Erlebacher, M. J. Aziz, a Karma, N. Dimitrov, K. Sieradzki, Evolution of nanoporosity in dealloying. *Nature*. **410**, 450–453 (2001).

9. J. Erlebacher, R. Seshadri, Hard Materials with Tunable Porosity. *MRS Bull.* **34**, 561–568 (2009).

10. K. Sieradzki, Curvature Effects in Alloy Dissolution. *J. Electrochem. Soc.* **140**, 2868 (1993).

11. J. Erlebacher, K. Sieradzki, Pattern formation during dealloying. *Scr. Mater.* **49**, 991–996 (2003).

12. J. Snyder, T. Fujita, M. W. Chen, J. Erlebacher, Oxygen reduction in nanoporous metal-ionic liquid composite electrocatalysts. *Nat. Mater.* **9** (2010), pp. 904–907.

13. F. Kertis *et al.*, Structure/processing relationships in the fabrication of nanoporous gold. *JOM*. **62** (2010), pp. 50–56.

14. H. Lechtman, Pre-Columbian Surface Metallurgy. *Sci. Am.* **250**, 56–63154 (1984).

15. H. W. Pickering, Volume Diffusion During Anodic Dissolution of a Binary Alloy. *J. Electrochem. Soc.* **115**, 143 (1968).

16. A. J. Forty, Corrosion micromorphology of noble metal alloys and depletion gilding. *Nature*. **282** (1979), pp. 597–598.

17. E. Seebauer, Estimating surface diffusion coefficients. *Prog. Surf. Sci.* **49**, 265–330 (1995).

18. J. Rugolo, J. Erlebacher, K. Sieradzki, Length scales in alloy dissolution and measurement of absolute interfacial free energy. *Nat. Mater.* **5**, 946–949 (2006).

19. J. Erlebacher, An Atomistic Description of Dealloying. *J. Electrochem. Soc.* **151**, C614 (2004).

20. J. Snyder, J. Erlebacher, Erratum: Kinetics of Crystal Etching Limited by Terrace Dissolution [J. Electrochem. Soc., 157, C125 (2010)]. *J. Electrochem. Soc.* **157**, S21 (2010).

21. H. W. Pickering, P. J. Byrne, On Preferential Anodic Dissolution of Alloys in the Low-Current Region and the Nature of the Critical Potential. *J. Electrochem. Soc.* **118**, 209 (1971).

22. D. M. Artymowicz, J. Erlebacher, R. C. Newman, Relationship between the parting limit for de-alloying and a particular geometric high-density site percolation threshold. *Philos. Mag.* **89**, 1663–1693 (2009).

23. K. Sieradzki, R. R. Corderman, K. Shukla, R. C. Newman, Computer simulations of corrosion: Selective dissolution of binary alloys. *Philos. Mag. A*. **59**, 713–746 (1989).

24. R. C. Newman, R. R. Corderman, K. Sieradzki, Evidence for dealloying of austenitic stainless steels in simulated stress corrosion crack environments. *Br. Corros. J.* **24**, 143–148 (1989).

25. K. Sieradzki *et al.*, The Dealloying Critical Potential. *J. Electrochem. Soc.* **149**, B370 (2002).

26. A. Dursun, D. V. Pugh, S. G. Corcoran, A Steady-State Method for Determining the Dealloying Critical Potential. *Electrochem. Solid-State Lett.* **6**, B32 (2003).

27. R. Mendoza, K. Thornton, I. Savin, P. W. Voorhees, The evolution of interfacial topology during coarsening. *Acta Mater.* **54**, 743–750 (2006).

28. Y. C. K. Chen-Wiegart *et al.*, In situ imaging of dealloying during nanoporous gold formation by transmission X-ray microscopy. *Acta Mater.* **61**, 1118–1125 (2013).

29. Y. C. K. Chen-Wiegart *et al.*, Structural evolution of nanoporous gold during thermal coarsening. *Acta Mater.* **60**, 4972–4981 (2012).

30. Y. C. K. Chen *et al.*, Morphological and topological analysis of coarsened nanoporous gold by x-ray nanotomography. *Appl. Phys. Lett.* **96**, 213–215 (2010).

31. Y. C. K. Chen-Wiegart, S. Wang, I. McNulty, D. C. Dunand, Effect of Ag-Au composition and acid concentration on dealloying front velocity and cracking during nanoporous gold formation. *Acta Mater.* **61**, 5561–5570 (2013).

32. Y. K. Chen-Wiegart *et al.*, 3D morphological evolution of porous titanium by x-ray micro- and nano-tomography. *J. Mater. Res.* **28**, 2444–2452 (2013).

33. J. Erlebacher, I. McCue, Geometric characterization of nanoporous metals. *Acta Mater.* **60**, 6164–6174 (2012).

34. T. Fujita, L. H. Qian, K. Inoke, J. Erlebacher, M. W. Chen, Three-dimensional morphology of nanoporous gold. *Appl. Phys. Lett.* **92**, 90–93 (2008).

35. J. Erlebacher, Mechanism of coarsening and bubble formation in high-genus nanoporous metals. *Phys. Rev. Lett.* **106**, 1–4 (2011).

36. K. Kolluri, M. J. Demkowicz, Coarsening by network restructuring in model nanoporous gold. *Acta Mater.* **59**, 7645–7653 (2011).

37. L. H. Qian, M. W. Chen, Ultrafine nanoporous gold by low-temperature dealloying and kinetics of nanopore formation. *Appl. Phys. Lett.* **91**, 083105 (2007).

38. H. Rösner, S. Parida, D. Kramer, C. A. Volkert, J. Weissmüller, Reconstructing a Nanoporous Metal in Three Dimensions: An Electron Tomography Study of Dealloyed Gold Leaf. *Adv. Eng. Mater.* **9**, 535–541 (2007).

39. J. . Harrison, C. Wagner, The attack of solid alloys by liquid metals and salt melts. *Acta Metall.* **7**, 722–735 (1959).

40. T. Wada, K. Yubuta, A. Inoue, H. Kato, Dealloying by metallic melt. *Mater. Lett.* **65**, 1076–1078 (2011).

41. M. Tsuda, T. Wada, H. Kato, Kinetics of formation and coarsening of nanoporous ??-titanium dealloyed with Mg melt. *J. Appl. Phys.* **114**, 113503 (2013).

42. T. Wada, H. Kato, Three-dimensional open-cell macroporous iron, chromium and ferritic stainless steel. *Scr. Mater.* **68**, 723–726 (2013).

43. K. Wang, J. Weissmüller, Composites of Nanoporous Gold and Polymer. *Adv. Mater.* **25**, 1280–1284 (2013).

44. K. Wang *et al.*, Nanoporous-gold-based composites: toward tensile ductility. *NPG Asia Mater.* **7**, e187 (2015).

45. I. McCue *et al.*, *Adv. Eng. Mater.*, in press, doi:10.1002/adem.201500219.

46. A. M. Hodge *et al.*, Scaling equation for yield strength of nanoporous open-cell foams. *Acta Mater.* **55**, 1343–1349 (2007).

47. J. Biener *et al.*, Size effects on the mechanical behavior of nanoporous Au. *Nano Lett.* **6**, 2379–2382 (2006).

48. J. Weissmüller, R. C. Newman, H. Jin, A. M. Hodge, J. W. Kysar, Nanoporous Metals by Alloy Corrosion: Formation and Mechanical Properties. *MRS Bull.* **34**, 577–586 (2009).

49. I. C. Cheng, A. M. Hodge, Strength scale behavior of nanoporous Ag, Pd and Cu foams. *Scr. Mater.* **69**, 295–298 (2013).

50. J. Biener, A. M. Hodge, A. V. Hamza, Microscopic failure behavior of nanoporous gold. *Appl. Phys. Lett.* **87**, 1–3 (2005).

51. J. Biener, A. M. Hodge, A. V. Hamza, L. M. Hsiung, J. H. Satcher, Nanoporous Au: A high yield strength material. *J. Appl. Phys.* **97**, 024301–4 (2005).

52. L. a. Zepeda-Ruiz, B. Sadigh, J. Biener, A. M. Hodge, A. V. Hamza, Mechanical response of freestanding Au nanopillars under compression. *Appl. Phys. Lett.* **91**, 101907 (2007).

53. J. R. Hayes, a. M. Hodge, J. Biener, a. V. Hamza, K. Sieradzki, Monolithic nanoporous copper by dealloying Mn–Cu. *J. Mater. Res.* **21**, 2611–2616 (2006).

54. A. Hodge, J. Hayes, J. Caro, J. Biener, A. Hamza, Characterization and Mechanical Behavior of Nanoporous Gold. *Adv. Eng. Mater.* **8**, 853–857 (2006).

55. H.-J. Jin, D. Kramer, Y. Ivanisenko, J. Weissmüller, Macroscopically Strong Nanoporous Pt Prepared by Dealloying. *Adv. Eng. Mater.* **9**, 849–854 (2007).

56. H.-J. Jin *et al.*, Deforming nanoporous metal: Role of lattice coherency. *Acta Mater.* **57**, 2665–2672 (2009).

57. C. a. Volkert, E. T. Lilleodden, D. Kramer, J. Weissmüller, Approaching the theoretical strength in nanoporous Au. *Appl. Phys. Lett.* **89**, 061920 (2006).

58. T. J. Balk, C. Eberl, Y. Sun, K. J. Hemker, D. Gianola, Tensile and Compressive Microspecimen Testing of Bulk Nanoporous Gold. *JOM.* **61**, 26–31 (2009).

59. N. Abdolrahim *et al.*, The mechanical response of core-shell structures for nanoporous metallic materials. *Philos. Mag.* **93**, 736–748 (2012).

60. Y. Sun, J. Ye, A. M. Minor, T. J. Balk, In situ indentation of nanoporous gold thin films in the transmission electron microscope. *Microsc. Res. Tech.* **72**, 232–241 (2009).

61. N. J. Briot, T. Kennerknecht, C. Eberl, T. J. Balk, Mechanical properties of bulk single crystalline nanoporous gold investigated by millimetre-scale tension and compression testing. *Philos. Mag.* **94**, 847–866 (2014).

62. D. Farkas, A. Caro, E. Bringa, D. Crowson, Mechanical response of nanoporous gold. *Acta Mater.* **61**, 3249–3256 (2013).

63. N. D. Bao-Nam *et al.*, Anomalous compliance and early yielding of nanoporous gold. *Acta Mater.* **93**, 144–155 (2015).

64. N. Huber, R. N. Viswanath, N. Mameka, J. Markmann, J. Weissmüller, Scaling laws of nanoporous metals under uniaxial compression. *Acta Mater.* **67**, 252–265 (2014).

65. H. L. Fan, D. N. Fang, Modeling and limits of strength of nanoporous foams. *Mater. Des.* **30**, 1441–1444 (2009).

66. N. J. Briot, thesis, University of Kentucky (2015).

67. R. Dou, B. Derby, Deformation mechanisms in gold nanowires and nanoporous gold. *Philos. Mag.* **91**, 1070–1083 (2011).

68. T. Wada, A. D. Setyawan, K. Yubuta, H. Kato, Nano- to submicro-porous β-Ti alloy prepared from dealloying in a metallic melt. *Scr. Mater.* **65**, 532–535 (2011).

69. D. Lee *et al.*, Microfabrication and mechanical properties of nanoporous gold at the nanoscale. *Scr. Mater.* **56**, 437–440 (2007).

70. L. J. Gibson, M. F. Ashby, *Cellular Solids: Structure and Properties* (Cambridge Univeristy Press, Cambridge, 1997).

71. X.-Y. Sun, G.-K. Xu, X. Li, X.-Q. Feng, H. Gao, Mechanical properties and scaling laws of nanoporous gold. *J. Appl. Phys.* **113**, 023505 (2013).

72. R. Dou, B. Derby, A universal scaling law for the strength of metal micropillars and nanowires. *Scr. Mater.* **61**, 524–527 (2009).

73. J. a. El-Awady, Unravelling the physics of size-dependent dislocation-mediated plasticity. *Nat. Commun.* **6**, 5926 (2015).

74. Q. Yu, R. K. Mishra, J. W. Morris, A. M. Minor, The effect of size on dislocation cell formation and strain hardening in aluminium. *Philos. Mag.* **94**, 2062–2071 (2014).

75. D. M. Norfleet, D. M. Dimiduk, S. J. Polasik, M. D. Uchic, M. J. Mills, Dislocation structures and their relationship to strength in deformed nickel microcrystals. *Acta Mater.* **56**, 2988–3001 (2008).

76. H. J. Jin, J. Weissmüller, Bulk nanoporous metal for actuation. *Adv. Eng. Mater.* **12**, 714–723 (2010).

77. H. J. Jin *et al.*, Nanoporous au-pt alloys as large strain electrochemical actuators. *Nano Lett.* **10**, 187–194 (2010).

78. A. Wittstock, J. Biener, M. Bäumer, Nanoporous gold: a new material for catalytic and sensor applications. *Phys. Chem. Chem. Phys.* **12**, 12919–12930 (2010).

79. X.-L. Ye, H.-J. Jin, Electrochemical control of creep in nanoporous gold. *Appl. Phys. Lett.* **103**, 201912 (2013).

80. S.-M. Zhang, H.-J. Jin, Multilayer-structured gold/nanoporous gold composite for high performance linear actuation. *Appl. Phys. Lett.* **104**, 101905 (2014).

81. A. Mathur, J. Erlebacher, Size dependence of effective Young's modulus of nanoporous gold. *Appl. Phys. Lett.* **90**, 061910 (2007).

82. L. Rong, Sieradzki, Ductile-Brittle Transition in Random Porous Au. *Phys. Rev. Lett.* **68**, 1168–1171 (1992).

83. Y. Ding, M. Chen, J. Erlebacher, Metallic mesoporous nanocomposites for electrocatalysis. *J. Am. Chem. Soc.* **126**, 6876–6877 (2004).

84. J. Snyder, J. Erlebacher, in *ECS Transactions* (2011; http://ecst.ecsdl.org/cgi/doi/10.1149/1.3635634), vol. 41, pp. 1021–1030.

85. D. Wang, P. Zhao, Y. Li, General preparation for Pt-based alloy nanoporous nanoparticles as potential nanocatalysts. *Sci. Rep.* **1**, 1–5 (2011).

86. S. Chen *et al.*, Origin of oxygen reduction reaction activity on "Pt 3Co" nanoparticles: Atomically resolved chemical compositions and structures. *J. Phys. Chem. C.* **113**, 1109–1125 (2009).

87. S. Parida *et al.*, Volume Change during the Formation of Nanoporous Gold by Dealloying. *Phys. Rev. Lett.* **97**, 035504 (2006).

88. T. Fujita *et al.*, Unusually small electrical resistance of three-dimensional nanoporous gold in external magnetic fields. *Phys. Rev. Lett.* **101**, 1–4 (2008).

89. L. Tang *et al.*, Electrochemical stability of nanometer-scale Pt particles in acidic environments. *J. Am. Chem. Soc.* **132**, 596–600 (2010).

90. L. Tang, X. Li, R. C. Cammarata, C. Friesen, K. Sieradzki, Electrochemical Stability of Elemental Metal Nanoparticles. *J. Am. Chem. Soc.* **132**, 11722–11726 (2010).

91. N. Combe, P. Jensen, A. Pimpinelli, Changing Shapes in the Nanoworld. *Phys. Rev. Lett.* **85**, 110–113 (2000).

92. S. a. Policastro *et al.*, Surface Diffusion and Dissolution Kinetics in the Electrolyte–Metal Interface. *J. Electrochem. Soc.* **157**, C328 (2010).

93. Y. Ding, Y. J. Kim, J. Erlebacher, Nanoporous gold leaf: "Ancient technology "/advanced material. *Adv. Mater.* **16**, 1897–1900 (2004).

94. J. Snyder, K. Livi, J. Erlebacher, Dealloying Silver/Gold Alloys in Neutral Silver Nitrate Solution: Porosity Evolution, Surface Composition, and Surface Oxides. *J. Electrochem. Soc.* **155**, C464 (2008).

95. T. P. Moffat, F. F. Fan, A. J. Bard, Electrochemical and Scanning Tunneling Microscopic Study of Dealloying of Cu[sub 3]Au. *J. Electrochem. Soc.* **138**, 3224 (1991).

96. I. McCue *et al.*, Apparent Inverse Gibbs-Thomson Effect in Dealloyed Nanoporous Nanoparticles. *Phys. Rev. Lett.* **108**, 225503 (2012).

97. S. P. Lynch, Metal-induced embrittlement of materials. *Mater. Charact.* **28**, 279–289 (1992).

98. S. P. Lynch, Solid-metal-induced embrittlement of aluminium alloys and other materials. *Mater. Sci. Eng. A*. **108**, 203–212 (1989).

99. M. H. Kamdar, Embrittlement by liquid metals. *Prog. Mater. Sci.* **15**, 289–374 (1973).

100. M. G. G. Nicholas, C. F. F. Old, Liquid metal embrittlement. *J. Mater. Sci.* **14**, 1–18 (1979).

101. Q. Chen, K. Sieradzki, Spontaneous evolution of bicontinuous nanostructures in dealloyed Li-based systems. *Nat. Mater.* **12**, 1102–6 (2013).

102. P.-A. Geslin, I. McCue, B. Gaskey, J. Erlebacher, A. Karma, "Topology-generating Interfacial Pattern Formation During Liquid Metal Dealloying" (2015).

103. J. W. Kim, T. Wada, S. G. Kim, H. Kato, Sub-micron porous niobium solid electrolytic capacitor prepared by dealloying in a metallic melt. *Mater. Lett.* **116**, 223–226 (2014).

104. B. Šarler, Stefan's work on solid-liquid phase changes. *Eng. Anal. Bound. Elem.* **16**, 83–92 (1995).

105. J. C. Dibbern, thesis, Massachusetts Institute of Technology (2007).

106. D. B. Butrymowicz, J. R. Manning, M. E. Read, Diffusion in copper and copper alloys. Part III. Diffusion in systems involving elements of the groups IA, IIA, IIIB, IVB, VB, VIB, and VIIB. *J. Phys. Chem. Ref. Data*. **4** (1975), p. 177.

107. X.-L. Ye *et al.*, Primary and Secondary Dealloying of Au(Pt)-Ag: Structural and Compositional Evolutions, and Volume Shrinkage. *J. Electrochem. Soc.* **161**, C517–C526 (2014).

108. K. Sieradzki, The fracture strength of solids near the percolation threshold. *J. Phys. C Solid State Phys.* **18**, L855–L856 (1985).

109. K. Sieradzki, The Relationship Between Dealloying and Transgranular Stress-Corrosion Cracking of Cu-Zn and Cu-Al Alloys. *J. Electrochem. Soc.* **134**, 1635 (1987).

110. T. a. Schaedler *et al.*, Ultralight Metallic Microlattices. *Science (80-.).* **334**, 962–965 (2011).

111. L. R. Meza, S. Das, J. R. Greer, Strong, lightweight, and recoverable three-dimensional ceramic nanolattices. *Science (80-.).* **345**, 1322–1326 (2014).

112. D. Jang, L. R. Meza, F. Greer, J. R. Greer, Fabrication and deformation of three-dimensional hollow ceramic nanostructures. *Nat. Mater.* **12**, 893–898 (2013).

113. K. J. Hemker, W. D. Nix, Seeing is believing. *Nat. Mater.* **7**, 97 (2008).

114. J. R. Greer, J. T. M. De Hosson, Plasticity in small-sized metallic systems: Intrinsic versus extrinsic size effect. *Prog. Mater. Sci.* **56**, 654–724 (2011).

115. S.-W. Lee, W. D. Nix, Size dependence of the yield strength of fcc and bcc metallic micropillars with diameters of a few micrometers. *Philos. Mag.* **92**, 1238–1260 (2012).

116. J. R. Greer, W. C. Oliver, W. D. Nix, Size dependence of mechanical properties of gold at the micron scale in the absence of strain gradients. *Acta Mater.* **53**, 1821–1830 (2005).

117. Callister, *Materials Science Engineering: An Introduction* (Wiley).

118. M. Hakamada, M. Mabuchi, Mechanical strength of nanoporous gold fabricated by dealloying. *Scr. Mater.* **56**, 1003–1006 (2007).

119. C. a. Volkert, E. T. Lilleodden, Size effects in the deformation of sub-micron Au columns. *Philos. Mag.* **86**, 5567–5579 (2006).

120. Y. Sun, J. Ye, Z. Shan, A. M. Minor, T. J. Balk, The mechanical behavior of nanoporous gold thin films. *JOM*. **59**, 54–58 (2007).

121. H. Bei, S. Shim, G. M. Pharr, E. P. George, Effects of pre-strain on the compressive stress–strain response of Mo-alloy single-crystal micropillars. *Acta Mater.* **56**, 4762–4770 (2008).

122. H. BEI *et al.*, Compressive strengths of molybdenum alloy micro-pillars prepared using a new technique. *Scr. Mater.* **57**, 397–400 (2007).

123. R. Liu, A. Antoniou, A relationship between the geometrical structure of a nanoporous metal foam and its modulus. *Acta Mater.* **61**, 2390–2402 (2013).

124. M. M. Biener *et al.*, Ultra-strong and low-density nanotubular bulk materials with tunable feature sizes. *Adv. Mater.* **26**, 4808–4813 (2014).

125. N. a Senior, R. C. Newman, Synthesis of tough nanoporous metals by controlled electrolytic dealloying. *Nanotechnology*. **17**, 2311–2316 (2006).

126. S. L. Choi, thesis, University of Toronto (2009).

127. R. Gu, a. H. W. Ngan, Effects of pre-straining and coating on plastic deformation of aluminum micropillars. *Acta Mater.* **60**, 6102–6111 (2012).

128. K. S. Ng, a. H. W. Ngan, Effects of trapping dislocations within small crystals on their deformation behavior. *Acta Mater.* **57**, 4902–4910 (2009).

129. D. Gianola, K. J. Hemker, M. Legros, W. N. Sharpe, Experimental Techniques for Uncovering Deformation Mechanisms in Nanocrystalline Al Thin Films. *TMS Lett.* **1**, 7 (2004).

130. C. Eberl, R. Thompson, D. S. Gianola, W. N. Sharpe, K. J. Hemker, Digital Image Correlation (2006), (available at http://www.mathworks.com).

131. S. I. Rao *et al.*, Estimating the strength of single-ended dislocation sources in micron-sized single crystals. *Philos. Mag.* **87**, 4777–4794 (2007).

132. a. Misra, J. P. Hirth, R. G. Hoagland, Length-scale-dependent deformation mechanisms in incoherent metallic multilayered composites. *Acta Mater.* **53**, 4817–4824 (2005).

133. K. T. Ramesh, *Nanomaterials* (Springer US, Boston, MA, 2009; http://link.springer.com/10.1007/978-0-387-09783-1).

134. H. Conrad, K. Jung, Effect of grain size from mm to nm on the flow stress and plastic deformation kinetics of Au at low homologous temperatures. *Mater. Sci. Eng. A*. **406**, 78–85 (2005).

135. H. Conrad, Grain-size dependence of the flow stress of Cu from millimeters to nanometers. *Metall. Mater. Trans. A*. **35**, 2681–2695 (2004).

136. H. Conrad, S. Feuerstein, L. Rice, Effects of grain size on the dislocation density and flow stress of niobium. *Mater. Sci. Eng.* **2**, 157–168 (1967).

137. I. Ryu, W. Cai, W. D. Nix, H. Gao, Stochastic behaviors in plastic deformation of face-centered cubic micropillars governed by surface nucleation and truncated source operation. *Acta Mater.* **95**, 176–183 (2015).

138. W. D. Nix, Mechanical properties of thin films. *Metall. Trans. A*. **20**, 2217–2245 (1989).

139. N. A. Mara, D. Bhattacharyya, R. G. Hoagland, A. Misra, Tensile behavior of 40nm Cu/Nb nanoscale multilayers. *Scr. Mater.* **58**, 874–877 (2008).

140. J.-Y. Kim, D. Jang, J. R. Greer, Tensile and compressive behavior of tungsten, molybdenum, tantalum and niobium at the nanoscale. *Acta Mater.* **58**, 2355–2363 (2010).

141. E. G. Fu *et al.*, Mechanical properties of sputtered Cu/V and Al/Nb multilayer films. *Mater. Sci. Eng. A*. **493**, 283–287 (2008).

142. N. Li *et al.*, He ion irradiation damage in Fe/W nanolayer films. *J. Nucl. Mater.* **389**, 233–238 (2009).

143. N. Li, N. A. Mara, Y. Q. Wang, M. Nastasi, A. Misra, Compressive flow behavior of Cu thin films and Cu/Nb multilayers containing nanometer-scale helium bubbles. *Scr. Mater.* **64**, 974–977 (2011).

144. J. Snyder, P. Asanithi, A. B. Dalton, J. Erlebacher, Stabilized Nanoporous Metals by Dealloying Ternary Alloy Precursors. *Adv. Mater.* **20**, 4883–4886 (2008).

145. Z. Qi *et al.*, Porous Gold with a Nested-Network Architecture and Ultrafine Structure. *Adv. Funct. Mater.* **25**, 2530–2536 (2015).

146. a. a. Vega, R. C. Newman, Nanoporous Metals Fabricated through Electrochemical Dealloying of Ag-Au-Pt with Systematic Variation of Au:Pt Ratio. *J. Electrochem. Soc.* **161**, C1–C10 (2013).

Vita

Ian McCue was born in Philadelphia, Pennsylvania and grew up outside of the city in Yardley Borough. He graduated from Johns Hopkins University with a degree in Materials Science and Engineering (2010), where his senior research design project was the fabrication of single crystal aluminum oxide substrates for organic transistor devices. He joined Professor Jonah Erlebacher's research group at Johns Hopkins University in 2010 to pursue a Ph.D. in Materials Science and Engineering studying the limits and tuenability of dealloying.

Publications

Manuscripts in Preparation (available upon request)

10. **I. McCue**, J. Erlebacher, "The Underlying Strength of Individual Phases in Metal/Metal Bicontinuous Composites," *expected submission October 2015.*

9. **I. McCue**, B. Gaskey, PA. Geslin, A. Karma, J. Erlebacher, "Kinetics of Liquid Metal Dealloying: An Experimental Study," expected submission *September 2015.*

Refereed Journal Publications

8. **I. McCue**, E. Benn, B. Gaskey, J. Erlebacher, "Dealloying and Dealloyed Materials," *Annual Reviews of Materials Research*, In Production.

7. PA. Geslin, **I. McCue**, B. Gaskey, A. Karma, J. Erlebacher, "Topology-generating interfacial pattern formation during liquid metal dealloying," Accepted (2015).

6. **I. McCue**, S. Ryan, K. Hemker, X. Xu, N. Li, M. Chen, J. Erlebacher, "Size Effects in the Mechanical Properties of Bulk Bicontinuous Ta/Cu Nanocomposites Made by Liquid Metal Dealloying," *Advanced Engineering Materials*, Accepted (2015). DOI: 10.1002/adem.201500219.

5. X. Li, Q. Chen, **I. McCue**, J. Snyder, P. Crozier, J. Erlebacher, K. Sieradzki, "Dealloying of Noble-Metal Alloy Nanoparticles," *Nano Letters,* **14 (5)**, 2569-2577 (2014).

4. J. Erlebacher, **I. McCue**, "Geometric Characterization of Nanoporous Metals," Acta Materialia, **60 (17)**, 6164–6174 (2012).

3. **I. McCue**, J Snyder, X Li, Q Chen, K Sieradzki, J Erlebacher, "Apparent Inverse Gibbs Thomson Effect in Dealloyed Nanoporous Nanoparticles," *Physical Review Letters*, **108 (22)**, 225503 (2012).

2. J. Snyder, **I. McCue**, K. Livi, J. Erlebacher, "Structure/Processing/Properties Relationships in Nanoporous Nanoparticles As Applied to Catalysis of the Cathodic Oxygen Reduction Reaction," *Journal of the American Chemical* Society, **134 (20)**, 8633–8645 (2012).

1. J. Sun, O. Wilson, M. Reese, B.J. Jung, T. Dawidcyk, M. Yeh, B.M. Dhar, B.N. Pal, P. Trottman, **I. McCue**, L. Berger, G.R. Blum, E. Heinemann, D. McGee, J.D. Erlebacher, H.E. Katz, "Hands-on Preparation and Testing of Solution-Processed Semiconductor Devices in the Undergraduate Classroom," *Journal of Materials Education*, **31 (5)**, 271-284 (2009).

Presentations

"*" denotes an invited presentation. Presenting authors are underlined.

Oral Presentations

9. **I. McCue**, B. Gaskey, P.-A. Geslin, A. Karma, J. Erlebacher, "Kinetics of Morphological Evolution during Liquid Metal Dealloying" *Materials Research Society Fall Meeting*, Boston, Massachusetts, to be presented December 2nd 2015 [**Accepted**].

8. **I. McCue**, S. Ryan, K. Hemker, J. Erlebacher, "Bulk Bicontinuous Ta/Cu Nanocomposites Made by Liquid Metal Dealloying : Structure and Mechanical Properties," *Materials Research Society Fall Meeting*, Boston, Massachusetts, to be presented December 1st, 2015 [**Accepted**].

7. **I. McCue,** S. Ryan, K. Hemker, X. Xu, N. Li, M. Chen, J. Erlebacher, "Hierarchical, Bicontinuous Refractory-Based Nanocomposites," *Materials Research Society Fall Meeting*, **Graduate Student Award Talk**, Boston, Massachusetts, December 2nd 2014 [**Talk**].

6. **I. McCue,** S. Ryan, K. Hemker, X. Xu, N. Li, M. Chen, J. Erlebacher, "Hierarchical, Bicontinuous Refractory-Based Nanocomposites," *Materials Research Society Fall Meeting*, Boston, Massachusetts, December 1st 2014 [**Talk**].

5. **I. McCue,** S. Ryan, K. Hemker, X. Xu, N. Li, M. Chen, J. Erlebacher, "Mechanical Properties of Hierarchical Refractory-Based Nanocomposites," *First International Symposium on Nanoporous Materials by Alloy Corrosion*, Lake Bostol, Germany, September 30th 2014 [**Talk**].

4. *J. Erlebacher, E. Benn, I. McCue, "Control of the Interface Mobility during Dealloying: New Systems and New Materials," *Materials Research Society Fall Meeting*, Boston, Massachusetts, December 5th 2013 [**Talk**].

3. *I. McCue, J. Erlebacher, "Dealloying and Fabrication of Porous Tantalum," *Gordon Research Conference in Thin Film and Crystal Growth*, Biddeford, Maine, July 9th 2013 [**Talk**]. *Abstract was selected to give oral presentation.*

2. I. McCue, J. Snyder, X. Li, Q. Chen, K. Sieradzki, and J. Erlebacher, "Apparent Inverse Gibbs-Thomson Effect in Dealloyed Nanoporous Nanoparticles," *Materials Research Society Fall Meeting*, Boston, Massachusetts, November 29th 2012 [**Talk**].

1. X. Li, I. McCue, J. Snyder, J. Erlebacher, K. Sieradzki, "Dealloying of Nanoparticles," *Fall ECS Meeting*, Honolulu, HI, October 11 2012 [**Talk**].

Poster Presentations

2. I. McCue, PA. Geslin, S. Ryan, K. Hemker, A. Karma, J. Erlebacher, "Bicontinuous Refractory-Based Nanocomposites," *Gordon Research Conference in Physical Metallurgy*, Biddeford, Maine, July 19th-24th 2015.

1. I. McCue, J. Erlebacher, "Liquid Metal Dealloying of Binary Refractory Alloys," *Materials Research Society Fall Meeting*, Boston, Massachusetts, December 2nd 2013.

Patent

1. J. Erlebacher, **I. McCue**, "Nanostructured Composite Materials Containing Refractory Elements," U.S. Patent Application Serial No. 13/975,659 filed on **August 26, 2013**